Matteo Briganti

Modeling of Transition Metals and Lanthanides Containing Materials by *Ab Initio* Methods

Ciclo XXX

UNIVERSITÀ DEGLI STUDI FIRENZE

DOTTORATO DI RICERCA IN
SCIENZE CHIMICHE

CICLO XXX

COORDINATORE Prof. PIERO BAGLIONI

Modeling of Transition Metals and Lanthanides Containing Materials by *Ab Initio* Methods

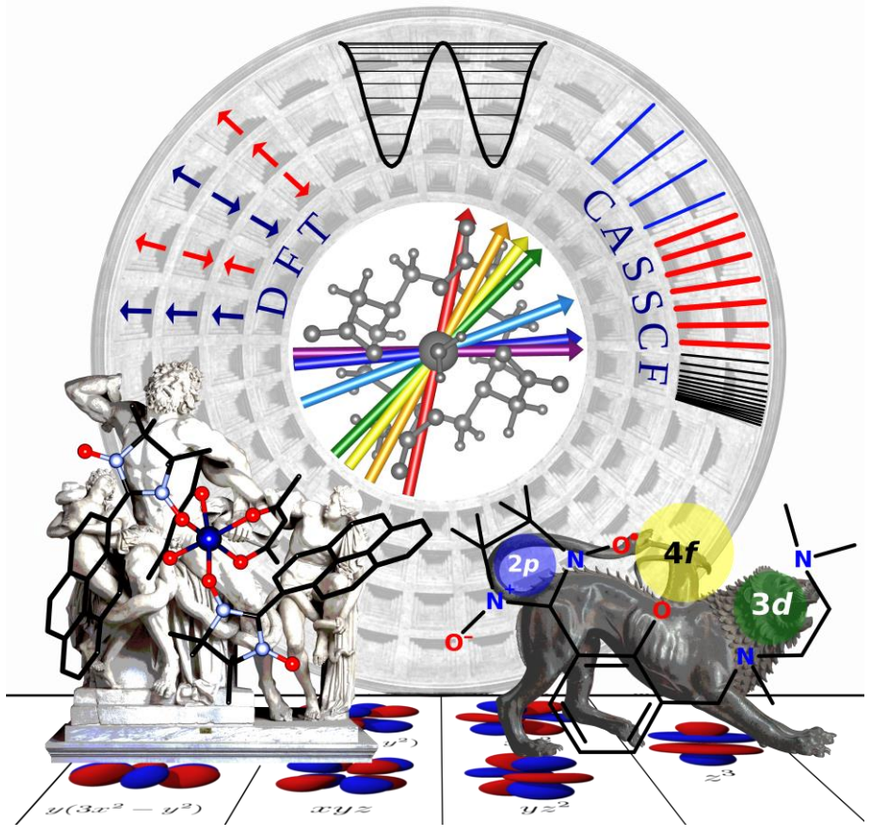

Dottorando
Dott. Matteo Briganti

Tutori
Prof. Federico Totti
Prof.ssa Maria das Graças Fialho Vaz

UNIVERSITÀ
DEGLI STUDI
FIRENZE

DOTTORATO DI RICERCA IN SCIENZE CHIMICHE

CICLO XXX

COORDINATORE Prof. PIERO BAGLIONI

Modeling of Transition Metals and Lanthanides

Containing Materials by *Ab Initio* Methods

Settore Scientifico Disciplinare CHIM/03

Dottorando
Dott. Matteo Briganti

(firma)

Tutori

Prof. Federico Totti

(firma)

Prof.ssa Maria das Graças Fialho Vaz

(firma)

Coordinatore
Prof. Piero Baglioni

(firma)

Anni 2014/2017

Anche un quadrato,
in prima approssimazione,
è un cerchio.

A Bernardo

Contents

Preamble and Acknowledgments

The present document is the result of three years of Ph.D. in joint-agreement between the University of Florence (Italy) and the Fluminense Federal University in Niteroi (Brazil) under the supervision of Prof. Federico Totti[a] and Prof. Maria das Graças Fialho Vaz[b].

I thank the European Research Council (ERC), through the advanced grant MolNanoMaS (no. 267746), and the Fundaçao de Amparo e Pesquisa do Estado do Rio de Janeiro (FAPERJ), through the 'Bolsa de Doutorado Sanduiche Reverso' (process no. E-26/200.104/2016), for funding my PhD scolarship. I acknowledge the financial support from 'Coordenaçao de Aperfeiçoamento de Pessoal de Nivel Superior' (CAPES, project 88881. 030358/2013-01) and from the 'Conselho Nacional de Desenvolvimento Científico e Tecnológico' (CNPq). A very special thanks to the 'Laboratorio Naçional de Computaçao Cientifica' in Petropolis (LNCC) and to the 'Centro Nacional de Processamento de Alto Desempenho' in Sao Paulo (CENAPAD-SP), for the availability of high performance computing resources and support (project MagMolTVB and project No.627, respectively).

The work that I developed in the course of the three years regards exclusively the theoretical and computational aspects of the subjects presented in this Ph.D. thesis, but a central focus was the collaboration with the experimental counterparts. Therefore, for reason of clarity, in the course of this manuscript experimental evidences, calculations and theorical analysis will be presented in a seamless way, without further specifications. Since I had the occasion to work with several colleagues from various Institutes, the list of the collaborators, along with their affiliation for each subject is presented hereby:

- **Mononuclear Lanthanide Complexes**: Eva Lucaccini[a], Mauro Perfetti[c], Lorenzo Sorace[a], Roberta Sessoli[a], Laure vendier[d], Jean-Pierre Costes[d], Julie Jung[e], Guglielmo Fernandez Garçia[e,a], Boris Le Guennic[e], Laura Chelazzi[a].

[a]Università degli Studi di Firenze, Dipartimento di Chimica 'Ugo Schiff', Via della Lastruccia 3-13, Sesto Fiorentino 50019 (Italy)

[b]Universidade Federal Fluminense, Instituto de Química, Outeiro de Sao Joao Batista s/n, Campus do Valonguinho, Centro - Niterói (RJ), CEP 24020-150 - Brasil

[c]University of Copenhagen, Department of Chemistry, Universitetsparken 5, DK 2100 Copenhagen, Denmark

[d]Laboratoire de Chimie de Coordination CNRS 205 Route de Narbonne, Toulouse F-31077 (France)

[e]Institut des Sciences Chimiques de Rennes, UMR 6226 CNRS Université de Rennes 1, 263 Avenue du Général Leclerc 35042 Rennes Cedex (France)

- **Heterospin Systems**: Samira G. Reis[b], Sergiu Calancea[f], Andrei Patrascu[g], Stephane Soriano[h], Rafael A. A. Cassaro[i], Guilherme P. Guedes[b], Miguel A. Novak[j], Carmen Tiseanu[k], Marius Andruh[g], Miguel A. del Aguila-Sanchez[l], Fernando Lopez-Ortiz[l], Andrea Caneschi[a].

- **Single Chain Magnets**: Rafael C. A. Allao[i], Benjamin R. Salles[j], Miguel A. Novak[j].

I would like to thank all my two 'scientific families', i.e. all the staff of the two research groups that gave me the possibility to carry on my research activity: the 'Laboratorio di Magnetismo Molecolare' (LAMM) in Florence and the 'Laboratorio de Magnetismo Molecular' (MagMol) in Niteroi.

I particularly would like to acknowledge Professors Roberta Sessoli, Lorenzo Sorace, Andrea Caneschi, Stephane Soriano, Rafael A. A. Cassaro, Guilherme P. Guedes, Miguel A. Novak and Marius Andruh, for their fruitful discussions and their constant support that inspired my work.

A special appreciation is due to Doctors Eva Lucaccini, Mauro Perfetti, Samira G. Reis, Sergiu Calancea and Andrei Patrascu for providing me the experimental data to support my calculations.

A very thankful acknowledgment is deserved to Guglielmo Fernandez Garçia, Alessandro Lunghi, Sara Giachetti and Giacomo Londi, for sharing with me joy and sorrow along these three years.

Finally, the last but most appreciated thank is due to Federico Totti and Maria G. F. Vaz, who have been much more than two tutors.

[f]Universitatea de Stat din Moldova str. Alexe Mateevici, 60 Chisinau, MD-2009 Republic of Moldova

[g]Inorganic Chemistry Laboratory, Faculty of Chemistry, University of Bucharest, Str. Dumbrava Rosie nr. 23, 020464-Bucharest, Romania

[h]Universidade Federal Fluminense, Instituto de Fisica, Rua Passo da Pátria, 156, Campus da Praia Vermelha, Sao Domingos, Niteroi, RJ 24210-310, Brazil

[i]Instituto de Química, Universidade Federal do Rio de Janeiro, Av. Athos da Silveira Ramos, 149-Cidade Universitaria, Rio de Janeiro, RJ 21941-909, Brazil

[j]Instituto de Física, Universidade Federal do Rio de Janeiro, Av. Athos da Silveira Ramos, 149-Cidade Universitaria, Rio de Janeiro, RJ 21941-909, Brazil

[k]National Institute for Laser, Plasma and Radiation, Str. Atomistilor 409, 077125-Magurele, Romania

[l]Area de Quimica Organica, Universidad de Almeria, Crta. Sacramento s/n, 04120, Almeria, Spain

Scientific Production

List of Papers

Published

- Eva Lucaccini, Matteo Briganti, Mauro Perfetti, Laure Vendier, Jean-Pierre Costes, Federico Totti, Roberta Sessoli and Lorenzo Sorace. **Relaxation Dynamics and Magnetic Anisotropy in a Low-Symmetry Dy Complex.** ***Chemistry. A European Journal.*** **2016**, *22*, 5552-5562

- Samira. G. Reis, Matteo Briganti, Stéphane Soriano, Guilherme. P. Guedes, Sergiu Calancea, Carmen Tiseanu, Miguel A. Novak, Miguel A. del Águila-Sánchez, Federico Totti, Fernando López-Ortiz, Marius Andruh, and Maria G.F. Vaz. **Binuclear lanthanide-radical complexes featuring two centers with different magnetic and luminescence properties.** ***Inorganic Chemistry.*** **2016**, *55*, 11676-11684.

- Andrei A. Patrascu, Sergiu Calancea, Matteo Briganti, Stéphane Soriano, Augustin M. Madalan, Rafael A. Allão Cassaro, Andrea Caneschi, Federico Totti, Maria G. F. Vaz and Marius Andruh, **A chimeric design of heterospin 2p-3d, 2p-4f, and 2p-3d-4f complexes using a novel family of paramagnetic dissymmetric compartmental ligands.** ***Chemical Communications***, **2017**, *53*, 6504-6507.

In Preparation

- Matteo Briganti, Guglielmo Fernandez-Garçia, Julie Jung, Boris Le Guennic, Roberta Sessoli, Federico Totti. **Subtle Geometrical Effects on a Mononuclear Lanthanide Single Molecule Magnet: the DyDOTA Archetype.**

- Matteo Briganti, Eva Lucaccini, Laura Chelazzi, Lorenzo Sorace, Roberta Sessoli, Federico Totti, and Mauro Perfetti, **Systematic determination of magnetic anisotropy in LnDOTA series combining experimental and theoretical results.**

- Matteo Briganti, Rafael A. Allão Cassaro, Benjamin R. Salles, Federico Totti, Miguel Novak and Maria G. F. Vaz, **Reversible Photomagnetism of a Cobalt Pyrenylnitronylnitroxide Single**

Chain Magnet with Record Blocking Temperature: an Experimental and Theoretical Characterization.

List of Papers not included into the thesis

- Samira G. Reis, Matteo Briganti, Daniel O. T. A. Martins, Handan Akpinar, Sergiu Calancea, Guilherme P. Guedes, Stéphane Soriano, Marius Andruh, Rafael A. A. Cassaro, Paul M. Lahti, Federico Totti and Maria G. F. Vaz. **First coordination compounds based on a bis(iminoylnitroxide) biradical and 4*f* metal ions: synthesis, crystal structures and magnetic properties.** ***Dalton Transactions.*** **2016**, *45*, 2936-2944.

Abstract

During this Phd thesis the analysis at the *post*-Hartree Fock level was focalized on transition metal ion and lanthanide containing systems characterized by a pronounced magnetic anisotropy. The work was progressively focused on molecular systems with higher level of complexity: mononuclear complexes, $2p$-$4f$ polinuclear systems, $2p$-$4f$-$3d$ heterospin complexes and, finally, $2p$-$4d$ one dimensional magnetic systems. The computational protocol employed is the Complete Active Space Self-Consistent Field (CASSCF), followed by Complete Active Space State Interaction (CASSI) for the calculation of the Spin-Orbit interaction. CASSCF is a *post*-HF multiconfigurational computational protocol. This method is necessary in order to take into account the electronic correlation in the calculation of the excited states of the system: the electronic states indeed have to be computed at an high level of theory in order to map the magnetic anisotropy.

The first part of this thesis was dedicated to the computational investigation of lanthanide based single ion magnets (SIMs). *Ab initio* calculations of the ground and excited states of the $Dy(LH)_3$ complex showed to reproduce experimental magnetic data (susceptometry, magnetization and cantilever torque magnetometry). Moreover, the most probable relaxation path between the two opposite sides of the anisotropy barrier was evaluated allowing the interpretation of the AC data. The analysis of the DyDOTA complex confirmed the influence of the water molecule directly bonded to the lanthanide atom on the orientation of the magnetic anisotropy axis. Calculations were also performed where the water molecule was substitued by its multipolar expansion. These results undermined the common idea that the magnetic properties are only determined by the purely electrostatic interaction between the $4f$-orbitals and the electric multipolar moments of the ligands. The protocol employed was then applied on the isostructural series of Ln(DOTA) (Ln = Ce, Pr, Nd, Eu, Gd, Er).

Regarding heterospin sytems, the exchange couplings between radicals, the lanthanide ions and transition metals were computed by CASSCF methods. The magnetic anisotropy of the isostructural series of binuclear complexes, Ln_2dppnTEMPO, containing two lanthanide ions bridged by an organic radical, was computed. The electronic structure, g-tensor and crystal field parameters were simulated. Two heterotrispin systems based on coupling a lanthanide ion with an organic radical and/or a transition metal ion were compared and a qualitative analysis of the relaxation path of the magnetization was attempted, giving an insight on the different

observed magnetic behaviour.

Calculations on cobalt containing Single Chain Magnets were performed. The study was focused on the reproduction of the structural, magnetic and electronic data of this system in the bulk phase. A reliable computational protocol is, indeed, necessary in order to unambiguously characterize a molecular system on surface, where the common techniques of structural investigation are not employable. The single repetitive unit of the coordination polymer was studied by *post*-Hartree Fock methods, then optimization of the geometry, with and without the co-crystallized solvent, and mapping of the magnetic exchange constants at periodic DFT level was performed. The optimized geometry showed only minimal modifications from with the X-Ray structure. However, in order to reproduce magnetic properties, i.e. the exchange coupling constants, the addition of a localizing potential, the Hubbard's U parameter, to the revPBE functional was crucial.

List of Abbreviations

- **SMM**: Single Molecule Magnet
- **SIM**: Single Ion Magnet
- **SCM**: Single Chain Magnet
- **MN**: Molecular Nanomagnet
- **SO**: Spin-Orbit
- **QTM**: Quantum Tunneling of Magnetization
- **CASSCF**: Complete Active Space Self Consistent Field
- **CASSI**: Complete Active Space Configuration Interaction
- **DFT**: Density Functional Theory
- **pDFT**: Periodic Density Functional Theory
- **BS**: Broken Symmetry

Chapter 1

Introduction

Single Molecule Magnets (SMMs) are a class of compounds that present under a certain temperature, called the blocking temperature T_{block}, slow relaxation of the magnetization and eventually the opening of an hysteresis loop, acting as a magnet of molecular dimension.[1] These properties arise from the electronic structure of the isolated molecule and not from trough space long range interactions like in classical magnets. In these systems the spin structure takes the form of the so-called 'double well potential' (see figure 1.1), where states with opposite quantum number M_S lie at the same energy but at opposite side of a potential barrier U, the anisotropy barrier. U in first approximation is equal to $|DS^2|$, where D is the zero field splitting constant and it is proportional to the spin-orbit (SO) coupling. Applying a magnetic field, it is possible to remove the degeneracy and magnetize the system transferring population from one side to the other of the barrier. Removing the field under T_{block} the magnetization persists because the spin has to overcome U to restore the thermodinamic equilibrium. The rate of this process, named slow relaxation of magnetization, is modeled with an Arrhenius-like behaviour

$$\tau = \tau_0 e^{\frac{U}{k_B T}} \qquad U = DS^2 \tag{1.1}$$

where τ is the mean time necessary for the spin overcome the barrier U.

Cluster of transition metal ions were the first complexes which showed this behaviour.[2] The first time it was observed on a crystal of the polynuclear complex $[Mn_{12}O_{12}(CH_3COO)_{16}(H_2O)_4]$, Mn_{12}ac, published in 1993, with an anisotropy barrier of 61 K and a blocking temperature of 2.5 K. Since then the number of SMMs synthesized and observed has constantly

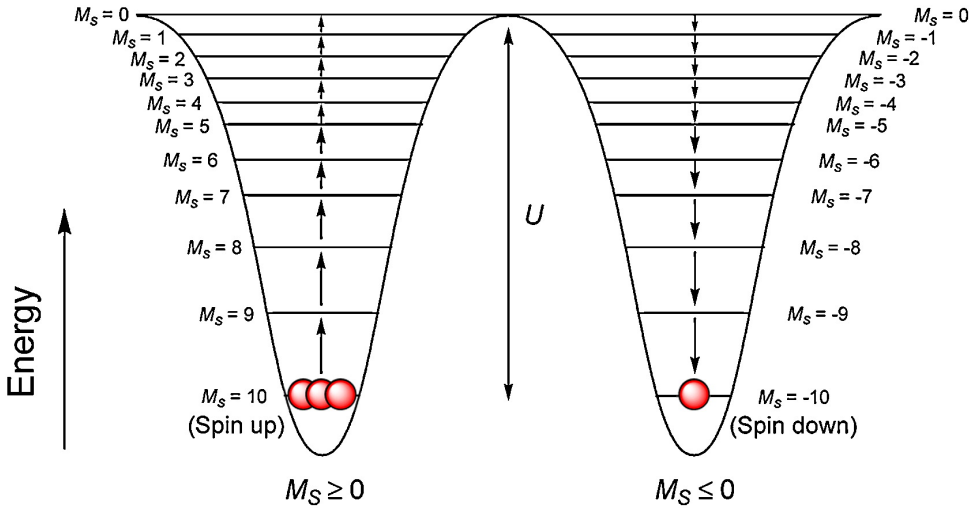

Figure 1.1: Double-well energy potential for the Mn_{12} molecule. The picture is taken from Feltham and Brooker.[6]

grown. Their mesoscopic dimensions allow to observe a cohexistence of classic and quantomechanic effects such quantum tunneling of magnetization[3–5] (QTM, *vide infra*). Moreover their molecular nature makes SMMs a perfect monodispersion of nanoparticles and consequently a model system to investigate effects at the border between nanoscopic and macroscopic world. In 2008 the discovery of SMM and QTM effects was declared a milestone in the history of spin by the journal *Nature*.

For all these reasons, their possible implementation on a new generation of devices has been deeply investigated. In principle each molecule can act as an independent operative unit where classical and quantistic phenomenon cohexist and potential application of these systems have been proposed, due to the possibility to reduce the dimension of the single components of a device at the mesoscopic level.

- **Information Storage**. The manipulation of the state of the atoms by scanning tunneling miscroscopy allows the storage of information at the atomic/molecular level. The proof of concept of this idea is a rewritable memory with a potential information density of 502 terabits per square inch recently reported by Kalff *et al.*,[7] who proved to control the position of the vacancies on a two dimensional lattice of clorine atoms adsorbed on a Cu(100) surface. Switching from atoms to molecules, SMMs can be seen as magnetic memories of molecular dimensions,[8] because the two states with opposite magnetization are

molecular analogues of the two states of a classical bit. Indeed the possibility to employ molecular nanomagnets was shown by Mannini *et al.*[8,9] that observed magnetic hysteresis and quantum tunneling of magnetization of molecular origin of a Fe_4 monolayer adsorbed on Au(111) surface. The adsorption of ordered layers of SMMs, the control on their relative orientation and the mantainment of their molecular magnetic properties on surface paved the way to a new generation of devices.

- **Quantum Computation** The nanometric dimensions of a molecule allows to observe and exploit quantum mechanical effects non observables in macrosocopic systems. It is possible to create linear superimposition of states with long decoherence times by means of electromagnetic radiation and employ them as quantum bits to perform logical operations.[10,11] The rich electronic structure available enable the presence of more than one qubit and the implementation of a quantum logical gate inside a single molecule.[12] Magnetic quantum processors based on single molecule qubit are currently under investigation: their feasibility and scalability has been recently demonstrated by means of simulations[13]

- **Molecular Spintronic** The giant magneto resistance effect demonstrated that the electric properties of a material could be manipulated by means of magnetic field by exploiting one of the intrinsic property of matter: the spin. After discovering that the injection, manipulation and detection of spin currents by means of molecules proved to be feasible, electronic devices based on molecular spintronic[14] have been investigated. The results showed that molecular materials can show better performances than the classical semiconductor and inorganic materials. Molecular nanomagnets are promising tools in this area hence they offer different possibilities to polarize the spin currents:[15] in principle both the exchange coupling (in transition metal based SMM) and the magneto-crystalline anisotropy (in lanthanide containing SIMs) could be exploited. Molecular spin transistors[16] and spin-valves[17] based on the first SIM, the $Tb(pc)_2$ have been reported.

These striking advances towards end-user applications gave impetus to the research efforts and nowadays researcher in this ares have to focus on two main challenges.

The increase of the blocking temperature is the first one. In order to be economically feasible, idealy molecular nanomagnets should present

their properties at room temperature. A magnetic hysteresis at least observed at nitrogen's boiling temperature would be a major breakthrough, because it would not require refrigeration by means of liquid helium. This goal implies an extensive research towards two directions: i) the suppression of the quantum tunneling of magnetization which allows a magnetic relaxation path in zero magnetic field at low temperatures; ii) the engineering of the spin-phonon coupling, which is responsible of the very small experimental preexponential factors of the arrhenius law τ_0 (*vide infra*), vanishing the strong increases of the anisotropy barrier U.

The second challenge is the safe adsorption and organization on surface. In a real device the single molecule should retain their properties on surface, be ordered and accessible in order to allow the manipulation of their spin-state to write and read informations, perform logical operations, inject and detect spin currents. Many of these polynuclear clusters are very fragile from a redox point of view and undergo some structural transformations upon adsorption on surface. Indeed, the disappearence of SMM behaviour upon the interaction with surface has been already observed and the surface has been demonstrated not to be an inert support but interacts with the adsorbed molecules changing their properties. The SMM therefore should be designed in order to have a robust electronic structure and preserve their magnetic properties. At the same time the surface should be chosen in order to eventually interact with the SMM and improving its behaviour.

As it will be explained in the following chapters, the *ab initio* compass can help to orient the researcher's serendipity in the mesosocopic jungle of molecular nanomagnets. Indeed several synthetic strategies can be pursued, the informations extracted from different experiments can hide unexpected behaviours. A forefront computational protocol is required: capable not only to rationalize the experimental data coming from a really wide variety of techniques but also to predict new properties and direct future research.

This thesis will be structured in four chapters. After this introduction, in the second and third chapter the main issues will be presented: the questions to solve when molecular nanomagnets of the presented class of systems are treated from a computational point of view, along with a brief description of the theoretical methods proposed. In the fourth chapter the study of a series of mononuclear lanthanide compounds will be discussed and analyzed in detail: the $Dy(LH)_3$ molecule will show how experimental data can be rationalized by *ab initio* calculations and *viceversa*; the archetipal compound Dy(DOTA) will be deeply investigated by a

large amount of magneto-structural correlations and a review of the models present in literature will be presented: the results will shed light on the nature of the chemical bonding in the $4f$ elements and on the fundamental importance of a reliable modeling of the environment around the lathanide ion; the whole series of the Ln(DOTA) series will be finally presented in order to validate and extend our proposed computational protocol. In the fifth chapter the calcultions performed on two classes of heteropin systems will be presented: an isostructural series of $2p$-$4f$ binuclear compounds, Ln_2(dppnTEMPO), will show how a how interaction between differents magnetic centers can be accessed; then two compounds, a $2p$-$4f$ system and a $2p$-$3d$-$4f$ one made with the same paramagnetic compartimental ligand will be investigated and compared in order to rationalize dynamic properties and extrapolate general tools to obtain better performances in heterospin SMMs. In the last chapter a multilevel modeling of the SCM with the actual record blocking temperature will be presented: the CoPyrNN single chain magnet. The whole protocol will range from *post*-Hartree Fock to periodic DFT methods. The computational method was tuned on the reproduction of the bulk properties of the system in order to study in a second phase the adsorption process on surface, where the experimental and magnetic data are ambiguous and difficult to rationalize in a complete picture.

1.1 Transition Metal Clusters

Large efforts were devoted to increase U, the relaxation time and the blocking temperature in order to employ these systems in real devices. The Mn_{12} system, the so-called 'Drosophila' of the SMMs, has been extensively studied from both experimental and theoretical[18] point of views and their properties come from a combination of pronounced easy axis anisotropy, and high point symmetry which prevents the system from tunneling (*vide infra*). However, for ten years the anisotropy barriers have not reached than few tens of K due to the small magnitude of the SO coupling in the *d*-block elements. In order to reach high anisotropy barriers, huge synthetic efforts were spent in order to obtain SMMs characterized by an high spin multiplicity of the ground state: the actual record is the Mn_{17} cluster,[19] which is an SMM charcterized by an impressive S = 37. At the same time the SMM with the highest nuclearity is the Mn_{84} molecular wheel[20] which presents a ground state having 'only' a spin multiplicity S = 6. However, no strong increase in the magnitude of the anisotropy barrier was reported: the already mentioned Mn_{17} has a U_{eff} = 9 cm^{-1}

(13K), a D = -0.66 K,[21] an hysteresis loop visible below 13 K.

This absence of improvements arises due to the nature of the zero-field splitting in transition metal based clusters: the spin-orbit coupling. The d orbitals strongly partecipate to the bonding with the ligands and therefore their obital angular momentum is in first approximation quenched. The total spin S is a good quantum number and the spin orbit coupling can be treated in a perturbative approach. Inside this framework, for a mononuclear complex the spin-orbit hamiltonian can be expressed in the following form

$$\mathcal{H}_{SO} = \lambda \mathbf{L} \cdot \mathbf{S} \qquad \lambda = \pm\zeta/2S \tag{1.2}$$

where $\mathbf{S}$ and $\mathbf{L}$ are total spin and orbital angular momentum operator for a given ^{2S+1}L Russell-Saunders' term and ζ is the spin-orbit coupling constant. Indeed the zero field splitting can be expressed within the second order perturbation theory as

$$\mathbf{D} = -\lambda^2 \mathbf{\Lambda} \tag{1.3}$$

$$\mathbf{\Lambda} = \sum_n \frac{\langle g|\mathbf{L}|n\rangle \langle n|\mathbf{L}|g\rangle}{E_n - E_g} \tag{1.4}$$

where $\langle g|$ and $|n\rangle$ are the ground and excited states, and the sum goes on all the excited states with $\Delta S = 0, \pm 1$ with respect to the ground one, as pointed out by Neese[22] and Pederson.[18] This expression shows that the zero field splitting is directly proportional to the mixing of the ground with the lowest in energy excited states with an unquenched angular momentum.

This treatment allows to rationalize the values of the anisotropy barriers in polynuclear complexes: if exchange coupling between centers is stronger than the other terms of the spin hamiltonian, i.e. strong exchange coupling regime, the zero field splitting term can be treated as a perturbation of the exchange coupled states. Under these assumptions it can be demonstrated that the $\mathbf{D_S}$ tensor of the whole molecule is a linear combination of the $\mathbf{D_i}$ tensor of the single ions and the following relation[23] is valid:

$$\mathbf{D}_S = \sum_i d_i \mathbf{D}_i + \sum_{i<j} d_{ij} \mathbf{D}_{ij} \tag{1.5}$$

where $\mathbf{D}_i$ and $\mathbf{D}_{ij}$ are the single ion and exchange anisotropy tensors, respectively. The coefficients take the form

$$d_i = \frac{2S_i - 1}{N(2NS_i - 1)} \qquad d_{ij} = \frac{2S_i}{N(2NS_i - 1)} \tag{1.6}$$

Therefore, for a given molecule, the increasing of the ground state spin multiplicity cause a decrease of the anisotropy of the whole molecule. Augmenting the number of spin centers N ferromagnetically coupled, and consequently the spin multiplicity of the ground state, the combination coefficients decrease as $\frac{1}{S^2}$. In consequence, the anisotropy barrier, which depends both from S and D, will not show a significative improvement as it could be expected. Moreover, the highest theoretical anisotropy barrier will grow at most linearly with the number of magnetically coupled centers N, and not with N^3 as it was previously conjectured. The trend is valid in general,[24] and the relation was demonstrated for an arbitrary number N of coupled spins without other assumptions.

However, if you take into account also the orientation of the anisotropy tensors $\mathbf{D}_i$, it can be demonstrated that the highest possible values of D and U is obtained for a parallel orientations of the single ion's easy axes. An high number N of spin centers magnetically coupled makes very difficult to attain this condition by means of synthetic strategies. Such an issue prevents to observe even the linear increase of U as a function of N, e.g. in the Mn_{84} molecular wheel.[20] As a matter of fact, the Mn_{12} cluster held the records of the highest anisotropy barrier and blocking temperature among SMMs until 2003, when a competely new strategy was proposed. Indeed, in order to design high performing SMM, working on the local anisotropy tensors $\mathbf{D}_i$ of the single magnetic center, i.e. of the single metal ion, seems more promising.[24]

1.2 Lanthanide Based Single Ion Magnet

The pioneering work of Ishikawa[25] demonstrated that in mononuclear complexes containing lanthanide ions, anisotropy barriers of hundreds of K could be reached, a order of magnitude higher than the ones observed until then. These compounds were called Single Ion Magnets (SIMs) and acquired a central role in the field of molecular magnetism.

The most important property of Lanthanides is the decreasing in radius of the trivalent lanthanide ions on crossing the series from La to Lu. This is called 'Lanthanide Contraction' and it is caused by the poor screening of the nuclear charge by the $4f$ electrons. For this reason they are much less diffuse than $5s$ and $5p$ orbitals and much more 'core like' (see figure 3.1). Further, the $4f$ orbitals are shielded by the electrons in the $5s$ and $5p$ shells from interacting with the ligands,[26] so they have little participation in chemical bond formation.

As a consequence their orbital angular momentum is largely unquenched

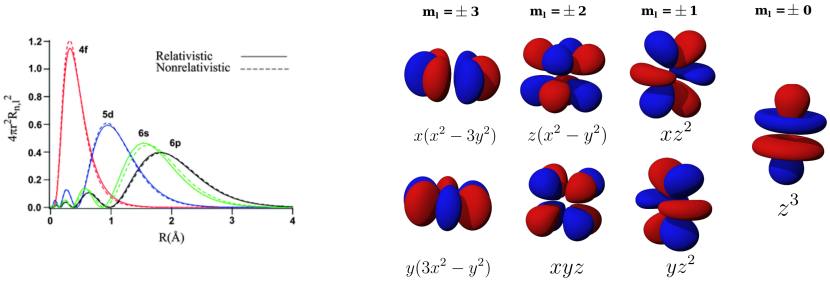

Figure 1.2: (Left)Radial part of the atomic $4f$ orbitals. (Right) Shape of general set of the $4f$ orbitals

causing the rise of a magnetic anisotropy of first order. Their spin-orbit coupling is stronger in energy than the crystal field, which is considered as a perturbation of the free-ion levels able to break the spherical symmetry and splitting the $2J + 1$ levels of the ground multiplet. The perturbative approach is confirmed by the energies of the interactions,[26,28] as it can be seen in table 1.1.

Lanthanide-based SIMs couple the high barriers U with molecular structures made of few tens of atoms, molecules not characterized by the elaborate architectures as the cluster of $3d$ transition metals. Therefore their structural simplicity allows a fine tuning of the bonding parameters in order to improve the properties of these compounds. However despite record energy barriers of thousands of K, the blocking temperatures remained around the temperature of the liquid Helium, confirming the elusive nature of the relation between the anisotropy barrier and the blocking temperature.

Hence the research regarding this new class of compounds was dedicated to increase the anisotropy barrier acting on the rare earth by en-

Interaction	Energy (cm^{-1})
Inter electron interaction	$10^4 \div 10^5$
Spin-Orbit coupling	10^3
Crystal field interaction	10^2
Magnetic field 10^4 Gauss	1
Hyperfine coupling	$10^{-3} \div 10^{-1}$

Table 1.1: Magnitude of main electronic interactions involved with lantanide ions in crystals.

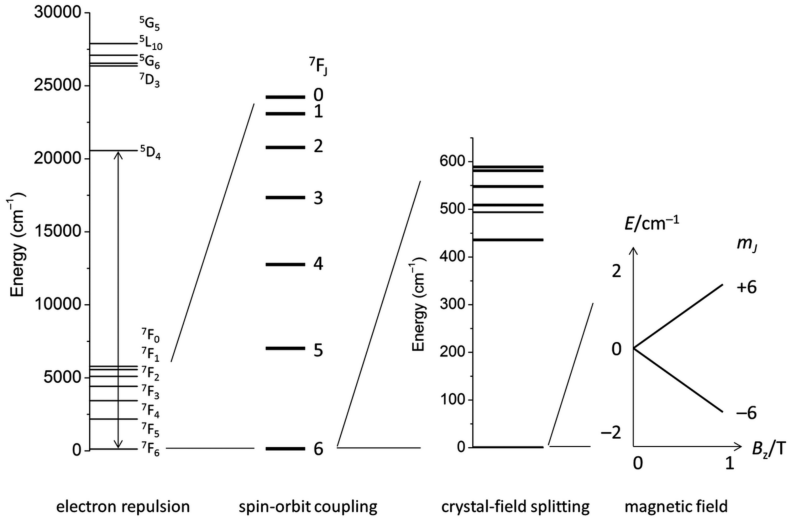

Figure 1.3: Main electronic interactions in lanthanides and their magnitude. The picture is taken from Liddle and Van Slageren[27]

gineering the ligand field around the anisotropic centre: in order to find higher and higher values of U, the electrostatic field generated by the ligands should be tuned in order to accomodate in the most favourable energetic configuration the f-orbitals electronic density of the free ion.[29] Several theoretical works showed how the perfect axiality of the ground doublet and a near bilinear coordination geometry are important features leading to SIMs with high anisotropy barriers.[30,31] With such design criteria the actual record for U has reached 1815 K in a pentagonal bipyramidal Dy(III) complex.[32] Finally, this year the previous record values of the blocking temperature has been broken by a Dy mononuclear metallocenium[33,34] that shows magnetic hysteresis until 60 K, an order of magnitude higher than the one observed until now.

However, the hysteresis of SIMs are usually affected by the presence of very low, or absent, remnant magnetization at zero-field due to the presence of Quantum Tunneling of Magnetization,[3–5] (QTM). QTM is one of the main issues to solve in order to employ this class of systems as real devices. Indeed, it limits the MN behaviour only at temperatures of few K due to the possibiltiy for the spin to relax the magnetization without the necessity to overcome **U**: due to transversal terms of the spin Hamiltonian, localized wavefunctions are not eigenfunctions of the Hamiltonian of the system and the spin has a non-zero probability to reach the other side of the double well potential tunneling through the anisotropy barrier. As it

will be shown in the next chapter (see for example equation 2.4), the QTM rate is inversely proportional to the energy difference between levels[35] and, therefore, it is usually quenched by applying a magnetic field that increase the separation between levels. However, for practical application the QTM should be suppressed at zero field in order to have a non-negligible remnant magnetization.

An other research line in this area was therefore devoted to the reduction of ω_T, the tunneling splitting, by reducing the mixing of the states on the two sides of the barrier. The transversal terms responsible for the temperature independent QTM are: i) rhombicity and superior terms of the zero field splitting, which becomes not-negligible when the molecule possesses a low symmetry group; ii)hyperfine coupling due to presence of magnetically active nuclei in the molecule; iii) dipolar coupling due to the spin-spin interaction with other molecules in the crystal lattice. Several strategies can be pursued in order to overcome each one of these limitations. Transversal rhombicity terms of the crystal field would vanish in molecules characterized by an high axiality symmetry, as already written: this strategy has been the most successful one and led to the already cited SIMs with high anisotropy barriers. However, at zero-field and low temperatures the spin-spin interaction becomes the main source of QTM. Even a small dipolar coupling between unpaired electrons localized on neighbours molecules in the crystal can open the temperature-independent relaxation path: the magnitude of the dipolar interaction can be reduced by dilution of the sample in a diamagnetic matrix, but this appears to be effective also at distances greater that 40 $\AA$. In order to increase further the distance dilution above 1:1000 would be necessary. To accomplish, it would make the magnetic measurement unfeasible or not reliable. An other method recently proposed able to supress spin decoherence is the exploitation of the 'atomic clock transitions':[11] a large tunneling gap derived from hyperfine coupling in an Ho(III) SIM leads to flat energy surface in function of the magnetic field, protecting the spin from dipolar interaction with the environment. Isotopic substitution of the magnetic active nuclei showed to influence and control the QTM[36] leading to the opening of the hysteresis loop.[37] Even if promising, this is a very expensive strategy: the synthesis of isotopically pure derivatives is a really hard task since it requires expensive reagents and solvents. The last adopted strategy is also the most interesting from the chemical point of view, because lies only on a tailoring of the synthetic approach: the pursue of exchange coupling between magnetic centers.

1.3 Heterospin Systems and Single Chain Magnets

In order to overcome the limitation produced by QTM the combination of different types of spin carriers (lanthanides, transition metals, organic radicals) within the same molecular entity represents actually the most valuable synthetic strategy in order to obtain single molecule magnets. The interest in these compounds arose in order to reach two main purposes. The first one is the possibilty to suppress, via exchange coupling, the QTM.[27,38] Indeed, as previously written QTM is suppressed removing the level degeneracy by the application of a magnetic field. Ferromagnetic coupling can, in principle, protect the molecular spin from the environment acting as an effective magnetic field able to localize the spin on one side of the barrier preventing from tunneling.

The second one is the possibility to reach higher anisotropy barriers increasing the total spin multiplicity **S** of the ground state by exchange coupling between different magnetic centers. Even if Waldmann[24] shows that, for the same molecule, the barrier is almost independent of **S**, the highest theoretical anisotropy barrier is reached within the state with the highest spin multiplicity, and ferromagnetic exchange is easier to reach in heterospin systems. Indeed the $3d$ and $2p$ orbitals do not have spherical symmetry and do not point in every direction of space. As a consequence, the orthogonality of the magnetic orbitals is therefore simpler to obtain. Low magnitudes of antiferromagnetic contributions, which are proportional to the overlap between semi-occupied MOs, are present. This fact leads to an overall ferromagnetic interaction.

However in the case of coupled magnetic centers with different numbers of unpaired electrons, e.g a metal ion and an organic radical, the total multiplicity can reach quite high values even if the interaction is antiferromagnetic, resulting in a ferrimagnetic ground state. This last strategy is the so called 'metal-radical approach' and it was successfully applied to obtain the first 1D ferrimagnet[39] (*vide infra*) which shows slow relaxation fo the magnetization. It was composed by high spin Co(II) ions ($S = 3/2$) bridged by NNit organic radical ($S = 1/2$): even if the interaction between them is antiferromagnetic, the two spins of the two different species do not compensate leading to an ferrimagnetic coordination polymer.

The above mentioned strategy has been successful: the single molecule magnet that holds from 2011 up to 2017 the record blocking temperature[29] (14 K) is a binucler complex of Terbium ions bridged by N_2^{3-} radical while the actual single chain magnet with record blocking temperature (14

K) is made of Co(II) ions bridged by PyrenylNitronylnitroxide radical[40] (see chapter 6). This year a dimetallofullerene characterized by a giant exchange interaction between the two lanthanides was recently reported and it shows a remarkable high blocking temperature of 21 K, the second highest until now.[41] Therefore, even if these two records have been recently broken by the previous cited Dy mononuclear compound[33,34] that shows magnetic hysteresis until 60 K, the pursue of higher and higher blocking temperature via exchange coupling is still very promising. Heterospin systems will be the subject of the fifth chapter.

As already outlined, the last class of compounds that gained a lot of interest at the beginning of this century are the one-dimensional magnetic molecular-based systems, when a cobalt(II) ferrimagnetic chain (CoPhOMe) that exhibited slow magnetic relaxation and magnetic hysteresis was discovered:[39] it was called Single Chain Magnet (SCMs) or magnetic nanowire. Until this year the record blocking temperature for a SCM was comparable[40] with the record reported for SMMs (14K), and the computational investigation of this last system will be the subject of the last chapter of this thesis. An other SCM with similar structure showed the highest coercivity ever recorded[42](52 kOe at 6K), even larger than commercial hard magnet at room temperatures.

If a SMM can be considered a 0-Dimensional material, SCMs are the one-dimensional equivalent of an SMM. However, their static and dynamic properties shows unique features. The magnetization dynamics is strictly connected to the formation and propagation of domain walls along the wire: an energy quantum has to be spent to create the domain wall but after that the propagation does not require any energy. The reversal of the magnetization can therefore proceed as a landslide process after the first perturbation: this process is called Glauber dynamics[43] and can be solved analitically for one dimensional Ising chains. Also relaxation in SCMs can therefore be rationalized by an Arrhenius-like behaviour with a different but analogue meaning comparing to SMMs. It can be demonstrated that for Ising chains with the following hamiltonian, where each magnetic center is characterized by an easy-axis type single ion anisotropy D,

$$\mathcal{H} = -2J \sum_i S_{i,z} S_{i+1,z} \tag{1.7}$$

if $D >> J$, in details $D/J > 4/3$, the following relations are valid:

$$\begin{aligned} \tau =& \tau_0 e^{\frac{\Delta_\tau}{k_B T}} \\ \Delta_\tau =& \Delta_\xi + \Delta_A \qquad \Delta_\xi = 4JS^2 \qquad \text{(Finite size limit)} \\ \Delta_\tau =& 2\Delta_\xi + \Delta_A \qquad \Delta_\xi = 8JS^2 \qquad \text{(Infinite chain)} \\ \Delta_A =& DS^2 \end{aligned} \tag{1.8}$$

From the equations above, a complex dependence of the Glauber dynamics from the electronic structure can be evinced. The energy required to create a domain wall Δ_ξ can be extracted by the slope of the $ln\chi T$ vs $1/T$ curve without any assupmtion of the energetic structure underlying and it depends from the correlation length ξ. This energy can be equal to $4JS^2$ if the temperature is sufficently low that the correlation length is so high that defects inside the chain become important. The domain wall forms at the end of the chain, where the defect interrupts the coordination polymer: this is called 'finite size limit'. On the other side, if the temperature is suffciently high, the chain appears infinite due to the minor extent of the correlation length respectively to the distance between two defects: in that case $\Delta_\xi = 8JS^2$ because the domain walls form in the middle of the chain. The relaxation times, however, show an other prominent contribution: the same barrier to the reversal of the magnetization employed to rationalize the behaviour of SMMs. Δ_A can be extracted form the different slope of the $ln\tau$ vs $1/T$ after and before the transition from the finite to the infinite size regime and it provides information about the anisotropy of the ions consituing the chain.[43] From all of these cosiderations, depending of the relative strength of D and J, a molecular nanowire can present properties of both SMM and SCM regimes. This modulation can be quite interesting in order to develop new multifunctional materials.

Indeed in Glauber dynamics the energy barrier to the reversal of magnetization depends on the exchange coupling constants J between the units therefore it can be modulated by the interaction with light[44] because it can alter the exchange interaction between the units which constitute the SCM. Moreover the Glauber dynamics is a very robust process that can cohexist with collective reversal of the magnetizations like in SMMs, and this usually happens in short chains constituted by few repetitive units: in principle the long-range interaction along the chain could be broken by a perturbation that allows a fast collective reversal of small segments of the chains and accelerating dramatically the process. Then after the fast reversal, the switch off of the perturbation would reestabilish the slow Glauber dynamic.[43,44]

Chapter 2

Molecular Nanomagnets: Open Questions Through the Filter of the Computational Investigation

2.1 Lanthanides based Single Ion Magnets from an *ab initio* point of view

The treatment of mononuclear lanthanide based molecular nanomagnets by *ab initio* methods has to face two different order of problems:

- Reproduction of the static magnetic properties
- Rationalization of spin dynamics

In the last ten years *ab initio* calcuations proved to be able to reproduce with an high level of accuracy static magnetic properties of lanthanide SIMs, i.e. the magnetic anisotropy of the fundamental state, main values of the g-tensor and orientation of the main magnetic axes into the crystal frame. Moreover, the electronic structure of the ground atomic multiplet, the energy ladder, magnetization, static susceptibility as a function of the temperature and the crystal field terms can be also computed with a good level of confidence. Consequently, a computational support for different experimental techniques as, for instance DC[45] magnetometry, electron paramagnetic resonance[46,47] and cantilever torque magnetometry,[48] can be given. The second chapter of the thesis will be devoted to explain which kind of experimental data can be rationalized by an high level *ab initio* calculation.

In virtue of the inner-shell character of the f orbitals, the most successful computational approach to describe the magnetic properties of Lanthanides is definitely the Complete Active Space Self Consistent Field (CASSCF),[49] a multiconfigurational method able to take into account electronic static correlation, followed by the Complete Active Space State Interaction[50] (CASSI) which introduces the Spin-Orbit coupling (see next chapter). Once obtained a reliable electronic structure, the spin hamiltonian can be mapped on the computed eigenfunctions in order to extract all the required parameters. In this framework the *effective hamiltonian* and the Operator Equivalent[51] approaches are introduced. Atoms with an odd number of electrons, in presence of crystal field, have a fundamental doubly degenerate state that can be described by a pseudospin $\tilde{S} = \frac{1}{2}$. Indeed, the Kramers degeneracy theorem[52,53] states that for every energy eigenstate of a system with half-integer total spin, there is at least one more eigenstate with the same energy. In other words, every energy level is at least doubly degenerate if it has half-integer spin. In the pseudospin approach the interaction with a magnetic field is written taking into account the interaction of a pseudospin $\tilde{S}$ with a magnetic field H and an effective Landè *g-factor* g_{eff}.[51] So we have

$$\mathcal{H}_{eff} = \mu_B \Big(\mathbf{H} \cdot \mathbf{g_{eff}} \cdot \tilde{\mathbf{S}} \Big) \tag{2.1}$$

In this equation $\mathbf{g_{eff}}$ is a 3×3 matrix and implies that the magnetic interaction depends not only on the angle between the magnetic field and the pseudospin $\tilde{S}$ but also on relative orientation between them and the axis defined by the local symmetry. Depending on the relative values of the g-tensor, we are in presence of different types of anisotropy.

- $g_{xx} = g_{yy} = g_{zz}$. The system is isotropic. The interaction with the magnetic field is independent from the direction.

- $g_{xx} = g_{yy} \neq g_{zz}$. In this case, $g_{xx} = g_{yy} = g_{\perp}$ and $g_{zz} = g_{\parallel}$. If $g_{\parallel} > g_{\perp}$, it is called *easy axis* magnetic anisotropy, i.e. the magnetization prefers to lie along a certain axis. If $g_{\parallel} < g_{\perp}$ it is named *easy plane* magnetic anisotropy and the magnetization prefers to lie on a plane.

- $g_{xx} \neq g_{yy} \neq g_{zz}$. The system is completely anisotropic. It is also called *rhombic*.

This hamiltonian can be employed also on systems with even number of electrons where the Kramers' theorem does not apply. If the ground and first excited states are quasi-degenerate in energy, the pseudo-spin

formalism is justified because the two states form a pseudo-doublet. For instance, this situation is common for Tb(III) in a low-symmetry environment as it will be shown in the next chapters.

The crystal field potential for lanthanides in the Operator Equivalent approach is usually expressed in the Steven formalism.[54,55] The hamiltonian has the form

$$V_{CF} = \sum_{k=2,4,6} \beta_k \sum_{q=-k}^{k} A_k^q \langle r^k \rangle \, \hat{\mathbf{O}}_{\mathbf{k}}^{\mathbf{q}} \tag{2.2}$$

where $A_k^q \langle r^k \rangle$ is a parameter, $\hat{\mathbf{O}}_{\mathbf{k}}^{\mathbf{q}}$ is the operator equivalent of the crystal field potential and β_k is a number, different for the different f^n configurations and for the different k values, which accounts for the proportionality between the electrostatic potential, expressed as a spherical harmonic of order k and the corresponding operator equivalent for that configuration. It is worth to stress that in low symmetry environments the access to these parameters by experimental method is extremely difficult since 27 parameters are in principle necessary to completely describe the ligand field surrounding a lanthanide ion. On the contrary, these parameters are straightforward accessible *ab initio*.[56] The number of parameters can be reduced in order to be extracted experimentally by symmetry considerations[57–60] but this approximation is justified only when the system has an exact point symmetry. In presence of pseudo symmetric elements this approximation is not valid as it has been demonstrated that the anisotropy in lanthanides is very sensitive to small geometric deviation from idealized geometries[61,62] (*vide infra*).

However, a clear understanding about some key aspects is still lacking: first of all a reliable reproduction of the ligand field around the lanthanide ion. The nature of the interaction between the ligands and the rare earths will be the subject of the third chapter of this thesis. In other words, the main problem is how to correctly take into account the electrostatic field and the orbital interactions between the f orbitals, the ligands and the crystal environment. Indeed, the idea that the $4f$ orbitals were not strongly involved in the coordination bond as their d orbitals counterpart supported the idea that a rationalization of the magnetic anisotropy in lanthanide complexes could be possible on the base of only electrostatic considerations. Several attempts were made following this idea, going from employing formal charges on the ligands[63] or more sophisiticated effective charge models.[64,65] The commmon mistake of these approaches is the underestimation of orbital interactions, which are accountable only with the explicit calculation of the whole electronic structure of the com-

plex. The role of each of the two contributions (orbital and electrostatic) can obviously vary from case to case but even if the former is expected to be, in general, smaller than the latter, completely neglecting a covalent contribution can be a risk.[62] Indeed, magnetic properties are really sensitive to small perturbations, like tiny deviations from idealized geometry[62] or varations of the bond distances, and such perturbations can reflect both on electrostatic and orbital contributions. In this framework not only the employment of the highest affordable level of calculation is necessary but also the choice of the model employed is crucial because it can seriously affect the results. In order to access a correct picture of the electrostatic field originated from the environment beyond the first coordination sphere a fine tuning of the models employed is necessary: without a reliable strength of the electrostatic field around the molecule the computational results could be affected by a model-dependent bias which can severely affect the reproduction and the prediction of the experimental behaviour. This aspect was deeply investigated and it will be described in the second chapter of this thesis.

The dynamic magnetic properties of single molecule magnets are usually investigated by AC magnetometry. From the real and imaginary part of the susceptibility recorded in presence of a static magnetic field, the relaxation rates in function of the temperature are extrapolated in order to define the process that allows the spin to overcome the anisotropy barrier:[1] the interaction of the spin with the phonon bath. The mechanisms of relaxation can assume several forms (direct, Orbach, first order and second order Raman) each one with a peculiar field and temperature dependence.[27,51] The interaction of the spin system with the phonon bath can be treated in two different ways. The first one, called Cotton-Waller process, assumes that the transition between the spin states are caused by the absorption of an electromagnetic wave emitted by the lattice at the right frequency. The origin of this oscillatory magnetic field is the vibration of the ions of the lattice due to the phonons. The transition probabilities w_{ij} between the levels are therefore directly proportional to the transition moments computed between the energy levels, where the perturbation is a fluctuating magnetic field.

$$w_{ij} = \frac{2\pi}{\hbar} |\langle i|\mu_{\pm}|j\rangle|^2 f(\omega) \tag{2.3}$$

In order to compute the terms between the levels it is, therefore, sufficient the static electronic structure of the molecule, because the terms w_{ij} are computable only with the total angular momentum of every state. Inside this approch it is also possible to give an estimante of the QTM

between states in Kramers'ions, where transversal magnetic field are the only possible source of tunneling inside a doublet. The common expression for QTM transition rate is the following [1,35]

$$\tau_{tunnel}^{-1} = \frac{2\omega_T^2 \tau_{mm'}}{1 + \frac{\tau_{mm'}^2 (E_m - E_{m'})^2}{\hbar^2}} \tag{2.4}$$

where ω_T is the tunneling splitting, $\tau_{mm'}$ is the transition rate and $E_m - E_{m'}$ the energy difference between levels on the opposite side of the barriers. QTM rate is proportional to term $\langle i|g_\perp \mu_B \hat{S}_{x,y}|j\rangle$ where $g_\perp$ is the perpendicular component of the g tensor, and this is the reason why the obtainment of an highly axial doublet became such an important design-criterion.

Actually this approach is the most wide-spread to rationalize dynamics in SIMs. [66–68] However this mechanism is not sufficient to explain the observed relaxation rates: it can only provide a qualitative relaxation path between the energy levels. In this thesis the AC data have been analysed inside this theory but we have to be aware that an other much more complex and time-comsuming approach is currently under development. Indeed in order to recover the experimental data an other more efficient mechanism has to be taken into account: the Van Vleck spin-phonon coupling. This mechanism relies on the modulation of the ligand field itself by the lattice vibrations. Hence the transition rates do not depend anymore on the static molecular structure but on the derivatives of the ligand field parameters in function of the distortions induced by the phonon vibrations. In order to access these derivatives a huge quantity of single point electronic structure calculations are necessary, proportional to the number of phonon modes inside the unit cell. Therefore the high level of theory necessary to treat in a quantitative way the spin-phonon coupling is not a simple task. Only few articles investigated this topic. [33,34,69–72] However, the results showed that such an analysis is absolutely necessary in order to improve the properties of SMMs towards real devices. Indeed the results obtained from a Cotton-Waller analysis can lead to overestimation of the energy barrier and to an uncorrect interpretation of magnetic data.

For instance, the paper from Lunghi *et al.* pointed out the importance of anharmonicity, [71] i.e. the finite line-width of the phonon mode, in decreasing the effective energy barrier from the one expected by the spacing of the electronic levels. In the same paper the importance of the lower lying phonon modes to promote the relaxation was evidenced. In a following paper, [71] the necessity of a selective engineering of the spin-phonon coupling was pointed out: organic ligands with high stiffness in order

to shift up the frequency of the vibrational modes and reduction of the molecular size in order to have small contribution of the magnetic center to the low-lying phonons. Finally, the analysis performed on the vibronic coupling of the Dysprosocenium molecule[33] individuated the main vibrations responsible for relaxation: the calculation suggested how to improve performances by acting on the substituent of the ligands. The same paper for the first time included second order effects computing the contribution to the relaxation rate due to the Raman mechanism.

Summarizing, a reliable treatment of the crystal environment and the simulation of the dynamic properties are now the two main challenges toward a deep understanding of the lanthanide containing molecular nanomagnets and both themes have been treated in the fourth and fifth chapter of this thesis.

2.2 Interaction of the magnetic centers between themselves

A huge quantity of *2p-4f* and *3d-4f* heterospin systems have been synthesized in the last years and exaustive reviews are available[6,73,74] but, despite the amount of compounds, theoretical studies on the nature of lanthanide-radical and lanthanide-transition metal interactions are not common. Indeed the theoretical treatment of the exchange coupling in presence of strong spin-orbit coupling requires a very complex Hamiltonian: in order to describe adequately **J-J** and **J-S** exchange interactions higher order terms are necessary in addition to the simple Heisenberg bilinear form $J \cdot S$ or $J \cdot J$. For this reason most part of the studies in the field deal with the isotropic Gadolinium ion coupled with different types of radicals and metals, i.e. Cu(II).[75–77]

The most considerable one is the *ab initio* characterization of the dinuclear terbium compound sythesized by Rinehart *et al.*[29] where a whole new theory was developed.[78] However, the interest in this system arose due to the magnitude of the magnetic exchange coupling, about tens of wavenumbers, comparable with the crystal field splitting between levels. Indeed in the most part of *2p-4f* heterospin compounds the exchange coupling is at least an order of magnitude smaller than the crystal field interaction and, therefore, it is usually rationalized as a perturbation of the ligand field levels. Therefore, assuming that the exchange interaction in heterospin systems is determined only by orbital overlap and exchange integrals, and that the spin-orbit doesn't affect the orbital's shape, two methods are usually employed.

The most common approach relies on the Lines' model:[79] it is a phenomenological method that allows to simulate the magnetic data by employing an effective exchange hamiltonian[80–83] and implemented into the POLY_ANISO software.[84] At first the electronic structure of each magnetic center is computed at the CASSCF/CASSI-SO level. Then each magnetic interaction between centers is described by an Heisenberg-like isotropic exchange interaction, i.e. a single exchange parameter for each interaction between centers is necessary. So the hamiltonian has the form

$$\mathcal{H}_{Lines} = -\sum_{i=1}^{N_c}\sum_{j>i}^{N_c} J_{ij}\tilde{\mathbf{S}}_\mathbf{i}\cdot\tilde{\mathbf{S}}_\mathbf{j} \tag{2.5}$$

where $\tilde{\mathbf{S}}_\mathbf{i}$ are pseudospin operators. The terms of the exchange matrix are then computed on the basis of the previously computed spin-orbit states. Depending on the system, only the low-lying states are included in the basis. The resulting picture is supposed to represent the anisotropic exchange coupling states of molecules characterized by strong spin-orbit interaction as lanthanides or d^7 ions as Co(II). This model is in principle exact when we are in presence of perfect isotropic or perfectly axial magnetic centers. In the first case the Lines' model reduces to the Heisenberg model, in the second to the Ising one. However, also in the intermediate cases, it can be a good approximation.

The exchange coupling constants J_{ij} are the only parameters of this model which allows to fit the susceptibility and magnetization data. Also the dipolar exchange interaction can be included in this approach. However, this method does not give any deeper information about the nature of the magnetic interaction, it allows only to estimate the magnitude of the dipolar and exchange part of J. In order to have information about the orbitals involved and the exchange paths the computation of the magnetic coupling *ab initio* is necessary.

The second approach is the computation of the exchange coupling by DFT method. The anisotropic lanthanide ion is substitued with the isotropic gadolinium and the energy of the states are computed by DFT. The energy values are then mapped on a broken symmetry Hamiltonian (see next chapter) and the extrapolated coupling constants are rescaled on the spin multiplicity of the anisotropic lanthanide ion:[85,86] the computed J is divided for the spin of Gadolinium (7/2) and multiplied for the real spin of the lanthanide, not taking into account the orbital contribution to the angular momentum. Calculation have been also performed without this isotropic substitution,[86] but the agreement with the experimental fitted values is very poor compared to the rescaling approach. From these calcu-

lations further insights about the electronic mechanism are extrapolated: overlap integrals,[87] natural bond order analysis[86] and possible axchange paths. Sometimes the Lines' constants that best simulate the magnetic data are compared to the computed values[81,86] by DFT.

Despite DFT showed along the years to reproduce with a good level magnetic properties of transition metal and lanthanide containing systems, here in this thesis we will propose a method to access these constants completely *ab initio*: these constants can therefore be compared to the best Lines' constants employed to simulate experimental data. The computation of these constants by *post*-Hartree Fock method is not unnecessary, as it could appear due the striking advances made by DFT. Indeed there are cases where DFT is not able to reproduce not even the sign of the magnetic interaction. An alternative approach based on a robust teoretical framework as the CASSCF method could be valid. The advantage could be a method not based on a 'black box' tool as a density functional whose single terms are not fully justified from a theoretical point of view. In the CASSCF method instead the approximations (i.e. number of active orbitals, extension of the basis sets) are known and therefore offers different options to improve the calculation without undermining the robustness of the approach. A method able to compute the exchange coupling constant completely *ab initio* will be proposed and discussed in the fifth chapter of the thesis.

2.3 Single Chain Magnets: from the bulk to the adsorption on surface

Once defined the *post*-Hartree Fock protocol able to reproduce the desired properties, a DFT based theoretical approach needs to be tuned in order to extend our computational protocol towards extended periodic systems. Indeed, regarding the bulk behaviour of magnetic systems, such a type of analysis is necessary in order to study i) a large variety of effects inherently determined by an extended periodic structure like Madelung potentials, ii) to perform structure optimizations when X-ray resolved geometries are not available, iii) to investigate coordination polymers, like SCMs, where the gas-phase approxiamtion usually employed for isolated molecules is not justified. However this step forward is not affordable by means of *post*-Hartree Fock methods, since these are not implemented in softwares that employ periodic boundary conditions to treat periodicity in the three direction of space. Several pDFT studies instead have demostrated to reproduce the spin topology of SMMs and in bulk systems[88,89] with an

high level of accuracy.

However the possibility to reproduce with an high level of confindence the bulk properties of these systems allows the intriguing exploration of the actual 'no man's land' in nanoscale sciences: the behaviour at the interface. More specifically, the interaction of molecular nanomagnets with surfaces in order to employ molecular systems in real devices. Indeed pDFT can simulate the surface 2D periodicity in order to have informations on the favorite adsorption geometries,[90] on the eventual surface/molecule electromagnetic interactions,[91] on the chemical-physical nature of the adsorption,[92] on the self-organization of molecules@surface.[92] The method can range from a 'simple' optimization of the molecule on the surface to *ab initio* molecular dynamics. Then the theoretical results can be extensively employed to rationalize experimental data recorded by a wide variety of techniques: for instance local probes, such as scanning tunneling micoroscopy (STM), give information about structure with atomic resolution; non-local techniques, such as x-ray and ultraviolet photoemission spectroscopy (XPS and UPS), are correlated to the electronic structure while other ones as X-ray Magnetic circular Dicroism (XMCD) give the possibiliy to observe the magnetic structure of adsorbed molecules on surfaces. All these informations can be fragmentary puzzle without a first-principle access to the geometric and electronic structure of the adsorbed molecules able to pick and link the different pieces.

In this framework the computational investigation of Single Chain Magnets is a triple challenge, as it will be described in the last chapter. Firstly it gives the possibility to study an inherently periodic system like a one dimensional coordination polymer, which are systems still at the frontier of the computational science despite the exponential increasing interest on Metal Organic Frameworks (MOFs) during the last years. Secondly, up to date it would be one of the few studies of SCMs performed fully-periodic,[93,94] i.e. by means of pDFT methods, and it would be the first approached with a mixed Gaussian-Plane Waves method as impleneted in CP2K[95] software. Finally, it would be the first study of an SCM@surface scenario.

Chapter 3

Multilevel Computational Method: from *post*-Hartree Fock to periodic Density Functional Theory

3.1 *Post*-Hartree Fock method: the *Divide et Impera* approach

The method employed in this work of thesis breaks the electronic structure calculation in two steps: first, a "spin-free" quantum computation, in which electron correlation and relativistic scalar effects are taken into account but where spin-orbit coupling is not considered; at this level of theory the reference wavefunction for the following spin-orbit calculation and/or the exchange coupling between different magnetic centers are computed. Then, a second step in which the spin-orbit coupling is introduced by computing this interaction among the different "spin-free" states. This "two-steps" approach assumes that: i) electron correlation and SO can be decoupled; ii) SO does not produce a large difference in the radial shape of the orbitals; iii) the main contributions to the spin-orbit coupling is due to the interaction among states close in energy. These last assumptions still must be tested in detail[96] and they will be discussed in the following chapters.

3.1.1 Complete Active Space Self Consistent Field: electronic correlation and exchange coupling

The first step consists in a Complete Active Space Self Consistent Field (CASSCF) calculation that treats the static electronic correlation. Complexes containing highly anisotropic ions, the subject of this thesis, are characterized by having a quasi degenerate electronic ground-state, therefore, Hartree-Fock and DFT are not adequate to generate correct reference states, due to their intrinsic mono-determinantal nature. The correct description of these systems is possible only taking into account electron correlation effects.[97] Electron correlation can be divided into dynamical and non-dynamical (static) correlation. Dynamical correlation refers mainly to the coulomb interactions among electrons of the same spin and can be taken into account through perturbation methods and also with the configuration interaction (CI) method. Static correlation is important for molecules where the ground state is well described only by more than one quasi-degenerate determinant, as transition metals and lanthanides: in these systems the d or f orbitals have almost the same energy and the defintion of a unique ground state configuration of electrons is not possible in the case a not spherical electronic symmetry is present. In all these cases the Hartree-Fock wavefunction, approximated to only one determinant, is qualitatively wrong. To account for electron correlation there are many *post*-Hartree Fock methods:

- *Multi Configurational Self Consistent Field* (MCSCF) in which the wave function is written as a linear combination of Slater determinants. It is able to account for static correlation and most part of the dynamic correlation. The principal approaches are the complete active space self-consistent field (CASSCF, *vide infra*), and the restricted active space self-consistent field (RASSCF, vide infra), Occupied Restricted Multiple Active Space (ORMAS) and Multi Reference Confuguration Interations (MRCI), a CI expansion truncated to singly, doubly or more excitations (MRCIS, MRCISD ecc).

- *Moller-Plesset perturbation theory* (MP2, MP3 ecc) which adds dynamical electron correlation effects by means of Rayleigh-Schrodinger perturbation theory (RS-PT), usually to second (MP2), third (MP3), or higher order. This method was extended to the CAS approach in the CASPT2 method[98] and in the NEVPT2 method.[99]

In a Full Configuration Interaction method all possible electronic configurations obtained by distributing the electrons of the quantum system

on the different molecular orbitals are considered, however it is not an accessible method because also for small molecules the number of excited determinants is enormous. Instead, the idea of the CASSCF is to reduce the number of electronic configurations by dividing the molecular orbitals into three types: inactive or core orbitals that are always doubly occupied; virtual orbitals that are always unoccupied; finally, the active orbitals that can be occupied by 0, 1 or 2 electrons. Therefore the different electronic configurations are obtained by arranging the "active" electrons in the molecular orbitals which belong to the active space (the active orbitals): a full CI of n-electrons in a subset m of orbitals set as 'active'. Finally the CASSCF wavefunction of a state is

$$|\Psi_I^S\rangle = \sum_k C_{kI} \, |\Phi_k^S\rangle \tag{3.1}$$

where $|\Psi_I^S\rangle$ is the N electron wavefunction for state I with total spin S. The set of $|\Phi_k^S\rangle$ is a set of configurations state functions (CSF), a linear combination of Slater determinats. The expansion coefficients C_{kI} are the first set of variational parameters. The CSF are constructed from a common set of orthonormal molecular orbitals $\psi_i(\mathbf{r})$ which are expanded in basis functions

$$\psi_i(\mathbf{r}) = \sum_\mu c_{\mu i} \phi_i \tag{3.2}$$

The molecular orbitals coefficients $c_{\mu i}$ form the second set of orbital parameters. The RASSCF is an extension of the CASSCF, where the active orbitals are partitioned into three other subgroups: RAS1 Orbitals where a maximum number of holes is allowed, RAS2 Orbitals where all possible occupation are allowed and RAS3 Orbitals a maximum number of electrons is allowed. Finally the Generalized Active Space (GAS) allows to define an arbitrary number of subspaces each one with its maximum occupation and excitation numbers.

Hence in the CAS/RAS/GAS approach the number of determinats are reduced allowing its application even to larger molecules. However the choice of the active space becomes critical, since it should account for the static correlation energy for the most part. Hence different protocols can be defined depending on the type of calculation:

- If the CASSCF calculation aims to provide the exchange coupling constant between two or more magnetic centers, the active space should at least involve the molecular orbitals where the unpaired electrons reside: the seven $4f$ orbitals, the five $3d$ orbitals, the π^* antibonding orbitals of organic radicals. Even if it can seem quite

straightforward, the effect of the extension of the active space to some virtual orbitals, or towards the internal doubly occupied one has not been tested in detail, with few exceptions.[44,76] Some attempts have been performed in this work of thesis, but in the majority of the cases the active space employed has been the less extended one. However, such a conservative approach seems to provide quite confident results. The second main advantage of this method is that the computed states for the several spin-multiplicities are now eigenfunctions of the total spin operator $\mathbf{S^2}$, due to their multideterminantal nature. The spin-states can therefore be mapped on an Heisenberg Hamiltonian, which in some cases is more coherent with the Hamiltonian employed to fit and simulate experimantal data. This is not true for DFT methods (see chapter 5).

- For calculation aiming to compute the magnetic anisotropy lanthanide and transition metal compounds the active space usually consists, again, of the orbitals where the unpaired electrons reside: the seven $4f$ orbitals or the five $3d$ orbitals. Comparing to the previous case, however, even if the extension of the active spaces have been investigated,[62] this 'minimal' extension of the active space already proved to provide a reliable electronic structure, at least for the states low lying in energy. With this approach the computation of more than one magnetic center at a time is not possible: the magnetic anisotropy of each spin carrier have to be computed separately quenching the other ions/radical, i.e. turning heavy atoms into diamagnetic ions or adding artificially an electron to the radical's molecular orbitals where the unpaired electron resides. Since the spin-orbit coupling operator is applied on the CASSCF states, a large number of CASSCF states must be computed in order to include all 'spin-free' states in the SO coupling Hamiltonian matrix that can have a relevant contribution on the lowest-energy SO states. Because of that, individual CASSCF calculations for each 'spin-free' state are not affordable and state-averaged CASSCF calculations are performed. In such kind of calculations several states are computed at once, by optimizing the same molecular electronic wavefunctions for all the states instead of using individually optimized molecular electronic wavefunctions for each state. An additional advantage of this state-average CASSSF method is that it allows to have a balanced description of all the computed states and their energy differences.

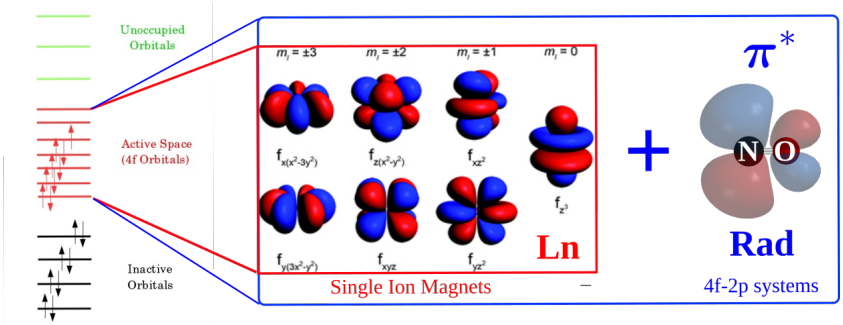

Figure 3.1: Examples of active spaces that can be defined for different classes of systems: the seven $4f$ orbitals for SIMs; $4f$ and π^* orbitals for Ln-rad systems.

3.1.2 Spin-Orbit Coupling: Complete Active Space State Interaction

When heavy atoms or orbitally degenerated ions are included in calculations, relativistic effects strongly affect the electronic structure of the molecule. The theoretical approach to account for the relativistic effects is based on the relativistic Dirac theory in which both the Hamiltonian and the wavefunctions have a 4-component form. However, due to the large number of degrees of freedom of the 4-components wavefunctions, the computational cost of this fully relativistic approach is too high for the study of molecular systems. For this reason several theoretical methods have been developed to reduce the 4-components Hamiltonian into an electronic 2-components one.[100] With these methods the hamiltonian reduces to a non-relativistic Schrödinger equation plus additional terms due to relativistic effects. The most used of such transformations leads to the second order Douglas-Kroll-Hess (DKH) Hamiltonian. The three main relativistic terms of the DKH Hamiltonian are called mass-velocity, Darwin, and Spin-Orbit coupling terms. The mass-velocity and Darwin terms, called scalar relativistic terms, can easily be implemented in a non-relativistic code. The quantum chemistry software employed in this thesis, MOLCAS[101] takes into account these two terms. Moreover since scalar relativistic terms affect significantly the radial shape of the orbitals, the employed basis-set should have been optimized by considering these scalar terms. The ANO-RCC[102] basis-set employed have been generated using the scalar relativistic terms of the DKH Hamiltonian and therefore it is suitable for relativistic calculations with that Hamiltonian.

On the other side, the treatment of the Spin-Orbit coupling term is

difficult since it produces a mixing of states with different spatial symmetry and with different spin. As a result, the simultaneous treatment of both SO coupling and electron correlation is very complex and it is not affordable for molecular systems. As previously written, the SO coupling is considered in the second step of the calculation, after the optimization of the multireference wavefunction, within the complete active space configuration interaction scheme.

The CAS State Interaction (CASSI) program forms matrix elements of the spin-orbit term over a wave function basis, which consists of CASSCF wave functions, each with an individual set of orbitals. Using these 'spin-free' eigenstates as a basis, it can compute spin-orbit interaction matrix elements, diagonalize the resulting matrix, and compute various matrix elements over the resulting set of spin-orbit eigenstates,[50] e.g. angular momentum necessary to map the magnetic anisotropy.

Complexes with arbitrary strength of spin-orbit coupling effects are, therefore, treated in a non-perturbative way by CASSI. This approach finally gives the multiplet eigenstates Ψ_i in the following form

$$\Psi_i = \sum_{i,rSM} c_{1,rSM}^{CASSI} \Psi_{rSM}^{CASSCF} \tag{3.3}$$

where the coefficients $c_{1,rSM}^{CASSI}$ are obtained via the diagonalization of the spin-orbit coupling matrix within CASSI, where r numerates solutions with the same S.[103] This approach allows to treat the spin-orbit coupling essentially in an exact way.

The dynamical correlation contributions can be possibly recovered by a CASPT2 approach but its inclusion showed not to improve significantly the results for complexes containing lanthanide ions.[61]

Finally it is worth to mention that in the computation of the SO operator, an additional approximation that reduces the computational time with a negligible loss of accuracy is the treatment of the two-electron terms as screening corrections of the dominating one-electron terms. The implementation of this idea is based on the use of atomic mean field integrals[104] (AMFI), which avoid the calculation of multicenter electron integrals. Since the short-range nature of the spin-orbit interactions, the one and two electrons spin-orbit integrals are computed for each atom separately: only the one-center integrals are considered exploiting the atomic symmetry with an high saving of computational cost.

3.2 Periodic Density Functional Theory

In order to treat magnetic materials constituted by transition metals by means of density functional theory, two main problems has to be faced. The first one is the necessity to find a protocol able to give reliable results for what concerns the magnetic properties and the electronic structure without requiring hardly affordable computational resources. The second one, but strictly connected with the previous, is the necessity to find an hamiltonian capable to map the magnetic properties in spite of the mono-determinatal nature of the DFT methods. The first problem can be solved by employiing the DFT+U Hubbard method[105] the second one by applying the broken symmetry formalism.[106,107]

3.2.1 Hubbard U method for magnetic complexes

One of the main limitations of DFT calculation is based on the approximated expressions for the different functionals that are usually optimized on *post*-Hartree Fock calculations or experimental data. The most common ones are constructed as expansions around the homogeneous electron gas limit and are not able to reproduce the properties of systems whose ground state is characterized by a more pronounced localization of electrons.[108] Density functionals based on Local Density (LDA) or Generalized Graident Approximation (GGA) overestimate the delocalization of the electrons and are therefore not suitable to reproduce parameters directly connected to the overlap of the molecular orbitals like density of states and magnetic exchange. In this category not only these species with d or f electrons are included, which are strong localized on the metal ions, but also the ones characterized with strong localized p orbitals. Hybrid functionals, including part of the Hartree-Fock exchange, are able to recover part of the one-site coulomb interaction but the computational times and resources required make this way difficult to choose in the perspective to use it on hybrid systems as SMM/SIM/SCM on surfaces. The basic idea behind DFT+U is to treat the strong on-site Coulomb interaction of localized electrons, which is not correctly described by LDA or GGA, with an additional Hubbard-like term. The strength of the on-site interactions are usually described by parameters U (on site Coulomb) and J (on site Exchange). These parameters U and J are usually obtained semi-empirically by reproducing sets of experimental data, for instance magnetic topology and/or UPS spectra.[89,90] However it is worth to stress that they can be also extracted from *ab-initio* calculations following the scheme proposed by Cococcioni and Gironcoli[109] in the linear response

theory framework.

The computational implementation of the DFT+U corrections is not univoque. The DFT+U corrections can be introduced in *ab initio* calculations in different ways. In the first one, introduced by Liechtenstein *et al.*[105] U and J enter as independent corrections in the calculations, while in the second one, proposed by Anasimov *et al.*,[110] only a single effective $U_{eff} = U - J$ parameter accounts for the Coulomb interaction. Energy correction can be expressed:

$$E_{DFT+U} = E_{DFT} + \sum_{a} \frac{U}{2} Tr(\rho_a - \rho_a \rho_a) \tag{3.4}$$

where ρ_a is the atomic orbital occupation matrix. As already said, U is often determined in a semi-empirical way, seeking agreement with available experimental measurement of certain properties and using the so determined value to make predictions on other aspects of the behavior of systems of interest. Moreover U values are element-dependent and oxidation state-dependent, it means that for each different state U should be reperformed from zero. This method however does not allow to appreciate the variations of the on-site electronic interaction U during chemical reactions, structural/magnetic transitions or, in general, under geometrical changes.

First applications of DFT+U approaches have been done for solid state physic band structure methods,[111] for instance to reproduce insulator's band gaps or energy loss-spectra. Subsequently it has been applied in quantum chemistry to get insights on reaction processes,[112] thermodynamic quantities,[113] metal complexes characterization,[114] adsorption processes.[115,116] This work of thesis aims to extend this approach to cobalt containing coordination polymers in order to have a computationally feasible method but also based on a solid tuning protocol.

3.2.2 Map of the magnetic properties by DFT

DFT methods represents the wavefunction as a single Slater determinant. This is not a problem for the state with the highest spin-multiplicity, usually well-described by a monodeterminantal wave-function. As a consequence the computed states with lower multiplicities are not eigenstates of the total spin-operator $\mathbf{S^2}$ but only of the spin projection operator S_z. This limitation doesn't allow to map the spin-states on the classic Heisenberg-Dirac-Van Vleck Hamiltonian for localized isotropic spins

$$\mathcal{H}_{HdvV} = -J_{ij} \sum_{i<j} \mathbf{S_i} \cdot \mathbf{S_j} \tag{3.5}$$

In order to overcome this limitation, the broken symmetry approach allows to compute eigenfunctions of the only spin projection operator S_z: such a method gives the possibility to extract the exchange coupling constants by using the following system of equations[117]

$$\Delta E(S_{max} - s) = \sum_{i<j} (2J_{ij}|S_i S_j|)\lambda_{ij} \tag{3.6}$$

where $\lambda_{ij} = 0$ if S_i and S_j have the same sign. From the previous equations it comes out that in order to extrapolate n exchange constants, $n + 1$ determinants are necessary. However for N spin centers $2^N/2$ states, usually much more than the $2n + 1$ necessary, can be computed and the arbitrary choice of the determinants to include inside the system of equations can lead to misleading results, as shown by Totti and Bencini.[118] To avoid such a possibility, for systems where N $>$ 2, it was proposed to compute all the possible determinants and after to perform a linear fitting of the J on all the BS-energies where for each determinant the energy expression is

$$E(BS) = \sum_{i<j} (J_{ij}|S_i S_j|)\lambda_{ij} \tag{3.7}$$

and the J_{ij} of the choosen spin topology are the fitting parameters. The best set of J_{ij} is obtained minimizing the test function

$$f = \sum_{S} [\Delta E^{DFT}(S_{max} - s) - \Delta E(S_{max} - s)]^2 \tag{3.8}$$

In this way, on the basis of values and possible internal determinants degeneracies, it is also possible to discern the goodness of the chosen spin Hamiltonian. Moreover, no further approximation deriving by the reduction of the number of determinants is assumed.

Chapter 4

Mononuclear Lanthanide Complexes

4.1 $Dy(LH)_3$

The origin of the peculiar magnetic behaviour of lanthanide ions lies in their strong magnetic anisotropy, stemming from the combined action of the spin-orbit coupling and the crystal field (CF) induced by the ligand(s) donor atoms, and by the large total angular momentum J (for the second half of the $4f$ series).[119] These two features originate, when the two states with the largest projection of J are the ground ones, an anisotropy energy barrier for the reversal of the magnetization. In the absence of other efficient relaxation paths it is then possible to observe slow relaxation of the magnetization through an Orbach process, with the thermal dependence of the relaxation rate following an Arrhenius-like behaviour. This result requires both a highly symmetric axial disposition of the ligands around the lanthanide centre - reducing the mixing between states with different M_J values - and a resulting ground state characterized by an M_J value as large as possible.[30] While it has been shown that complexes with lower symmetries can also possess axial eigenstates,[61,63,120] in these situations it is not possible to predict *a priori* the composition of the ground state, since several different $|M_J\rangle$ can in principle contribute to it.

It has further been pointed out that the relaxation of the magnetization can be due to different mechanisms.[66,121,122] For example, at low temperature and for small values of applied magnetic field, quantum tunneling of magnetization (QT) can be strongly effective in accelerating the relaxation. In this sense, molecules containing Kramers' ions are clearly to be

preferred, since in semi-classical approach QT is forbidden for semi-integer spins. However, this process can be mediated by dipolar and hyperfine interactions, so that in zero field fast relaxation of the magnetization is often observed. Suppression of the QT relaxation processes is then achieved by diluting paramagnetic complexes within an isostructural diamagnetic matrix, which reduces dipolar interactions, and/or by applying a static magnetic field.

On increasing magnetic field the direct process gains importance due to the larger number of available phonons of correct energy and can become the dominant contribution.[123] Finally, relaxation may occur through a Raman process that gives a more marked temperature dependence of the magnetic relaxation time τ, since an interaction with phonons from the thermal bath and virtual energy states is involved.[124] It is quite clear that to correctly describe the relaxation processes in these systems a detailed picture of the electronic structure of the lanthanide ion and its relation to the molecular structure is needed. Therefore an accurate *ab initio* characterization was performed to get more detailed insights of the Dy(III) electronic structure. An approach combining spectroscopic characterization (EPR, luminescence, Inelastic Neutron Scattering)and *ab initio* theoretical studies is now becoming the standard procedure for this scope.[47,61,125–128] The outcome of this experimental characterization can then be used to validate the results of *ab initio* calculations that, on their turn, help to unravel the knot and to avoid misinterpretation of the observed dynamic behaviour by providing information on the eigenstate composition and the corresponding energy gaps. In this chapter a complete experimental characterization, obtained by X-ray diffractometry, Electron Paramagnetic Resonance (EPR) spectroscopy, single crystal cantilever torque magnetometry (CTM), *AC* and *DC* susceptibility flanked by theoretical analysis based on *ab initio* methods of a new mononuclear Dy complex behaving as Single Ion Magnet in zero field will be presented. The complex has been synthesized using a potentially pentadentate ligand: however, only three of its binding sites are used to bind to the Dy ion, thus resulting in a neutral molecule which is in principle sublimable:[129] a future possible attempt to deposit it on surface is therefore possible.

4.1.1 Structure and Experimental Data

The 2-Hydroxy-N'-[(E)-(2-hydroxy-3-methoxyphenyl) methylidene] benzhydrazide ligand, LH_2 is a potentially pentadentate ligand, which possesses two functional groups that can be deprotonated: its coordination chemistry has, up to now, only been investigated with regard to nickel or

cobalt complexes.

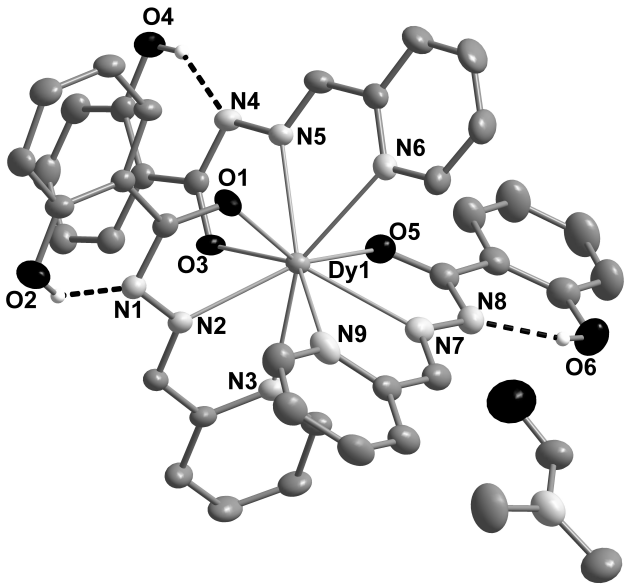

Figure 4.1: View of the asymmetric unit of **1**, including one molecule of the complex and one dmf molecule. The dashed lines evidence the three intramolecular hydrogen bonds stabilizing the structure. Remaining hydrogen atoms are not shown for clarity sake. Ellipsoids are drawn at 40% probability, with the exception of hydrogen atoms, for which ball and stick representation is used.

Molecular structure obtained by single crystal X-ray diffractometry indicates that $Dy(LH)_3$dmf (**1**) crystallizes in the monoclinic $P2_1/n$ space group. Its asymmetric unit (fig. 4.1) is made up of one mononuclear $[Dy(LH)_3]$ neutral molecule and one dimethylformamide (dmf) molecule. The Dy ion experiences a N_6O_3 coordination environment provided by the three tris-chelating LH ligands. The hydrazide function is deprotonated while the phenol function remains protonated and not involved in coordination with the Dy ion. Each ligand remains essentially planar, with the exception of the phenolic residues, due to the presence of an intramolecular hydrogen bond involving the non-deprotonated phenol function and the hydrazide nitrogen atom of each ligand. The Dy–N(pyridine) bond lengths, 2.574(3) Å to 2.696(4) Å, are slightly larger than the Dy–N(hydrazide) bond lengths, 2.496(3) Å to 2.538(4) Å, the shorter bonds involving the Dy–O of the hydrazone part of the ligand, 2.322(3) Å to 2.368(3) Å. Analysis of the nine-coordinate DyN_6O_3 polyhedron with the SHAPE pro-

gram[130] (see table S2) suggests that the coordination polyhedron is intermediate between the different possible choices for a nine coordination, with a slight preference for a spherical capped square antiprism. For this choice the capping atom is the N7 hydrazide nitrogen one, and the two squares of the antiprism are made up by the N9 N3 O5 N6 and O1 N2 O3 N5 atoms. In order to reduce the effect of intermolecular interactions and of demagnetizing fields due to shape anisotropy, we chose to use a sample of the isostructural Y(III) derivative doped with ca. 10 % Dy(III), hereafter **2**. The isomorphicity of the diluted compound **2** with the pure one was checked with a Single Crystal diffractometry.

The static magnetic properties of a microcrystalline powder sample of **1** and **2** were investigated by means of *DC* measurements and the behaviour of the magnetization was studied both as a function of field H and temperature T. The χT *vs* T curve is reported in fig. 4.3: the room temperature experimental value ($\chi T = 13.97\,\mathrm{emu\,K\,mol^{-1}}$) is consistent with the free ion expectation one for Dy(III) ($^6H_{15/2}$, $g_J = 4/3$, $\chi T = 14.17\,\mathrm{emu\,K\,mol^{-1}}$). A smooth decrease is observed on lowering temperature, which is attributed to the depopulation of excited levels of the $^6H_{15/2}$ multiplet, split by the CF. The magnetization versus field was measured at 2 K and 4 K and it is reported in the lower part of fig. 4.3. The saturation value is $5\mu_\mathrm{B}$, as already observed for other molecular complexes containing Dy(III).

In our case the complex revealed to be silent to EPR spectroscopy. **1** was then investigated by using CTM. This technique exploits the magnetic torque of a molecule immersed in a homogenous magnetic field and has already proven to be extremely useful to determine the anisotropic features of lanthanide-based Single Molecule Magnets.[57,131,132] The resulting director cosines of the easy axis (z in molecular reference frame), with respect to abc^* are: $\cos\alpha_1 = -0.501$, $\cos\alpha_2 = 0.801$, $\cos\alpha_3 = 0.326$ ($\alpha_1 = 120°$, $\alpha_2 = 37°$ and $\alpha_3 = 71°$). Due to the presence of two magnetically non equivalent molecules in the unit cell these direction cosines can identify two possible orientations for the magnetic anisotropy axis with respect to the molecular structure, see fig. 4.2. It is interesting to note that none of the two possibilities correlate with the highest symmetry axis (C_4 or C_3) of the best fit coordination polyhedra, capped square antiprism or tricapped trigonal prism. This is in agreement with the fact that the idealized structural geometry does not take into account the heterolepticity of the complex, which results in a CF symmetry completely different from the structural one.

Atom	Label	Primitives	Contraction
Dy	VTZP	[25s22p15d11f4g2h]	[8s7p5d3f2g1h]
N	VTZP	[14s9p4d3f2g]	[4s3p2d1f]
O	VTZP	[14s9p4d3f2g]	[4s3p2d1f]
C	VDZP	[14s9p4d3f2g]	[3s2p1d]
H	VDZ	[8s4p3d1f]	[2s]

Table 4.1: Contractions of the ANO-RCC basis set used for *ab initio* calculations of $Dy(LH)_3$.

4.1.2 *Ab initio* calculations: computational details.

The quantum chemistry package MOLCAS 8.0[101] was employed in all the calculations. X-ray structure resolved from the diffraction pattern recorded at 180 K was used throughout the study. All atoms were described with standard all electrons ANO-RCC basis set. TZP basis set was employed for dysprosium, nitrogen and oxygen atoms (see table S8). DZP and DZ for Carbon and Hydrogen atoms. respectively. The default contraction scheme was not altered. The Douglass-Kroll-Hess hamiltonian was employed in order to take into account scalar relativistic effects. The spin-free wave functions were obtained with the Complete Active Space Self Consistent Field (CASSCF) method for a state-average calculation of all roots arising from the considered active space. The active space consisted of nine electrons in the seven f orbitals of the lanthanide atom [CASSCF(9,7)]. The Spin-Orbit interaction was considered in the following Restricted Active Space State Interaction (RASSI) calculation by mixing all the state-averaged obtained 21 sextuplets. The g-tensor for every Kramers doublet and his orientation in the molecular frame, the crystal-field parameters and their decomposition in wavefunctions with definite projection of the total moment $|J, M_J\rangle$ were computed with the SINGLE_ANISO package. The quantization axis was chosen to be the main magnetic axis of the ground doublet.

4.1.3 *Ab initio* calculations: discussion.

A first relevant test about the correct reproduction of experimental properties concerns the calculation of the orientation and magnitude of the magnetic anisotropy compared to the results of CTM. In agreement with the experimental CTM results the calculated ground Kramers' doublet shows an almost pure Ising character with a principal value of $g_z = 19.8$ (see ta-

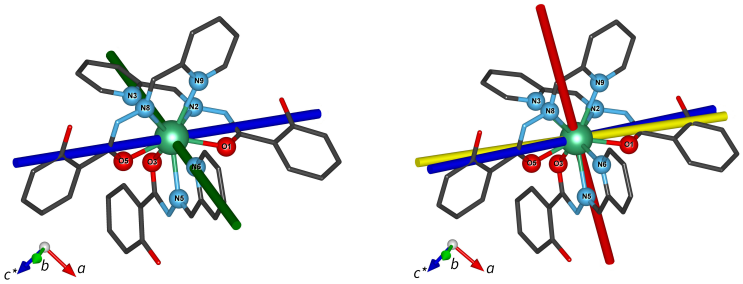

Figure 4.2: (a) two possible directions of the easy axis of magnetic anisotropy as determined by CTM: the blue one is substantially coincident with the calculated one. (b) direction of the easy axis anisotropy for the first three energy doublets: ground (blue), first excited (yellow), second excited (red) computed direction.

ble 4.4) and contribution from $M_J = \pm 15/2$ only. The computed easy axis orientation for the ground doublet (fig. 4.2) approximately lies on the line connecting two carbonyl oxygens of two LH ligands ($\cos\alpha_1 = -0.531454$, $\cos\alpha_2 = 0.788731$, $\cos\alpha_3 = 0.308967$). It is evident that the calculated direction is almost coincident with one of the two possible choices provided by the CTM analysis (see above and fig. 4.2), the angle formed by calculated and experimental orientation being 2.9°, which is below the estimated experimental uncertainty (5°). The calculated *ab initio* anisotropic properties are then perfectly consistent with the results of the CTM investigation. With this proof of the reliability of *ab initio* calculations we used the set of calculated Stevens' Spin Hamiltonian parameters[133] (see table 4.3) pertaining to the ground $J = 15/2$ state to simulate the static magnetic properties of the complex using the home-developed software EVALUCF.[121] In particular, while the correct simulation of the M *vs* H curves at low temperature confirms that the ground doublet properties are well reproduced by *ab initio* calculations, an indication about the correct evaluation of energy splitting and eigenstates of the ground $J = 15/2$ state can be provided by the simulation of the χT *vs* T curve. For this quantity, the agreement between experimental and calculated curve (see upper part of fig. 4.3), apart for a small scaling factor within experimental error ($< 5\,\%$), lends further support to the electronic structure obtained by *ab initio* calculations. This is reported in term of computed energy splitting[133] between the Kramers' doublets and of their composition (M_J contributions larger that 0.1) in fig.4.4. The calculated energy separation between ground state with the first and the second excited state is 195 and 237 cm^{-1}, respectively.

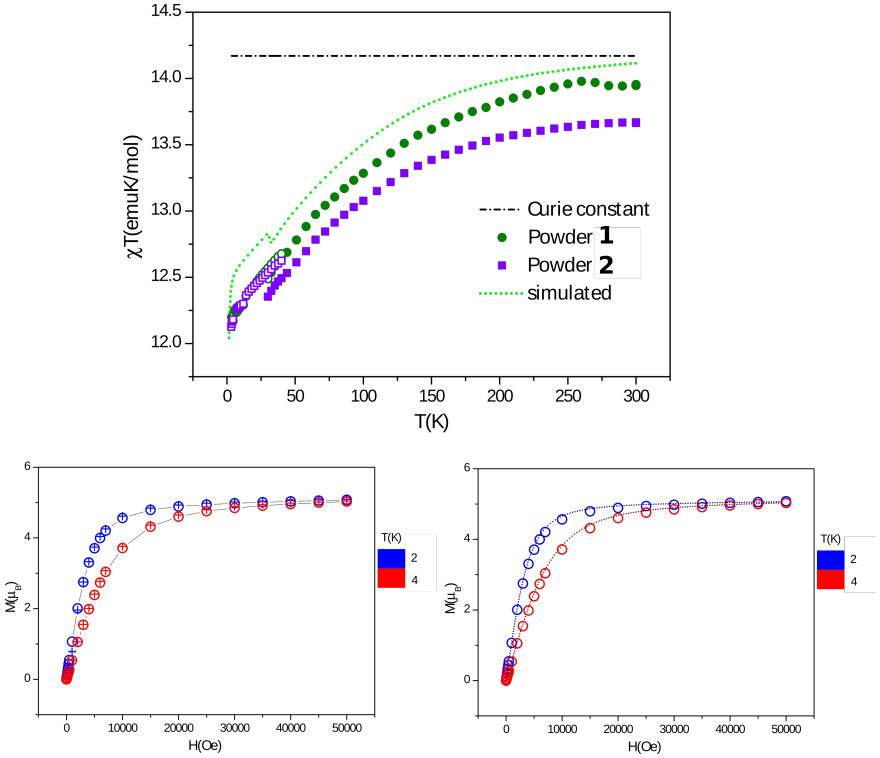

Figure 4.3: (Top)Temperature dependence of χT of **1** (circles) and **2**(squares) along with theoretical curves (dotted line) calculated by using CF parameters derived from ab initio calculations. The dashed line corresponds to the expected free-ion χT value. The empty circles and squares correspond to an applied static field H of 1000 Oe while the full ones to a field of 10 000 Oe. The difference observed for the two fields is to be attributed to saturation effects which are well reproduced by the theoretical prediction. (Bottom) Empty circles represents the behavior of magnetization versus field at 2 K and 4 K for **1** (left) and **2** (right), while the dotted lines are the simulation calculated with the CF parameters extracted from *ab initio* calculations.

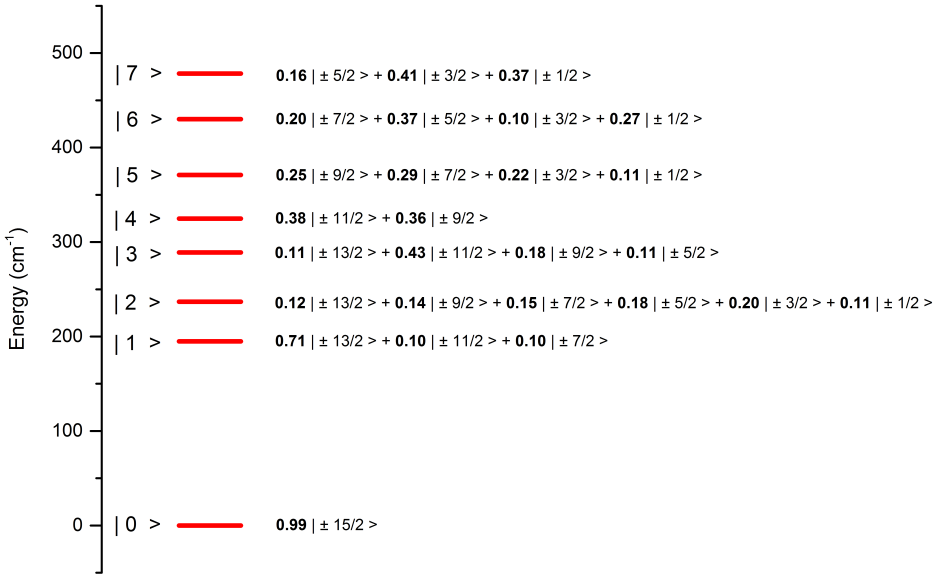

Figure 4.4: Energy splitting and prominent contributions of the M_J components for the eight Kramers'doublet.

The first excited doublet shows a prominent contribution from the $\pm 13/2$ components with only the $\pm 11/2$ and $\pm 7/2$ ones as minor contributions, which are nevertheless enough to induce appreciable deviations from the axiality of the **g** tensor. A much larger mixing among different M_J components is observed for the third excited doublet, while for the fifth excited doublet the axiality is completely lost. It is to be stressed that in addition to the increased rhombicity, the non-collinearity of the easy axis with respect to the one of the ground state is also increasing with the energy of the doublets (see director cosines in table 4.4 and fig. 4.2). Indeed the easy axis of the ground doublet forms an angle of 6° with the easy axis of the first excited doublet and of about 60° with the one of the second excited doublet.

In this framework, the calculations suggest that if magnetic relaxation occurs only via an Orbach two-phonon mechanism, this should likely involve the second excited state. In such a case the energy barrier to be overcome would be of the order of 230 K, thus indicating the possible observation of an overall slow relaxation rate at relatively high temperatures.

Stevens' parameter					
	cm^{-1}		cm^{-1}		cm^{-1}
B_2^0	314.1	B_4^0	57.3	B_6^0	−21.7
B_2^1	−24.9	B_4^1	59.8	B_6^1	31.5
C_2^1	−24.9	C_4^1	−39.2	C_6^1	−23.2
B_2^2	−103.0	B_4^2	21.6	B_6^2	1.2
		B_4^3	13.5	B_6^3	33.9
		C_4^3	5.1	C_6^3	33.9
		B_4^4	−24.6	B_6^4	−8.2
				B_6^5	2.2
				C_6^5	−13.8
				B_6^6	−16.2
				C_6^6	32.3

Table 4.2: Crystal field parameters of the Crystal field Hamiltonian $\mathcal{H}_{CF} = \sum_{n,m} \alpha_n [B_n^m O_n^m + C_n^m W_n^m]$, where the operator O_n^m and W_n^m are defined in[133] and the α_n are the Stevens' coefficient for the lanthanide.

Energy Levels		(cm^{-1})
$^6H_{\frac{15}{2}}$	E_0	0
	E_1	195
	E_2	237
	E_3	289
	E_4	324
	E_5	371
	E_6	430
	E_7	478
$^6H_{\frac{13}{2}}$	E_8	3082
	E_9	3159
	E_{10}	3240
	E_{11}	3294
	E_{12}	3320
	E_{13}	3355
	E_{14}	3382

Table 4.3: Results of the calculations with RCC basis sets for $Dy(LH)_3$: energy splitting of the $^6H_{\frac{15}{2}}$ (ground) and the $^6H_{\frac{13}{2}}$ multiplets.

Principal g-values		a	b	c^*
			Ground Doublet	
g_x	0.0	0.505 440	0.587 959	−0.631 533
g_y	0.0	−0.679 770	−0.179 466	−0.711 130
g_z	19.8	−0.531 454	0.788 731	0.308 967
			First Excited Doublet	
g_x	0.5	0.655 910	0.696 041	−0.292 076
g_y	1.8	−0.460 955	0.062 932	−0.885 189
g_z	14.9	−0.597 747	0.715 239	0.362 121
			Second Excited Doublet	
g_x	0.1	0.390 680	−0.551 943	−0.736 701
g_y	2.2	0.651 787	0.731 000	−0.202 023
g_z	14.3	0.650 033	−0.401 246	0.645 336
			Third Excited Doublet	
g_x	1.5	−0.859 388	0.048 208	−0.509 047
g_y	3.7	−0.497 180	−0.311 322	0.809 871
g_z	12.1	−0.119 435	0.949 081	0.291 514
			Fourth Excited Doublet	
g_x	0.6	0.913 581	0.226 644	0.337 642
g_y	2.8	−0.374 290	0.144 034	0.916 057
g_z	13.8	0.158 987	−0.963 269	0.216 418
			Fifth Excited Doublet	
g_x	2.6	0.897 009	0.315 330	−0.309 745
g_y	4.5	0.047 565	0.627 828	0.776 897
g_z	8.8	0.439 446	−0.711 617	0.548 169
			Sixth Excited Doublet	
g_x	3.4	−0.369 322	−0.878 165	0.304 018
g_y	4.1	0.873 695	−0.439 584	−0.208 384
g_z	7.4	0.316 637	0.188 658	0.929 596
			Seventh Excited Doublet	
g_x	1.1	0.549 731	−0.830 355	−0.091 138
g_y	4.7	0.423 687	0.183 132	0.887 103
g_z	15.9	−0.719 920	−0.526 282	0.452 484

Table 4.4: Results of the calculations with RCC basis sets for $Dy(LH)_3$: value of the main magnetic axis of the eight doublets of the ground multiplet and their orientation in the crystalline frame.

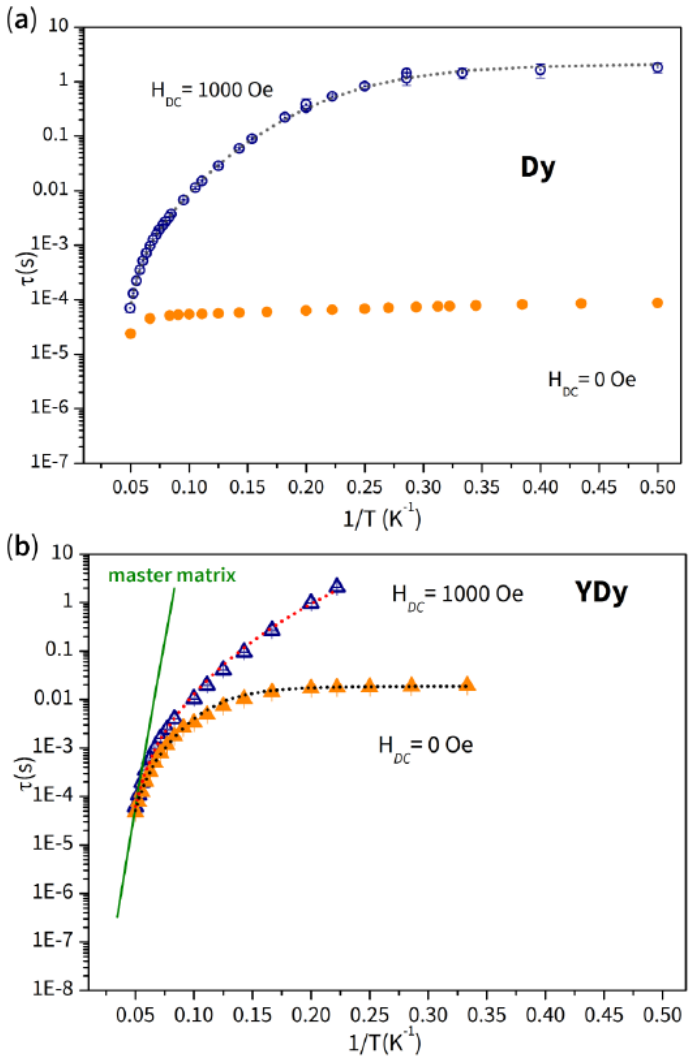

Figure 4.5: (a): relaxation times versus T^{-1} for compound **1**, in zero (full circles) and applied static field (empty ones). The relaxation in zero field is almost temperature independent up to 12 K. The grey dotted lines represents the best fit curve with $\Delta = 270$ K. (b): Relaxation times versus T^{-1} for compound **2**, in zero (full triangles) and applied static field (empty triangles). The dotted lines represent the fit of the relaxation time (see eq. 4.1) with $\Delta = 270$ K, the solid line is the relaxation time simulated using the master matrix equation.

4.1.4 Rationalization of magnetisation dynamics.

To have more insights on this important point, the dynamic magnetic properties of **1** were investigated performing *AC* magnetic susceptibility experiments, as a function of frequency (0.02 Hz to 10 000 Hz), temperature, and of *DC* applied field. This investigation revealed a composite dynamic magnetic behaviour between 2 and 20 K. The pure complex showed two different relaxation channels in zero and non-zero magnetic static field: the application of an external field allows to suppress one channel and activate the other one. The imaginary susceptibility curves χ'' in zero and applied field were fitted according to a Debye model[1,134] and the corresponding relaxation times versus T^{-1} is reported in fig. 4.5a. We notice that the relaxation rate of the channel dominating in zero field is almost temperature independent up to 12 K. The observed temperature dependence of the relaxation rate of **2** for both relaxation channel was reproduced by including three contributions, a Raman and an Orbach process and a temperature independent process:[125,135–137]

$$\tau^{-1} = CT^n + \tau_0^{-1}\exp(-\Delta/T) + B \tag{4.1}$$

A simultaneous fit of the relaxation time in field and in zero field (the corresponding parameters being indicated by *f* and *zf*, respectively, in the following) was performed, using the same set of parameters for Orbach process (τ_0 and Δ), while the Raman contribution was left free to vary for the two situations. This was intended to account for the possible contribution of direct process in the case of in-field measurements, which may affect the best fit value obtained for the Raman relaxation.

A first attempt was made by fixing the value for the energy barrier Δ at 270 K $\sim$ 195 cm^{-1}, that is the energy of the first excited doublet computed by *ab initio* calculations. With this precondition we obtained the following values for the best-fit parameters: $\tau_0 = 1.3(2)\times10^{-10}$ s, $n_f = 6.19(4)$, $C_f = 5.0(5)\times10^{-5}\,s^{-1}K^{-n}$, $B_f = 0$ (fixed), $n_{zf} = 5.5(2)$, $C_{zf} = 6(4)\times10^{-4}\,s^{-1}K^{-n}$, $B_{zf} = 53(2)\,s^{-1}$. The

In a second step the Δ parameter was left free to vary, providing as best fit values $\tau_0 = 1(2)\times10^{-11}$ s, $\Delta = 318(44)$ K (ca. 230 cm^{-1}), $n_f = 6.22(4)$, $C_f = 4.7(5)\times10^{-5}\,s^{-1}K^{-n}$, $B_f = 0$ (fixed), $n_{zf} = 5.6(2)$, $C_{zf} = 5(3)\times10^{-4}\,s^{-1}K^{-n}$, $B_{zf} = 53(2)\,s^{-1}$ It is clear from these results that while at low temperature Raman and QT dominate the relaxation, the Orbach process is active in promoting the relaxation in the high temperature regime. It is however not completely clear whether the latter process occurs via the first or the second excited doublet.

In order to obtain some more hints on the mechanism of the single-ion relaxation, transition moments between the states were computed[30,138] (see fig. 4.6). On the basis of these transition moments no efficient QT relaxation is expected for the ground Kramers' doublet: the underestimation of the probability of QT relaxation by transition moments with respect to the experimental results is clearly due to the fact that this method takes into account only purely electronic, single molecular properties, whereas zero-field QT in Kramers' systems needs residual dipolar interactions and hyperfine coupling to occur (in the present case the magnetic nuclei are Dy(^{161}Dy, rel. ab.= 18.9 % and ^{163}Dy, rel. ab.= 24.9 %, both with $I = 5/2$).[139] On the basis of the *ab initio* results a thermally assisted QT is likely to occur already for the first excited state. However, the magnetic moment matrix element computed for a quantum tunneling mechanism between the two components of the first excited Kramers' doublet, $|1;\pm\rangle$, suggests that this is not the most likely process to occur. Indeed, from the first excited state both Orbach and thermally assisted QT processes are more probable: the former provides access to the second excited state while the latter would allow a reversal of the magnetization. On the basis of the above considerations a relaxation via the second excited state ($E_2 = 237\,\mathrm{cm}^{-1}$) seems to be more likely, in fairly good agreement with the phenomenological value of the above reported value of the energy barrier of $230\,\mathrm{cm}^{-1}$.

The use of transition moments to evaluate the potential relaxation paths is still providing only semi-quantitative indications,[66,140] despite being increasingly used in rationalizing the spin dynamics. A more directly quantitative reproduction of the observed dynamics, using the electronic structure derived by *ab initio* calculations, can be obtained by a master matrix based approach.[1] This approach assumes a series of steps of the direct process type promoted by a suitable spin phonon coupling Hamiltonian, assumed here of the Villain type[1] for the sake of simplicity. Indeed in the low symmetry of our system the dynamic spin phonon coupling Hamiltonian proposed in Abragam and Bleaney textbook[51] would require the calculation of a huge number of CF Hamiltonians following different distortions[69] and is thus unfeasible. On the other hand, notwithstanding its simplicity, our approach allows us to extract the relaxation time by calculating the relaxation rate γ_q^p from a state $|q\rangle$ (eigenstate of the

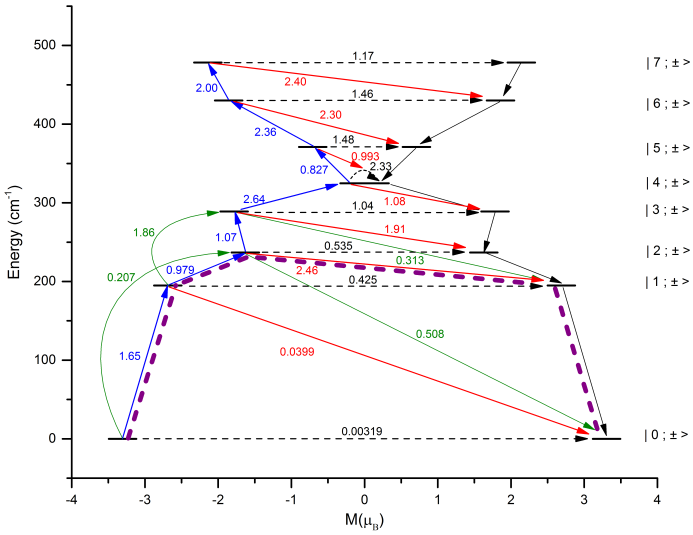

Figure 4.6: The *ab initio* computed magnetization blocking barrier for **1**. The thick black lines indicates the Kramers' doublets as a function of the projection of the magnetic moment on the chosen quantization axis (the one of ground multiplet). The red arrows show the possible pathways of the Orbach process. The dotted black arrows represent the presence of (thermal assisted) quantum tunneling between the connecting states. The numbers reported for each arrow are the mean absolute value for the corresponding matrix element of transition magnetic moment. The dotted purple lines show the most probable relaxation pathways for the reversal of magnetization.

Hamiltonian that describes the system) to another state $|p\rangle$:

$$\gamma_q^p = \frac{3v}{\pi\hbar^4 m c_s^5} \frac{(E_p - E_q)^3}{\exp\left[\beta(E_p - E_q)\right] - 1} \left\{ |\tilde{D}_a|^2 \left[|\langle p|\mathbf{J}_+^2|q\rangle|^2 + |\langle p|\mathbf{J}_-^2|q\rangle|^2 \right] + |\tilde{D}_b|^2 \left[|\langle p|\{\mathbf{J}_+, \mathbf{J}_z\}|q\rangle|^2 + |\langle p|\{\mathbf{J}_-, \mathbf{J}_z\}|q\rangle|^2 \right] \right\} \tag{4.2}$$

where β is $1/k_B T$, v and m are the volume and the mass of the unit cell, $\tilde{D}_a$ and $\tilde{D}_b$ are the spin-phonon coupling parameters. If the energy levels and the eigenstates are known, the only parameters that need to be adjusted are the spin-phonon coupling parameters and $v/(mc_s^5)$. In our case the CF eigenfunctions of the ground J multiplet and the corresponding eigenvalues in zero applied field obtained by the *ab initio* calculations were used to

obtain the Crystal Field matrix as $\mathbf{R}^T\mathbf{V}\mathbf{R}$ (where $\mathbf{R}$ is the eigenfunctions matrix and $\mathbf{V}$ the diagonal matrix of the corresponding eigenvalues). The complete Hamiltonian (Crystal field + Static magnetic field) was then obtained by adding the Zeeman interactions in the $|M_J\rangle$ basis. After diagonalization this provided new eigenvalues and eigenfunctions by which it was possible to calculate the master matrix $\mathbf{\Gamma}$ for all the investigated temperatures. Diagonalization of the master matrix allowed to extract the relaxation time as $\tau = -1/\lambda_1$, where λ_1 is the first non vanishing eigenvalue of the master matrix.

The result, obtained by adjusting both the spin-phonon coupling parameter to 0.05 and the pre-factor ($3v/\pi\hbar^4 m c_s^5$) to 3000, is shown in fig. 4.5b. It is evident that while this approach reproduces the linear high temperature region above 15 K, being consistent with an energy barrier of about 320 K, it overestimates the relaxation time at lower temperature. This is a common feature for many lanthanide based-molecular magnets and is usually attributed to the higher effectiveness of Raman process at lower temperatures. This process is however quite elusive since the corresponding parameters are usually considered as phenomenological.[46,121,125,135,136,141,142] Indeed, to the best of our knowledge, no reports are available relating the values of the Raman parameters (C and n) obtained by fit of dynamic data to the structure of the investigated molecule. This is a severe drawback in the search of increased relaxation times for potential applications, since this process, which provides a channel of relatively fast relaxation even at quite low temperature, is currently beyond our control. It is however to be stressed that, despite the phenomenological fit of the temperature dependence of the relaxation rate pointed to the existence of a T^n contribution, we cannot even be sure that this is associated to a real Raman process. Indeed, interactions which are not taken into account by the model, such as hyperfine and residual dipolar intermolecular interactions, may open the possibility of relaxation via quantum tunneling, and might also change the expected field and temperature dependence of direct processes.[143]

4.1.5 Summary

In conclusion, by means of the rational characterization of the $Dy(LH)_3$ mononuclear complex, an experimental and theoretical investigation of the anisotropy and dynamic behaviour of a novel mononuclear lanthanide-based single molecule magnet have been performed. We evidenced that the results of *ab initio* calculations can provide independent confirmation of detailed cantilever torque magnetometry in the absence of further spec-

troscopic information. This is particularly relevant in case the system is EPR silent and no detailed luminescence data are available. In turn this allows to analyze the observed dynamics of the magnetization on the basis of the calculated electronic structure of the lanthanide center. For the studied complex the experimental and theoretical results indicate a strong axiality of both the ground doublet and the first excited state; the *ab initio* prediction of an almost complete collinearity of the ground and first excited doublet is mirrored by the low temperature slow relaxation of the magnetization of the complex, which could be phenomenologically modelled by a combination of an Orbach and a Raman process. The observed behaviour could be qualitatively rationalized via the commonly used transition probabilities provided by the *ab initio* suite.[30,138] In addition to this we showed that the relaxation behaviour in the higher temperature range can be correctly reproduced assuming the *ab initio* computed electronic structure in a statistical analysis based on the master matrix approach. On the other hand, further processes are clearly contributing at low temperature, resulting in an experimental relaxation rate which is much faster than predicted by this approach. This might be due either to a true Raman process or to the unaccounted hyperfine and dipolar intermolecular interactions,the latter reduced but not completely quenched by the doping level used here. As a whole these results outline the necessity of a virtuous interplay between detailed single crystal studies and *ab initio* calculations. This process allowed us to obtain a detailed understanding of the relation between the electronic structure and the rich low temperature magnetization dynamics in this system, a point of crucial importance for rationally improving the properties of lanthanide-based single molecule magnets.

Author contribution

Matteo Briganti performed the *ab initio* calculations. Mauro Perfetti performed the Cantilever Torque Magnetometry measurement. Eva Lucaccini performed and fitted the EPR, AC and DC measurements. Matteo Briganti and Eva Lucaccini simulated the DC data and the relaxation mechanism by master matrix approach. Jean Pierre Costes synthesized the complex.

4.2 An archetypal and pedagogical system: the $\{Dy(DOTA)(H_2O)\}^-$ molecule

4.2.1 Introduction

Lanthanide ions when complexed by polyamino-polycarboxylate chelators form a class of compounds of paramount importance in several research and technological areas, particularly in the fields of magnetic resonance and molecular magnetism. One of the paradigmatic ligand of this class of complexes is the twelve-membered tetra-azamacrocyclic H_4DOTA (1,4,7,10-tetraazacyclododecane-1,4,7,10-N,N',N",N"'-tetraacetic acid). In its fully deprotonated derivative $DOTA^{4-}$ it forms thermodinamically and cinetically stable compounds[144] with the whole series of tripositive lanthanide ions Ln^{3+} in a capped square antiprismatic environment (coordination number 9). The rare earth atom is sandwiched between two parallel square faces, one formed by the ligand's four nitrogen atoms and the other by four oxygens of the four acetate groups. The 9th coordination site along the pseudo C_4 axis is occupied by a water molecule: the unique properties of this series of complexes arise from the interaction of the chelated lanthanide ion with this apparently innocent bonded molecule.

Indeed, this is the reason why the Gadolinium derivative is one of the most employed contrast agents for magnetic resonance imaging (commercialized as DOTAREM), alongside with other complexes such as $\{Gd(DTPA)(H_2O)\}^{2-}$,[145] the first approved in 1988 from the American Food and Drug Administration. Moreover ligands derived from DOTA such as DTMA[146,147] or DO3A[148] are widely employed and investigated in order to improve selectivity and contrast enhancement. The exchange of the apical water molecule between the complex and the solvent selectively increases the longitudinal relaxation rate of the water protons in certain tissues,[149] principle on which T_1-weghted magnetic resonance imaging (MRI) is based. The signal enhancement can vary in function of the concentrations of the contrast agent as well as of the different relaxivity in the different biological environments. On the other side complexes of the series based on anisotropic lanthanides, like Dysprosium, presents much shorter correlation times and showed to increase the transverse relaxation rate of protons, becoming promising contrast agents for T_2-weighted MRI,[150] a new generation of MRI contrast agents. Moreover, the hyperfine shift that some of these ions can induce in the surrounding molecules is exploited for new MRI contrast mechanisms such as the chemical exchange saturation transfer (CEST).[151]

The access to the magnetic anisotropy tensor is also an important

information to interpret solution and solid-state NMR of paramagnetic proteins. LnDOTA complexes already displayed good qualities in order to assess the structure of proteins by NMR spectroscopy.[152] Since the pseudo-contact shift depends on the position of the atom respect to the orientation of the magnetic susceptibility tensor and the distance from the paramagnetic center and its effect is felt on the surrounding local environment up to 40 $\AA$. Ln(III) complexes are, therefore, exploited as structural restraints to solve protein's structures.[153–155] In such a framework Tb, Dy, Yb and Tm are the most common paramagnetic[152] labels due to the ion's high anisotropy and small participation to the bonding, i.e. small contact shift.

In the field of molecular magnetism the series of $\{Ln(DOTA)(H_2O)\}^-$ was extensively studied[156,157] as one of the pioneer complexes of the lanthanide based Single Molecule Magnets (SMMs).[27] An archetype compound suitable for the investigation of the interplay of the electrostatic and orbital contribution is the $\{Dy(DOTA)(H_2O)\}^-$ complex.[61] This complex is a Single Ion Magnet (SIM) which has been deeply characterized both at the computational and experimental level. In particular, it was shown for the first time from a computational point of view the dependence of the orientation of the main magnetic axis in function of a finest structural modification: the rotation of the apical water molecule directly bonded to the Dysprosium atom. Indeed, to reproduce the experimental data (direction and magnitude of the anisotropy axes, and energy ladder) a particular orientation of the water's proton was necessary: for such a reason it was supposed an interplay between the electrostatic potential determined by the ligands and a small, but crucial, interaction between the Dysprosium's $4f$-orbitals and the water's molecular orbitals.

This uncommon behavior made the computational study of this complex a hard but intriguing task. It offers an extraordinary possibility to get insights about how to handle from a computational point of view the subtle equilibrium between orbital interactions and electrostatic field strength. The importance of a reliable reproduction of the crystal environment was already pointed out in lanthanide crystals of high polar simple condensate structure,[158] the series of elpasolites $Cs_2NaLnCl_6$, where a rationalization of the properties in terms of ligand field was also proposed.[158] Indeed the electrostatic potential inside a crystal is intrinsecally periodic, but *post*-Hartree Fock calculations are feasible only with packages of softwares based on Gaussians based wavefuctions, reducing the periodic treatment to molecular clusters of small dimensions: in order to simulate the periodicity of the environment the inclusion of the molecular

cluster in a Madelung potential becomes the key aspect. Different structural modelizations proposed in literature led to apparently conflicting results: in the original article by Cucinotta[61] both the orientation of the water's proton and the extension of the atomic cluster showed a prominent role in determining the energy ladders and the directions of the anisotropy axes; on the other side Chilton *et al.*,[63] reported no influence on the single ion magnetic anisotropy coming from the apical water's orientation.The difference in the obtained results is to be looked for in the difference in the models employed in the two articles, in particular the inclusion of different coordination spheres surrounding the central $\{Dy(DOTA)(H_2O)\}^-$ cluster, which can strongly affect the electrostatic field's strength. The aim of this work is to critically revise the models proposed in literature so far to get a reliable general approach of modeling complex magnetic lanthanide-based complexes as $\{Dy(DOTA)(H_2O)\}^-$ and to shed some light on the perennial question about the interplay between orbital and electrostatic contributions in such kind of complexes. This last aspect will be investigated by a large variety of magneto-structural correlations involving different structural bonding parameters (mainly rotations, but also stretching and bending) of the water molecule. These studies were applied to a different molecular cluster, each one representing different structural approximations. Along this way the new models and a critical review of the previous ones will be presented and discussed. The work is focused on a single lanthanide derivative, but the conclusions and the proposed approach can be extended in general, to other lanthanide based complexes and even beyond the solid state: from MRI's relaxation mechanism in solution to protein's structural refinement by NMR data.[154] Indeed even if in the crystals the rotation of the water molecule is not allowed by supramolecular interactions with neighboring molecules, in solution this is not true: the water molecule is free to rotate and exchange with the solvent. This could shed a new light on the mechanism of the relaxation enhancement in solution in presence of MRI contrast agents based on anisotropic lanthanide atoms.

4.2.2 Computational Details

Description of the Models

In this section the different models used in the paper are defined in details to make the reader fully aware of the different account of the environment by geometrical and electrostatic point of view.

Model 1 In order to reduce at the minimum the number of bias inherent the choice of the model, we have considered a Dy(DOTA)(H_2O) complex surrounded by four crystallographically symmetry related replicas along with the five Na^+ cations and the twenty-five co-crystallized water molecules (see Figure 4.8) representing two unit cells and half. Such a choice was driven by the fact that the Dy(DOTA)(H_2O) complexes form chains quite distant one from the other and only water molecules and Na^+ ions are present in between them. The whole model is formed by 414 atoms. However, such a model cannot be handled at the high level of theory as CASSCF/CASSI-SO approaches and, therefore, we chose to treat only one Dy(DOTA)(H_2O) unit (56 atoms) explicitly and at the highest level while all the other atoms were considered as point charges (see Computational section for more details). The net total charge is almost neutral (Q1 = 0.11).

In this framework, the closest groups the two H_w can interact with are represented by two carboxyl groups belonging to adjacent DOTA molecules present in the cell. The distance between the closest Oxygen atoms of the two carbonyl groups and the O_w are 2.773 and 2.803 *Å*. Similar distances are also observed for the four oxygens of the DOTA ligand directly coordinating the Dysprosium ion (see Figure 4.7). The two H_w are located in a network of an almost equidistant Oxygens atoms theoretically eligible for hydrogen bonding. However, only the two Oxygen atoms belonging to the adjacent DOTA ligands can be able to orient the O_w-H_w bonds at very low temperature.

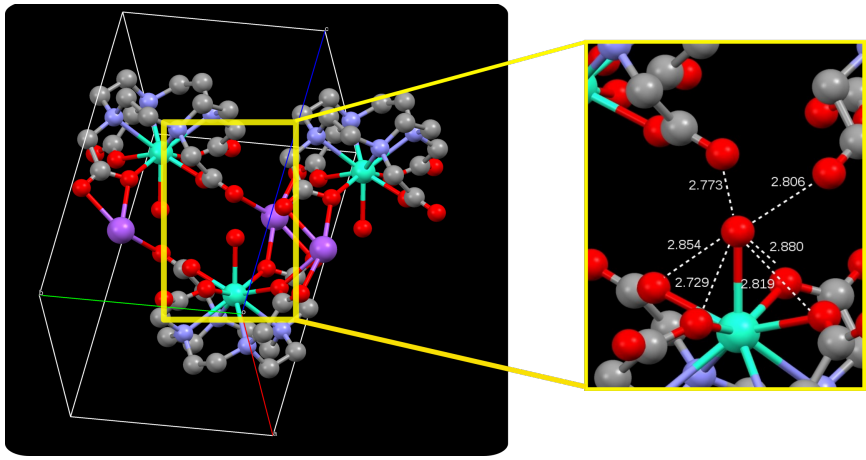

Figure 4.7: Positions of the nearest carboxyl groups in the crystal cell of Dy(dota) in *Å*.

For this reason, we have relaxed the H_w positions at the DFT level (see Computational details). The dihedral angle ϕ, defined by the plane determined by the water molecule and pseudo C_4 passing through the Dysprosium ion was optimized to 54°. Such a value strongly deviates from what previously reported by Cucinotta[61] (0°) where the two carboxyl groups where not considered in the optimization model, and by Blackburn[147] (22°), where the solution structure of $[Lu(DTMA)(H_2O)]^{3+}$ derivative was optimized in the gas phase. The two optimized O_w-H_w distances are 0.967 and 0.969 $\AA$. Such a geometry corresponds to $\alpha = 0°$, where α is the angle corresponding to the rigid rotation of the two optimized H_w atoms along the Dy-O_w. The angle α can, therefore, assume values from 0° (optimized H_w positions) to 2π values. We have also introduced the angle γ_n as a deviation index between the computed and experimental easy axis of magnetization, where n can assume values 0 and 1 for the ground and first excited doublets, respectively.

Model 2 and 2m With the aim to reduce the computational efforts but to have the same accuracy of M1, we reduced it to a model consisting of only one Dy(DOTA)(H_2O) unit. Such a model represents the most intuitive, and therefore, the simplest possible model. The net total charge of the model, **Q2**, is -1. In order to mimic the intermolecular interactions in the crystal, the two carboxylates groups belonging to the two Dy(DOTA)(H_2O) neighbor units that interact with the two H_w's were modeled with two molecules of formaldehydes, as shown in figure 4.9 (Model 2, **M2**). The net total charge of the model is therefore maintained (Q2 = -1). The coordinates of two Hw atoms where left to relax and, in support of the goodness of the model proposed, no changes were computed for the O_w-H_w distances and ϕ angle.

In virtue of the simplicity of the model such a model has been used to performed the majority of the magnetic-structure calculations. Indeed, calculations for ϕ values of 0° and 90° where also computed for $\alpha = [0°, 90°]$. It is worth to be mentioned that, the case for $\phi = 0°$ corresponds to the Model C used in the paper by Cucinotta[61] and it has been then used as cross reference, too.

A simpler model (Model C in Cucinotta *et al.*[61]) where only the Dy(DOTA)H_2O complex is also considered (i.e. no aldehydes added) is Model 2 'modified' (**M2m**). Such a model allowed to verify the role of the aldehydes.

In order to show the extreme difficulty to choose a structural model in which the experimental balance between electrostatic and orbital con-

tributions can be reliably modeled we have built up three more models resembling the ones already used in literature.

Model 3 In the unit cell, each Dy(DOTA) complex is surrounded by three counter-ions. Indeed, three of the four carboxylates involved in the coordination of the Dysprosium ion contribute to the coordination of three Na^+ ions, too. The Model 3 (**M3**, see figure 4.10) has been designed to account these three cations, positioned in their crystallographic positions. Moreover, to reduce the charge of system, the two aldehydes groups were substituted with two formate anions. The formates are in the same positions of the two carboxilate groups of the two next DOTA molecules in the crystal packing. This model is neutral (**Q3** = 0) and it is composed by 67 atoms. The two H_w atoms were positioned accordingly to **M1**. All the atoms are considered explicitly. Such a model corresponds to Chilton's[63] model with the only difference related to the inclusion of the formates. For computational details see computational methods.

Model 4 Model 4 is obtained adding to **M3** four more formate anions and the two water molecules around the three Na^+ ions (see figure 4.11). The added four formate groups mimic the carboxylate groups that belong to the DOTA ligands of the four neighbor DyDOTA complexes. The first coordination sphere of each Na^+ ion is now complete being coordinated by six Oxygen atoms, at difference as in **M3**. However, the net total charge of the complex is -4 (**Q5** = -4). The number of atoms in the model increased up to 92. The two H_w atoms were positioned accordingly to **M1**. All the atoms are considered explicitly. For computational details see computational methods.

Model 5 Each DyDOTA complex has got other four symmetry related Dy(DOTA) complexes as first neighbors. To reduce the charge unbalance in **M4**, the computed DFT point charges of the four Dysprosium ions belonging to the surrounding complexes were added (see figure 4.12) to it (**M5**). The charge of the peripheral lanthanide ions was set to 1.37 and the net total charge, **Q5**, became 1.48. The two H_w atoms were positioned accordingly to **M1**. All the atoms are considered explicitly but the four neighbor Dy(III) ions. For computational details see computational methods. Such a model is very close to the Model A/A' (neutral charge) proposed by Cucinotta *et al.* where acetates where used instead of out formiates and four excplicit Na^+ ions were used at the place of Dy^{3+} ions.

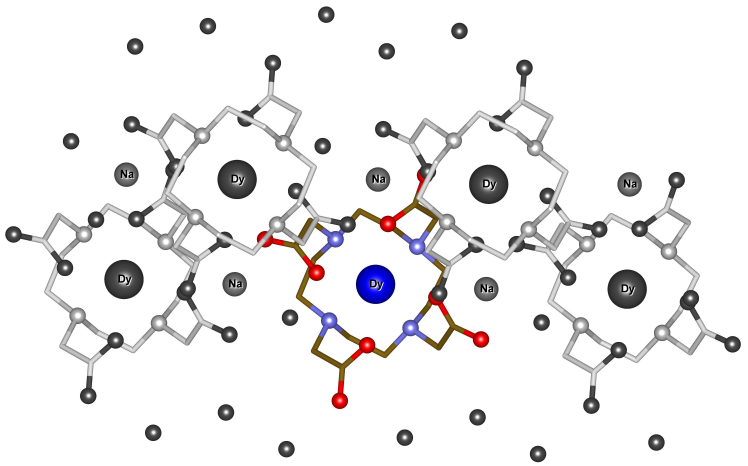

Figure 4.8: Model **1**. The atoms in grey are substitued by their atomic point charges. Hydrogens atoms are hidden for sake of clarity.

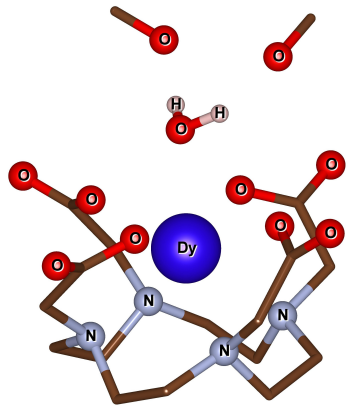

Figure 4.9: Model **2-2m**. Only the hydrogens of the water molecule are displayed.

Computational Method

Geometry optimization of the only two H_w atomic positions in **M1** and **M2** was performed with the quantum chemistry package ORCA.[159] Unrestricted DFT/B3LYP[160] together with Van der Waals empirical dispersion correction D3[161] have been used. VTZPP basis sets for all the atoms were chosen. Relativistic effects were taken into account by using the second-order Douglas-Kroll-Hess (DKH2) Hamiltonian. The spin multiplicity was

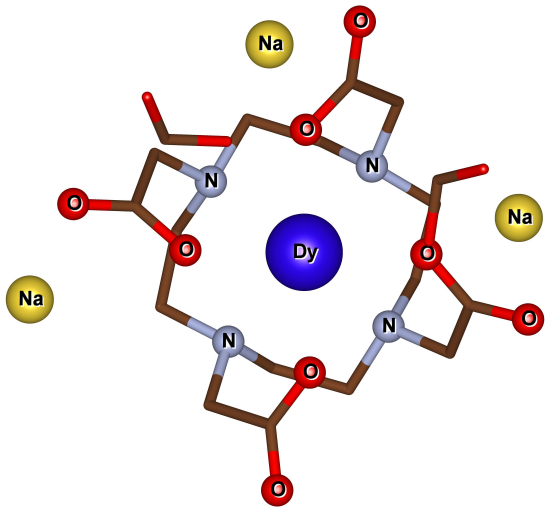

Figure 4.10: Model **3**. Hydrogens atoms and the apical water molecule are hidden for sake of clarity.

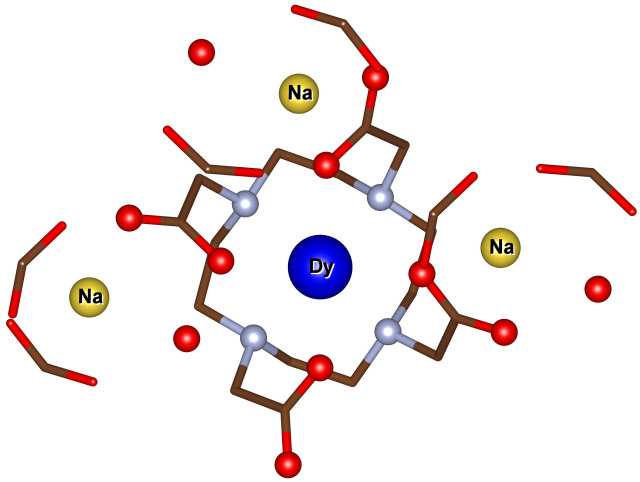

Figure 4.11: Model **4**. Hydrogens atoms and the apical water molecule are hidden for sake of clarity.

set to six. Def2-TZVPP basis set were employed for all the atoms except for the lanthanide atom where SARC-TZV basis[162] were used.

In order to simulate the effect of the crystal environment at a larger extent than considering just few neighbor atoms or pieces of adjacent

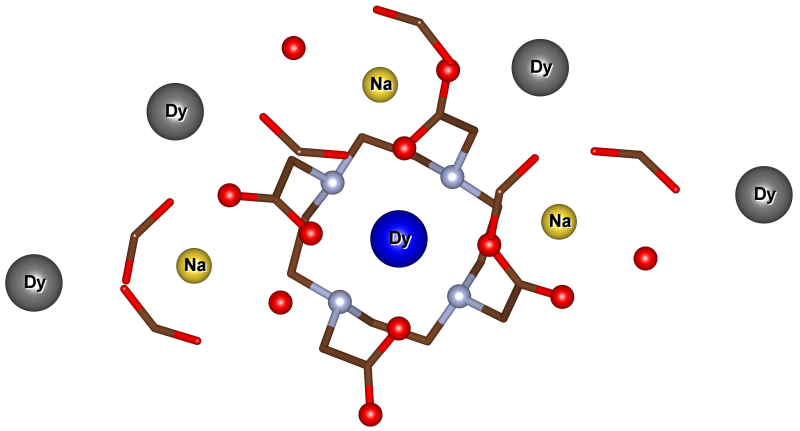

Figure 4.12: Model **5**. The lanthanides in grey are substutued by their atomic point charges. Hydrogens atoms are hidden for sake of clarity.

Dy(DOTA) complexes but still at an affordable level, atomic point charges were added to the explicit models. Point charges were computed as density derived atomic point charges (DDAPC)[163] obtained by a single point calculation on the [NaDy(DOTA)(H2O)] · 4H2O unit cell with PBE0[164] functional and periodic boundary conditions included. Van der Waals empirical dispersion corrections RVV10[165] have been used. The package of software CP2K 2.6[95] based on a mixed gaussians and plane waves (GPW) formalism was employed. Since, basis sets for Dysprosium are not available in the package, the Dysprosium atom was substitued by the La(III) ion. Double-z polarized basis sets (mid-PBE for La, DZVP-MOLOPT-SR47 for other atoms) with Goedecker–Teter–Hutter norm conserving pseudopotentials[166] have been employed. The PW cutoff have been set to 400 Ry.

The computational protocol used for all the models to compute the excited states and the magnetic anisotropy is the following. All the calculations were performed with the package of programs MOLCAS 8.0.[101] The multiplicity of spin for this first step was set as the maximum possible: a sextuplet for Dy(III). The active space consisted of nine electrons in the seven $4f$ orbitals of the Lanthanide ion[61,96,167][CASSCF(9,7)]. The f orbitals were chosen through the program Molcas Grid Viewer (MolcasGV). State averaged calculations for the possible multiplicities were then performed in order to have the maximum number of spin-free states of the given multiplicity. At the first stage, all the procedure was performed with the minimal basis set (ANO-RCC-MB) to obtain a better orbital guess. Once obtained, the dimension of the basis was increased and all electron

ANO-RCC[102,168,169] basis sets were employed in all the calculations (see table 4.5 for details and contraction schemes).

Atom	Label	Primitives	Contraction
Dy	VTZP	[25s22p15d11f4g2h]	[8s7p5d3f2g1h]
Na	VDZ	[17s12p5d4f2g]	[4s3p]
N	VTZP	[14s9p4d3f2g]	[4s3p2d1f]
O	VTZP	[14s9p4d3f2g]	[4s3p2d1f]
C	VDZP	[14s9p4d3f2g]	[3s2p1d]
H	VDZ	[8s4p3d1f]	[2s]

Table 4.5: Contractions of the ANO-RCC basis set used for all CASSCF calculations.

The orbitals projected on the larger basis set were then used as starting orbitals for subsequent CASSCF calculations. Average state calculations were performed only considering all the sextets (21 roots). Complete Active Space State Interaction (CASSI) was calculated, using the previously computed CASSCF states in order to check the effect of the spin-orbit splitting on the ground ${}^6H_{\frac{15}{2}}$ ground state. Only the sextets (${}^6H$, ${}^6F$, and ${}^6P$ sextets) were taken into consideration since the inclusion of other multiplets did not improve the solution.[45,61] Moreover, we chose not to include a second order perturbation on the CAS (CASPT2) since the effect on the first two excited doublets was of the order of only few wavenumbers.[61] The main magnetic axes for the first eight Kramers' doublets were computed with the SINGLE-ANISO module with pseudospin $\tilde{S} = 1/2$.

The atomic electric multipole moments were computed with the LOPROP module[170] on the ground state electronic density obatined with the CASSCF/CASSI-SO method.

Rigid rotation of the two optimized H_w atoms along the Dy-O_w axis defines an angle which assumes a value of 0° for the optimized H_w positions and it can vary from 0 to 2π values. For **M1**,**M2**, and **M2m** a was varied along the whole [0, 2π] range. For **M3**,**M4**, and **M5** calculations were performed only for $\alpha = 0°, 90°$.

4.2.3 Results and Discussion

In order to shed some light on the effect of the model tailoring on the electrostatic environment of the Dysprosium ion and consequently on the orientation of the easy magnetization depending on the rotation of the

apical water molecule, we chose to used different models some recalling the ones already used in literature along with new ones. The differences among the presented models rely on the number of explicit atoms considered at the highest computational level and the eventual addition of a different number of point charges. For all of them the same computational protocol CASSCF/RASSI-SO along with all-electron basis sets for all the explicit atoms considered were used (see Computational Methods). Rigid rotations of the apical water molecule were performed on all the presented models.

Model1

The necessity to fulfill at the same time both chemical soundness and a accurate representation of the electrostatic environment around the very sensitive Dy(III) ion is frustrated by the absence of any experimental data supporting other than the experimental value i.e. $\alpha = 0°$. The most correct way to model a system as Dy(DOTA) would be considering it in its periodic environment. The problem of this approach is related to the impossibility to perform such a calculation at the level of accuracy affordable by the CASSCF/RASSI-SO approach. One possible solution is represented by the mimicking of the first neighbors Dy(DOTA)(H_2O) complexes and of the crystallization water molecules through point charges leaving a single Dy(DOTA)(H_2O) computed explicitly at the high level of accuracy. In order to shed some light on the real dependence of the easy axis orientation on the water molecule rotation, we have chosen **M5** as our reference model (see Computational Details). Indeed, it is worth to remind that the only geometrical approximations were limited to the choice of the number of neighbor Dy(DOTA)(H_2O) units (4) in addition to the one considered explicitly and the number of water molecules and Na^++ ions present in two and a half unit cells. DDAPC charges were, therefore, computed for a total net charge of the model of 0.11 (see computational details).

We have monitored the evolution of the electronic structure of **M1** for twenty values of α. The principal g-values of the ground and first excited Kramer' doublets and the angle between the computed g_z components and the experimental value are reported in Table 4.6. The computed g-values for $\alpha = 0°$ show a stronger Ising character of the Dy(III) ion than the experiment but in agreement with the previously computed g-values.[61] The good accuracy of the results is also witnessed by the very good agreement observed between the experimental and the computed easy axis of magnetization value. The deviation of 3° is well below the experimental uncertainty. The ground and the first excited doublets show a promi-

nent contribution from the $|M_j >= 15/2$ and $|M_j >= 13/2$ components and they are separated by 47 cm^{-1} in excellent agreement with an experimental value of 52 cm^{-1}. A very good agreement is evidenced also for higher energy doublets which differ from the experimental ones of 16 cm^{-1} at maximum. Only for E_2 and E_5, a more significant deviance from the experimental value was found (28 and 31 cm^{-1}), respectively. Interestingly, the first excited doublet shows also a significant Ising character and the orientation of its g_z component is quasi-orthogonal (80.1°) to the one of the ground doublet. The whole agreement with the experiment is evident. This is not surprising since the present computational model represents the best representation so far of the environment that the single Dy(DOTA)(H_2O) unit can experience. In other words, such a model, at the geometrical level, is, in principle, not prone to more or less arbitrary and chemically meaningful approximations as reported in previous literature. In the light of these results, we have performed the same calculations with different values of the angle α. First of all, we have tried to calculate the evolution of the orientation of the easy axis of magnetization for 0° $< \alpha <$ 90° as already reported (see Table 4.6) and then extended for 90° $< \alpha <$ 360°. The choice to extend the α range is due to the asymmetry introduced by the presence of the two carboxylate groups coordinating the H_w atoms in the explicit Dy(DOTA)(H_2O) unit. For more clarity the g_z orientations in function of the α angle are collected for both the ground and the first excited doublet in Figure 4.13. Regarding the ground state (blue curve), it is evident that the rotation of the apical water modules the orientation of the easy axis of magnetization in the plane identified by the DOTA oxygens atoms coordinating the Dy^{3+} ion. The value of γ_0 remains almost constant up to 60° and only after it starts to increase up to a maximum computed for α= 120°. Therefore the easy axis orientation is a smooth process since a range of 60° was necessary to α to cover the gap between the minimum and maximum values of γ_0. Moreover, the easy magnetization axis took about 60° (180°) to recover a value of γ_0 close to 0°. A similar trend is observed also for 180° $< \alpha <$ 360°, even if a slight higher maximum was achieved (γ_0 =78.5°) maintaining practically unaltered the range of α values for which the variation of γ_0 took place.

	Exp	*Opt*	59°	75°	90°	105°	120°	129°	140°	150°	180°	200°	220°	245°	260°	270°	290°	300°	310°	320°	330°	340°
Principal g-values of the ground Kramers doublet																						
g_x	3.4	0.3	0.3	0.7	1.0	0.9	0.9	0.9	1.1	0.9	0.3	0.2	0.2	0.6	1.1	1.0	0.8	0.9	1.0	1.1	0.9	0.6
g_y	4.9	0.7	0.9	2.6	6.1	4.5	4.1	5.1	7.1	4.5	0.7	0.5	0.6	2.4	7.3	6.1	3.5	4.2	6.0	8.3	4.8	2.2
g_z	17.0	19.2	19.0	17.3	13.9	15.5	16.0	15.0	13.1	15.7	19.2	19.4	19.3	17.8	13.2	14.3	16.8	16.2	14.5	12.3	15.5	18.0
γ_0 Angle between experimental and calculated g_z of the ground Kramers doublet																						
		2.8°	1.3°	5.5°	34.1°	67.7°	71.7°	67.8°	34.9°	7.3°	3.5°	3.4°	2.7°	2.2°	25.6°	68.3°	78.5°	77.7°	73.0°	41.5°		1.7°
Principal g-values of the second Kramers doublet																						
g_x		0.43	0.2	0.2	1.8	1.7	1.6	1.7	1.9	1.7	0.4	0.7	0.5	1.0	1.9	1.8	1.6	1.7	1.8	1.9	1.6	0.8
g_y		1.12	1.2	1.2	4.5	3.0	2.6	3.5	5.5	3.1	1.1	1.1	1.1	1.5	5.7	4.4	2.1	2.6	4.3	6.7	3.4	1.5
g_z		17.95	17.6	17.6	11.9	13.8	14.4	13.3	11.1	13.9	18.0	18.1	18.0	16.2	11.2	12.6	15.3	14.7	12.8	10.3	13.8	16.5
γ_1 Angle between experimental and calculated g_z																						
		80.1°	77.5°	73.5°	44.0°	9.2°	5.5°	9.0°	42.9°	72.0°	79.5°	78.7°	78.5°	77.1°	53.5°	9.2°	1.0°	0.9°	4.8°	36.3°		80.0°
Energy Levels (cm^{-1})																						
E_0	0	0	0	0	0	0	0	0	0	0	0	0	0	0	0	0	0	0	0	0	0	0
E_1	52	47	40	25	18	19	20	18	16	18	41	49	44	25	17	18	23	22	19	18	21	28
E_2	112	140	136	128	123	123	122	121	121	122	133	137	135	126	123	124	126	126	125	125	127	131
E_3	198	212	208	198	193	194	194	192	191	192	206	212	209	198	194	195	198	198	197	196	197	201
E_4	287	298	295	286	281	281	281	280	279	280	292	297	295	285	281	282	285	284	283	282	284	288
E_5	400	369	365	357	352	352	351	349	348	349	362	367	366	356	353	354	357	357	356	354	356	359
E_6	454	451	446	437	432	431	430	429	428	428	442	449	449	441	439	440	442	442	440	438	439	442
E_7	574	590	583	574	568	567	566	565	564	565	579	585	585	578	577	578	582	582	580	578	578	581

Table 4.6: Results of the calculations on DyDOTA system for **Model 1**

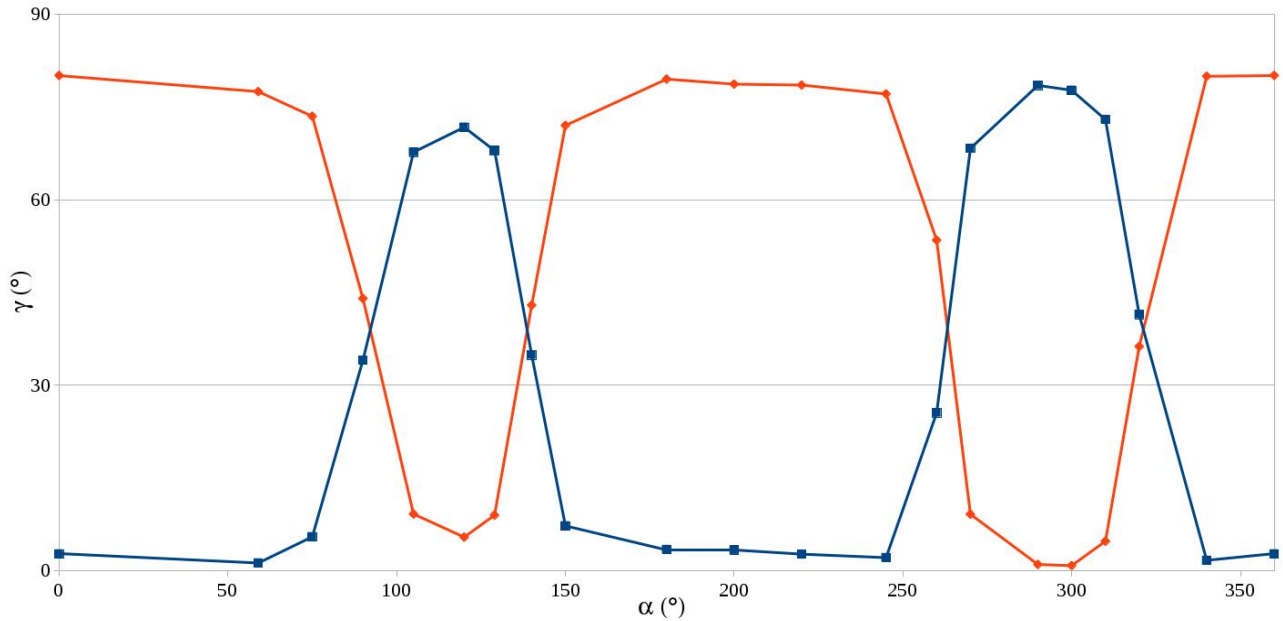

Figure 4.13: Angle between the calculated and the experimental main magnetic axis in function of the rotation of the water molecule for **M1**, for ground and first excited Kramers' doublet

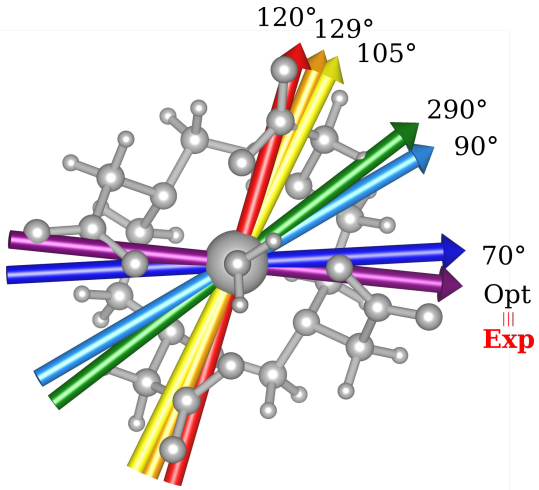

Figure 4.14: Orientation of the computed main magnetic axis inside the molecular frame for **M1**. The black number indicates the angle of rotation of the water molecule α related to that computed easy-axis.

Such results are important for two main reasons: first, they show that a strong reorientation of the easy axis of magnetization can be induced by the simple rotation of the apical water even if at larger values than $\alpha = 90°$, in contradiction to what reported by Chilton;[63] Secondly, the reorientation is a smooth phenomenon and not an abrupt one as reported in Cucinotta *et al.*,[61] where the change in the orientation was observed within 15°: γ_0 passing from - 1° to 92° from $\alpha = 45°$ to $\alpha = 60°$, respectively.

It is also worth to stress that similar results, but opposite in trend, were obtained for the first excited doublet. Indeed, the two $\gamma_{0,1}$ values observed for the ground and the first doublet states, respectivley is found to be constant (80°± 3 °) for all the 2π range.

In order to deepen this interesting behaviour, we have analyzed the compositions of the ground and first excited Kramers'doublets in terms of $|M_j>$ multiplets (see Computational Details) for α equal 0° and 120°, as shown in table 4.7. The ground Kramers'doublet for $\alpha = 0°$ displays a prominent contribution from the $|Mj>= |\pm 15/2>$ (95%), instead the first excited from $|Mj>= |\pm 5/2>, |\pm 3/2>, |\pm 1/2>$ (15%, 24%, 36%, respectively). Instead, after the water molecule rotation of 120° the contributions are inverted: the ground state shows a prominent contribution from the same $|M_j>$ multiplets which were predominant in the first excited at $\alpha = 0°$ ($|\pm 5/2>, |\pm 3/2>, |\pm 1/2>$ with contributions 11%, 22%, 29%, respectively), while the first excited one presents an almost unique

composition from the $|Mj>=|\pm 15/2>$ (71%). The correspondance is not perfect: for $\alpha = 120°$ the ground doublet shows a contribution from $|Mj>=|\pm 15/2>$ (24%), not present in the first excited for $\alpha = 0°$, and similarly the first excited a contribution from $|\pm 1/2>$ (12%).

Therefore, we can think that E_0 goes towards a swapping process with E_1 depending on the rotation angle of the water molecule. From an accurate analysis of the energy ladders calculated for different α values, such a flipping process can be rationalized in three main steps. In the first step, where α ranges between 0° and 70°, we have indications that the rotation of the water molecules induces a destabilization of E_0 of about 20-25 cm^{-1} leaving the energy ladder practically unchanged for E_2-E_7 (each of them is stabilized of 20±3 cm^{-1}). Instead, the energy of the first excited doublet, E_1, remains practically constant. In this a range, both E_0 and E_1 keep their easy axis original orientation ($\gamma_0 = 2.8°\div 5.5°$, $\gamma_1 = 80.1°\div 73.5°$). In the second step, that is $70°<\alpha<90°$, we observed a kind of avoided crossing scenario between E_0 and E_1 states witnessed by the fact that at 90° we have an intermediate easy axis orientation ($\gamma_0 = 34.1°$, $\gamma_1 = 44.0°$). Supposing the E_0 and E_1 related energy surfaces undergo to an avoided crossing situation, we can qualitatively estimate the E_{cross} 20 ± 2 cm^{-1} by ($E_0(\alpha = 75°,129°,245°,310°)+E_1(\alpha=105°, 150°,270° 330°)/2$, where the two α values immediately before and after the avoided crossing point are considered. To this step, we can, therefore, associate an energy of 20 cm^{-1} to the E_0/E_1 states swap. In the third step, where values range values are between 90° to 120°, are involved the energies needed by the flipped states to be localized again ($\gamma_0 = 67.7°\div 71.7°$, $\gamma_1 = 9.2°\div 5.5°$) with their easy axis of magnetization quasi-orthogonal again. In this regard, it is not surprising that an equal value of the one found for $0°<\alpha<70°$ for E_rot is found.

From the considerations above, we can say that the energy involved to reach the avoided crossing point (E_{rot} + E_{cross}) is about 40-50 cm^{-1}. The energy, instead, necessary to spend to completely rotate the easy magnetization axis ($2E_{rot}$ + E_{cross}) can be, therefore, estimated to be in about 60-70 cm^{-1}. Such result suggests that in the case the separation energy between the first two doublets would exceed the requested flip energy quantum (40-45cm^{-1}), the reorientation of the easy axis of magnetization would not likely take place. Of course, the value of the flip energy quantum could be model dependent, but the ratio of the phenomenon is valid in general (vide infra). Unexpectedly, in the $90° < \alpha < 140°$ range, in correspondence of the flip of the easy axis of magnetization from γ_0 0° to 72° and back to 35°, the E_0-E_7 energies did not show any changes

α	0°	120°
$\|M_J>$	E_0	E_0
±15/2	**0.94565751705**	**0.241719936811**
±13/2	0.000277673593	0.02225987361
±11/2	0.003751082898	0.024106485156
±9/2	0.003274179106	0.025085438118
±7/2	0.023707287285	0.069871080585
±5/2	0.003285747289	**0.112098521353**
±3/2	0.012714124635	**0.217951316007**
±1/2	0.007333068565	**0.28690738982**
	E_1	E_1
±15/2	0.029218409139	**0.707749389024**
±13/2	0.065768263988	0.024262224446
±11/2	0.038279154867	0.011683952285
±9/2	0.048125530357	0.020706767765
±7/2	0.051603550055	0.010491140387
±5/2	**0.156077990002**	0.044490046437
±3/2	**0.244606566861**	0.062677717005
±1/2	**0.366321002497**	**0.11793934275**

Table 4.7: M_J composition of the first two kramers' doublet for **M1**

(1÷3 cm^{-1}). From $\alpha = 150°$ we observed a new swap between the first two doublets which led, for $\alpha = 200°$, to values of γ_0 and doublets ladder energies corresponding to $\alpha = 0°$ (see Table 4.13). From this value, the ground doublet energy started to be destabilized again by the further water molecule rotation until when, for $\alpha = 260°$, we computed a further flip of the easy axis of magnetization. In the range $270° < \alpha < 320°$, E_0-E_7 energies were computed very close to the corresponding energies found for the $90° < \alpha < 140°$ interval.

In this framework we can also give an explanation of the not perfect correspondance of the compositions in terms of $|M_j>$ multiplets presented in Table 4.7. The flip between the states is not total, even for $\alpha = 120°$. This is due to the fact that the rotation of the water molecule can apply a perturbation of almost 60-70 cm^{-1}, and it is not sufficient to totally localize the states again after the switching process. Indeed components of the states before the swapping process are found for the states at $\alpha = 120°$: a $|\pm 15/2>$ contribution of about 24% in the ground state and a $|\pm 1/2>$ contribution of about 12% in the first excited. For the same reason the calculations also displays a strong axiality for $\alpha = 0°$ ($g_z = 19$) but a less pronounced one for $\alpha = 120°$ ($g_z = 16$), as shown in table 4.6.

From the presented results, it becomes evident that the indirect inclusion of periodic contributions even if treated at the electrostatic level

	Exp	**M1**	**M2**
	Principal g-values of E_0		
g_x	3.4	0.6	0.7
g_y	4.9	2.9	3.1
g_z	17.0	17.3	17.2
	Angle γ_0		
		2.98°	77.5°
	Principal g-values of E_1		
g_x		1.3	1.4
g_y		1.6	1.7
g_z		15.7	15.9
	Angle γ_1		
		76.0°	4.2°
	Energy Levels (cm^{-1})		
E_1	0	0	0
E_2	52	27	25
E_3	112	146	144
E_4	198	231	230
E_5	287	356	356
E_6	400	506	508
E_7	454	702	704
E_8	574	982	981

Table 4.8: Results of the calculations on **M1** and **M2** without apical water molecule

brought out a magnetic and electronic structure richer of flavors than already observed for simpler model. On the basis of what discussed above, hint on the reason why in literature different models did not show any changes in the orientation of the easy axis of magnetization in function of the variation of α: all depends on deviation from the experimental E_0-E_1 gap. Indeed, since the rotation of the apical water involve an energy of about 60-65 cm^{-1} going from $\alpha = 0°$ to $\alpha = 120°$, in the case the gap is computed larger than 60-70 cm^{-1}, no flip of the easy axis will be likely observed (see Chilton's model[63]); in the case the gap is smaller, the ground doublet can be erroneously computed due to a poor geometrical modelization choice leading to a partial or total prevalence of a wrong orientation of the easy axis of magnetization over the experimental evidence. It becomes evident that the modelisation of lanthanides systems needs considerable care in order to avoid unwanted misinterpretation of the experimental findings.

In such framework we decided to verify how the magnetic properties of **M1** could be altered by the removal of the water molecule, as previously performed by Cucinotta *et al.*[61] The results are reported in table 4.8. Differently from what reported,[61] where the easy axis of magnetization showed a $\gamma_1 = 82.4°$ with respect to the experimental finding, we observed a γ_1 angle of only 3°. The energy ladder, instead, is found quite different from the one computed for the complete **M1** model and, therefore, from

the experimental findings, too.

In order to shed some light on the modelization effects on the magnetic properties we performed similar calculation on several other models.

Model 2

A completely different approach from **M1** is represented by the choice of **M2** (see figure 4.9). Indeed, it represents, along with **M2m** (vide infra), the simplest possible model and for this reason we have studied it in details. Even for this model, we have monitored the evolution of the electronic structure for eighteen values of α. Interestingly, the optimization of the two H_w lead to the same geometry found in **M1**. The results obtained for **M2** are reported in Table 4.9 where the principal g-values of the ground and first excited Kramer' doublets and the $\gamma_{0,1}$ angles are shown. The computed values give a similar picture given by **M1** with slightly, but significant, differences. First of all, the rotation effect on the flip of the easy axis is fully confirmed as its Ising type along all the α values, even if the rhombicity is more enhanced than in **M1** and, therefore, in even nicer agreement with the experiment. The deviation of 8° from the experimental orientation of the g_z values is below experimental uncertainty. The trend of the easy axis of magnetization flipping is similar to the one observed for **M1** with the difference that the periodicity observed for the two orientations are larger and smaller, respectively, than in **M1**. For such a reason, the flip is observed already for $\alpha = 59°$ instead of 70° and the maximum is reached at $\alpha = 90°$ instead of 120°.

Differently from **M1**, the ground and the first excited doublets in this case are separated by only 15 cm^{-1} versus an experimental value of 53 cm^{-1}. Regarding the E_2-E_7 values, an overall good agreement with the experimental energies was found for only E_2-E_4 while a worse agreement (about 40 cm^{-1} of difference) was found for E_5-E_7. For the reason above, it is difficult to say which state, between E_0 and E_1, is affected by the water rotation, but a rough estimate of the E_0 destabilization/E_1 stabilization (E_{rot} + E_{cross}) can be likely about 40 cm^{-1}, in good agreement with what found in **M1** model. Differently from **M1**, the maximum flip is now reached in the narrow α range: $0° < \alpha < 90°$. The strong asymmetry in the α intervals between **M1** and **M2** can, now, be readily explained: since the separation energy between E_0 and E_1 is only 15 cm^{-1} and the energy quantum involved during the first step of the water rotation (E_{rot}) is about 20 cm^{-1}, the flip can happen at lower α values (45°) than in **M1**. A further indication of the interdependence of the two lowest doublets, even for this model the two correspondent $\gamma_{0,1}$ values observed are quasi-

complementary as observed for **M1** for all α values, even if at a lesser extent (77° ± 13°).

The effect of the removal of the water molecule has been studied also for this model: in such a case the easy axis of magnetization showed a $\gamma_1 = 77.5°$ in agreement with Cucinotta *et al.*[61] The results are shown in table 4.8. The energy ladder is curiously equivalent to the one found for the correspondent model in **M1** with the difference that the two first doublets are flipped. Such a result further stresses the model dependence of the magnetic properties. On **M2** we have also verified the magneto-correlation effects of the angle ϕ on the magnetic properties when $\phi = 0°$, 54° and 90°. In this regards, the effect of the variation of ϕ on the first excited doublet does not exceed 8 cm^{-1}.

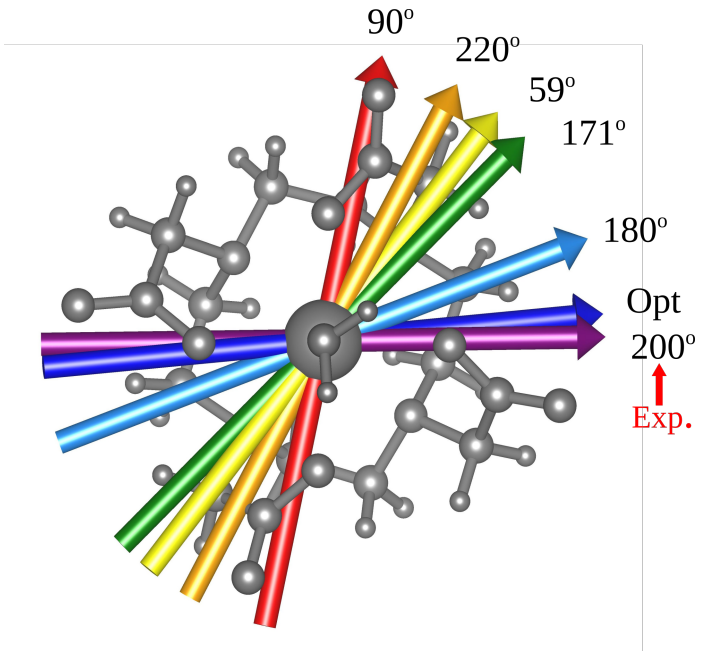

Figure 4.15: Orientation of the computed main magnetic axis inside the molecular frame for **M1**. The black number indicates the angle of rotation of the water molecule α related to that computed easy-axis.

	Exp	0°	30°	45°	52°	59°	90°	129°	171°	180°	200°	215°	225°	229°	270°	300°	340°	350°	355°
								Principal g-values of the ground Kramer doublet											
g_x	3.4	1.0	0.6	0.9	1.0	1.0	0.3	0.2	1.1	1.1	0.8	1.0	1.0	1.0	0.2	0.2	0.7	1.1	1.1
g_y	4.9	5.4	2.3	4.2	6.2	6.4	0.7	0.5	8.0	7.6	4.0	4.9	7.0	5.6	0.5	0.4	2.7	6.9	7.4
g_z	17.0	14.9	17.7	16.0	14.0	13.8	19.1	19.3	12.6	12.9	16.3	15.5	13.3	14.6	19.3	19.4	17.4	13.4	13.9
								γ_0 Angle between experimental and calculated g_z											
		8°	0°	8°	21	54°	81.1°	82.9°	47.8°	24.6°	7.3°		30.4°	65.3°	82.2°	83.3°	79.8°	63.2°	25.2°
								Principal g-values of the second Kramer doublet											
g_x		1.7	1.1	1.5	1.7	1.8	0.3	0.5	1.8	1.8	1.6	1.7	1.7	1.7	0.5	0.8	1.4	1.8	1.8
g_y		4.4	1.3	2.8	4.7	5.5	1.1	1.1	6.7	6.1	2.6	3.4	4.4	4.2	1.1	1.1	1.5	5.4	6.0
g_z		12.9	16.4	14.5	12.1	11.4	18.2	18.4	10.4	11.0	14.6	13.7	12.6	13.0	18.4	18.5	16.2	11.8	11.1
								γ_1 Angle between experimental and calculated g_z											
		56.1°	74.1°	64.2°	57.0°	12.8°	4.4°	6.7°	28.6°	54.6°	74.3°	70.2°	48.1°	12.2°	5.5°	5.8°	2.8°	13.7°	53.4°
	Exp	0°	30°	45°	52°	59°	90°	129°	171°	180°	200°	215°	225°	229°	270°	300°	340°	350°	355°
								Energy Levels (cm^{-1})											
E_1	0	0	0	0	0	0	0	0	0	0	0	0	0	0	0	0	0	0	0
E_2	52	15	22	18	16	16	39	46	15	15	18	17	15	16	45	52	21	14	14
E_3	112	118	122	121	120	120	129	131	120	120	121	120	118	119	131	134	120	117	117
E_4	198	185	192	191	190	190	201	205	190	190	191	190	188	188	205	211	189	175	185
E_5	287	272	280	279	279	279	289	291	278	278	280	278	276	277	292	296	276	272	272
E_6	400	338	346	347	347	348	359	359	346	347	349	348	346	346	363	367	343	338	337
E_7	454	412	421	424	424	425	435	434	424	426	429	427	426	422	444	447	418	412	411
E_8	574	530	543	548	550	551	561	559	554	556	558	555	552	548	570	575	540	532	530

Table 4.9: Results of the calculations on **Model 2**: g-values of ground and first excited Kramers'doublet, corresponding angle between experimental and calculated g_z and energy levels.

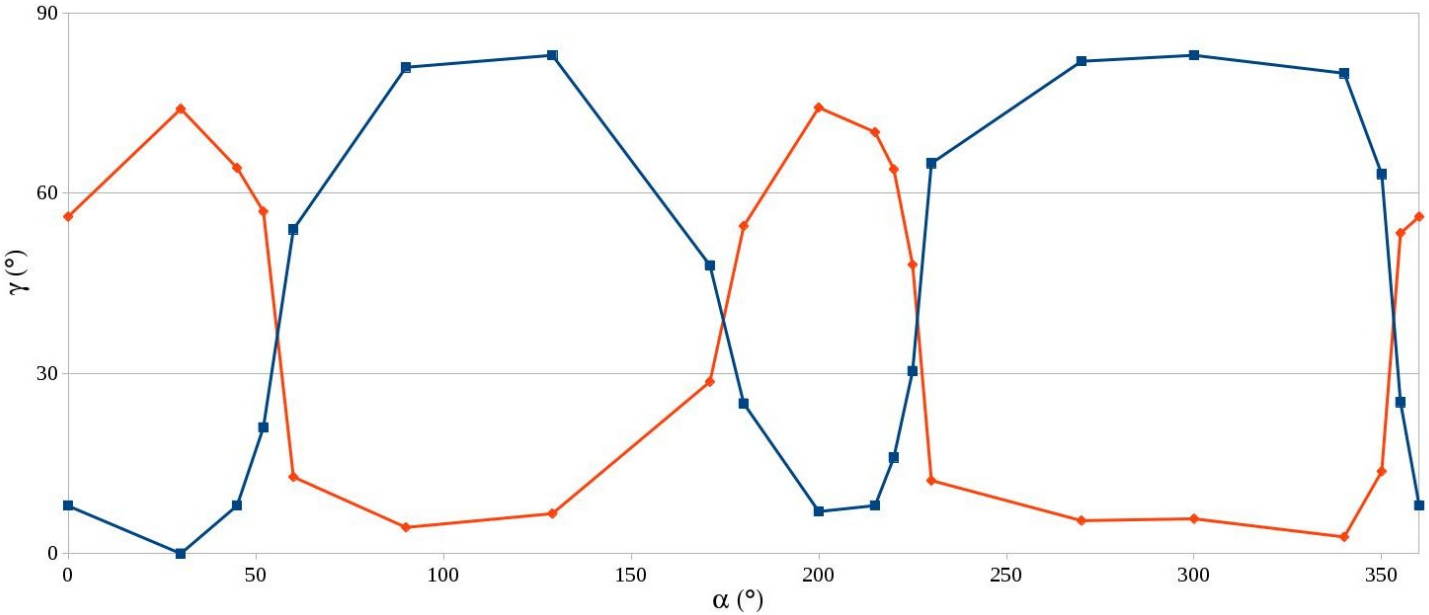

Figure 4.16: **Model2**. Angle between the calculated and the experimental main magnetic axis in function of the rotation of the water molecule, for ground and first excited Kramers' doublet

Model 2m

To verify the influence of the two aldehydes and to have a model directly comparable, except for the different ϕ angle, with the Model C of the article by Cucinotta,[61] we removed the above mentioned groups from **M2** to obtain **M2m**. The results are reported in Table 4.10. For what regards the g-values, no significant differences were found with respect to **M2**, confirming all the observed trends of the previous model. Indeed, plotting the variation of the γ_1 angle in function of the α angle (see Figure 4.17) the **M2** and **M2m** trends are superimposable suggesting a limited importance of the two aldehydes on the magnetic structure without undermine their role in the orientation of the two H_w atoms.

The small deviation between Model C and **M2m** on γ_0 for $\alpha = 0°$ can be explained with the different ϕ values used in the two models (0° in former and 126° in latter), since the difference in ϕ deviation as only a limited effect on E_0 and E_1 of few degrees and cm^{-1}, respectively (vide supra). We can conclude that the good agreement between the experimental easy axis orientation and the computed one in **M2m** (Model C) is due to the unsufficient reduction of the $E_0 - E_1$ energy gap below the switch activation energy quantum. Therefore, we can consider such a modelization as a good operative approximation to reproduce the experimental energy ladder and the orientation of the magnetic easy axis. As a drawback, it can be very risky to use it to extrapolate magneto-correlation trends without a validation procedure with an accurate model as **M1**. This is the reason why the computed trend of the easy magnetization axis is only roughly similar to the more reliable ones given by **M1** and **M2m**.

As in **M2**, the removal of the water molecule made the easy axis rotate from the experimental orientation to a $\gamma_0 = 78.2°$, still in agreement with the results reported.[61] A very similar ladder to **M2** has been found, as expected. The two aldheyds were too far from Dy(III) to produce a significant effect.

	Exp	*Opt*	30°	45°	52°	59°	90°	129°	171°	180°	200°	220°	225°	229°	270°	340°	350°	355°
							Principal g-values of the ground Kramer doublet											
g_x	3.4	1.1	.8	1.0	1.1	1.0	0.3	0.2	1.1	1.1	0.9	1.1	1.1	1.0	0.2	0.7	1.0	1.1
g_y	4.9	7.8	3.9	6.0	7.3	6.1	0.9	0.6	8.0	8.0	4.9	6.8	7.5	6.0	0.6	2.9	6.2	8.0
g_z	17.0	12.8	16.4	14.4	13.3	14.3	19.0	19.2	12.6	12.5	15.5	13.7	13.0	14.4	19.2	17.3	14.3	12.6
							γ_0 Angle between experimental and calculated g_z											
		22.4°	4.3°	14.2°	36.3°	63.7°	81.2°	82.7°	53.3°	32.6°	8.4°	19.7°	36.5°	66°	82.2°	80.4°	72°	74.2°
							Energy Levels (cm^{-1})											
E_0	0	0	0	0	0	0	0	0	0	0	0	0	0	0	0	0	0	0
E_1	52	18	22	19	17	19	43	49	17	17	20	18	18	19	47	25	19	18
E_2	112	128	130	128	128	128	137	139	127	127	128	127	126	127	139	131	129	128
E_3	198	201	204	202	201	202	214	218	200	200	202	201	200	201	217	206	202	202
E_4	287	293	296	294	294	294	305	308	291	291	293	292	292	294	307	297	294	293
E_5	400	369	371	370	369	370	382	383	365	366	368	369	369	369	385	373	370	369
E_6	454	459	460	458	457	457	469	470	452	454	457	458	458	457	476	463	459	459
E_7	574	610	610	608	606	607	618	620	603	604	608	609	609	608	627	615	611	610

Table 4.10: Results of the calculations on **Model 2m**

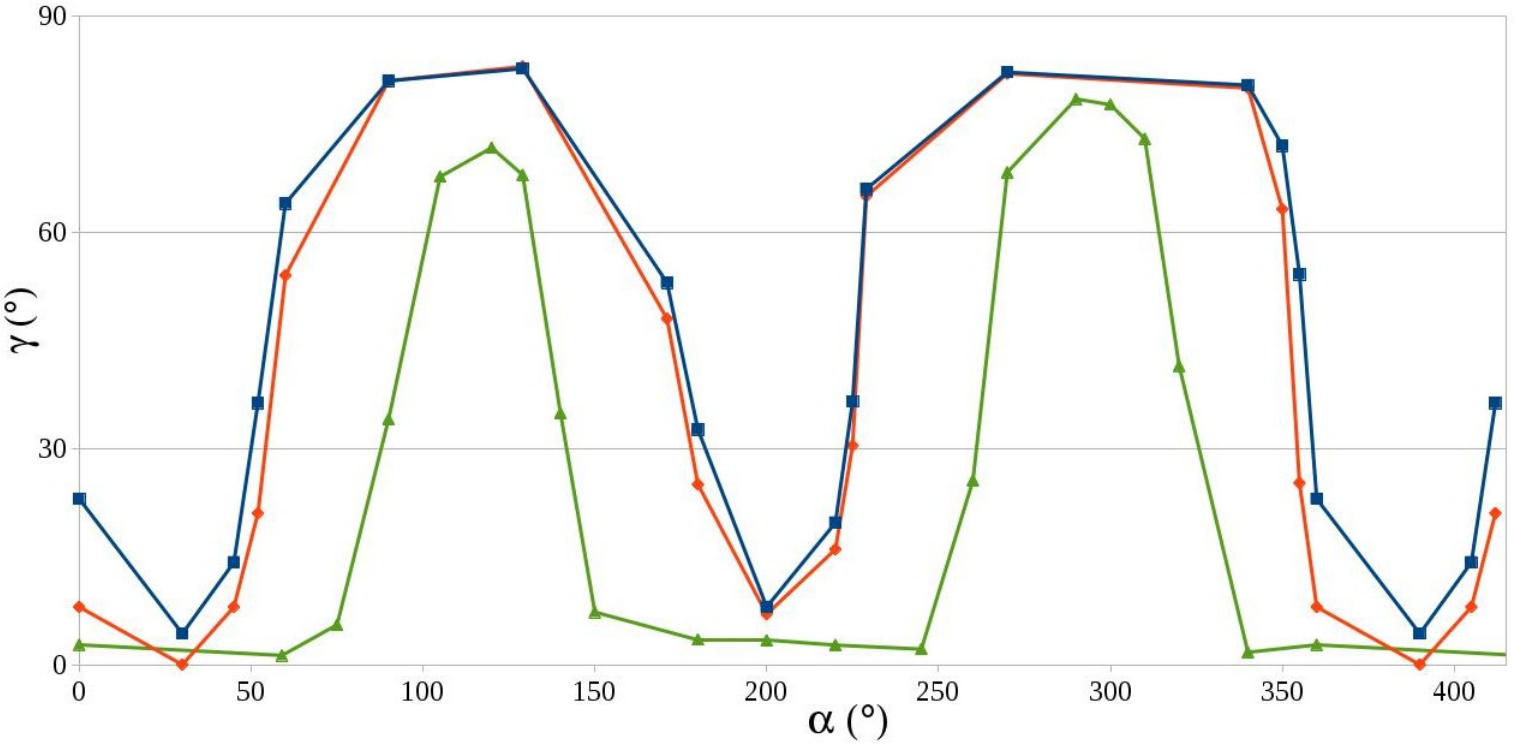

Figure 4.17: Angle between the calculated and the experimental main magnetic axis in function of the rotation of the water molecule for **M1**(green), **M2**(orange) and **M2m**(blue).

Influence of the Dihedral angle The influence of the dihedral angle ϕ was investigated performing single point calculations on model **2m** (see tables 4.11 and 4.12). For the two most significant values of the rotation parameter α (0° and 90°) the angle ϕ was changed into a value of 90° (plane of the water perpendicular to the Dy-O_w bond) and 180° (plane of the water parallel to the Dy-O_w bond). It is worth to stress that this last option corresponds to the model published by Cucinotta *et al.*[61] (model C) on which the magneto-structural correlations where performed. The variation of the dihedral angle seems not to influence significantly nor the orientation γ_0 of the main magnetic axes neither the energy ladder. For α equal 0, the γ_1 angles fluctuates of about 8° around the orientation computed for the otpimized position, with a better agreement with the experimental value found for $\phi = 180°$. Regarding the energy of the excited states, from E_2 to E_3 the variation is below 10 cm^{-1}), while from E_4 to E_5 the range of variation scales up from 20 cm^{-1} from the fourth excited state to more than 100 cm^{-1} for the seventh one. For the α equal 90° geometry, with $\phi = 180°$, the trend looks the same. However, the dihedral angle

	α		0°			90°	
	ϕ	90°	126°(*opt*)	180°	90°	126°(*opt*)	180°
	Principal g-values of the ground Kramers doublet						
g_x	3.4	1.1	1.0	0.6	0.4	0.3	0.2
g_y	4.9	7.5	5.4	2.8	1.4	0.7	0.3
g_z	17.0	13.1	14.9	17.3	18.6	19.1	19.5
	γ_0 Angle between experimental and calculated g_z						
		15.1°	8°	3.7°	79.3°	81.1°	83.4°
	Energy Levels (cm^{-1})						
E_0	0	0	0	0	0	0	0
E_1	52	18	15	23	36	39	60
E_2	112	127	118	129	137	129	143
E_3	198	197	185	203	209	201	224
E_4	287	284	272	297	299	289	315
E_5	400	361	338	383	375	359	398
E_6	454	450	412	486	456	435	494
E_7	574	585	530	646	593	561	651

Table 4.11: Results of the calculations on model **2** for dihedral angle $\phi = 90°, 126°, 180°$ for angles $\alpha = 0°, 90°$

influences the flipping process between the two orientations. Cucinotta *et al.*[61] reported that the orientation of the main magnetic axis experiences an abrupt change between the two extreme directions (the experimental and the perpendicular one). The switch is not gradual and happens about

60°, while in our model the process is gradual an at α equal to 60° the magnetization axes experiences an intermediate orientations (vide supra). For this reason calculations were performed varying the α angle with $\phi =$ 90°. The results are shown in table 4.12. The results are in agreement with those computed in the Cucinotta's paper: the flipping turns out to be again kind of abrupt again more abrupt for $\phi = 90°$. At $\alpha = 60°$ the rotation of the easy axis is only 26° against 54° for the same α but ϕ = 126°, the one we found in the optimized position. The best agreement with the experimental data is again found for 30°. This behaviour could be explained by the increasing of the energy difference between the first two doublets, in analogy with what has already been observed for the different periodicity in **M1** and **M2**. A more accurate mapping of the electronic structure in function of the α angle, i.e. one or two degree instead of 15° as in Cucinotta *et al.*, could show again the intermediate position even in a narrower range than **M1**.

	α	0°	30°	45°	60°	90°
Principal g-values of the ground Kramers doublet						
g_x	3.4	1.1	0.6	0.7	1.0	0.4
g_y	4.9	7.5	2.3	3.0	5.7	1.4
g_z	17.0	13.1	17.8	17.1	14.3	18.6
γ_0 Angle between experimental and calculated g_z						
		15.1°	3.3°	6.5°	26.2°	79.3°
Energy Levels (cm^{-1})						
E_0	0	0	0	0	0	0
E_1	52	18	28	25	20	36
E_2	112	127	134	133	130	137
E_3	198	197	205	205	202	209
E_4	287	284	292	293	291	299
E_5	400	361	368	368	367	375
E_6	454	450	457	456	452	456
E_7	574	585	592	592	588	593

Table 4.12: Results of the calculations on model **2** for dihedral angle $\phi = 90°$ for different angles α

Model 3, 4 and 5

M3 was obtained adding three Na^+ ions in their crystallographic positions to **M2** structure and replacing the CH_2O molecules with $HCOO^-$ ones (see Figure 4.10). **M3** was chosen because it resembles the model used in Chilton *et al.*,[63] except by the presence of the two formate ions. Their

addiction was intended to restore both the original nature of the chemical groups and the neutrality of the whole system (see Computational Methods). However, as showed in **M2** the role of these two groups are only marginal and, therefore, we can confidently compare our results with those obtained by Chilton *et al.*[63] The results are reported in Table 4.13. At difference with **M1** and **M2m**, for **M3** calculations were performed only for $\alpha = 0°$ and 90°. In agreement with Chilton, no reorientation of the easy axis of magnetization was observed ($\gamma_0 = 5.5°$ and 3.5° for $\alpha = 0°$ and 90°, respectively). The reason of such a behavior can be now explained by the large $E_0 - E_1$ separation with respect to the switch activation energy quantum involved in the water rotation, preventing, de facto, the flip between the two states even at α= 90°. Very strong Ising character was found for both geometrical configurations (see Table 4.13) with no significant rhombic contributions. Such result compared to the ones obtained for **M1** and **M2** gives a strong indication about the relevance of a proper modelization of the electrostatic environment around the Dy(III) ion. In this framework, the present model shows the bias constituted by the arbitrariness of having the three Na^+ ion with their coordination sphere unsaturated. To overcome such a bias, **M4** was built in such a way that the Na^+ ions were fully coordinated by adding four more formate groups and two water molecules, always in their own crystallographic positions. The model is now more chemically sound but at the cost of increasing the charge from 0 to -4 . The non-innocence of even such a change in the modelization is witnessed by the results reported at Table 4.13. Indeed, the easy axis of magnetization was found at γ_0 values of 88° and 84° for $\alpha = 0°$ and 90°, respectively. This means that even if the inclusion of the formate ions and the water molecules can be considered an alteration of the second-third coordination sphere of the Dy(III) ion, their effect on its electrostatic environment is not at all negligible because strongly stabilized the E_1 until it becomes the ground state even for $\alpha = 0°$. In order to verify it, we added three point charges mimicking three Dy(III) ions corresponding to three neighbor Dy(DOTA) complexes (see Computational Details) and put in their own correspondent crystallographic positions (**M5**). The net total charge passes from -4 to 1.48. Such a model is very close to the Model A/A' proposed by Cucinotta *et al.* where acetates were used instead of out formiates and four explicit Na ions were used at the place of Dy^{3+} ions. In this case the easy axis of magnetization shows again no reorientation, but differently from **M4**, γ_0 values of 4.6° and 11.9° (see Table 4.13) were found for $\alpha = 0°$ and 90°, respectively. A strong Ising character was confirmed for $\alpha = 0°$ and at a

		model 1		model 2		model 3		model 4		model 5	
	Exp	0°	90°	0°	90°	0°	90°	0°	90°	0°	90°
					Principal g-values of the ground Kramers doublet						
g_x	3.4	0.3	1.0	1.0	0.3	0.0	0.2	0.5	0.0	0.1	0.9
g_y	4.9	0.7	6.1	5.4	0.7	0.0	0.3	1.8	0.1	0.3	4.1
g_z	17.0	19.2	13.9	14.9	19.1	19.6	19.1	18.0	19.6	19.5	15.6
					γ_0 Angle between experimental and calculated g_z						
		2.8°	34.1°	8°	81.1°	5.5°	3.5°	88.0°	84.4°	4.6°	11.9°
					Principal g-values of the second Kramers doublet						
g_x		0.43	1.8	1.7	0.3	0.9	0.3	0.9	0.9	0.7	1.5
g_y		1.12	4.5	4.4	1.1	1.1	0.8	1.1	0.9	1.0	2.8
g_z		17.95	11.9	12.9	18.2	18.0	18.1	17.3	18.7	18.4	14.0
					γ_1 Angle between experimental and calculated g_z						
		80.1°	44.0°	56.1°	4.4°	76.5°	77.5°	8.3°	7.1°	81.0°	67.1°
					Energy Levels (cm^{-1})						
E_0	0	0	0	0	0	0	0	0	0	0	0
E_1	52	47	18	15	39	78	35	16	57	53	15
E_2	112	140	123	118	129	132	115	105	120	129	110
E_3	198	212	193	185	201	198	173	164	191	193	172
E_4	287	298	281	272	289	263	246	246	270	267	250
E_5	400	369	352	338	359	307	292	300	328	320	304
E_6	454	451	432	412	435	355	344	357	388	378	364
E_7	574	590	568	530	561	429	426	437	473	480	471

Table 4.13: Results of the calculations on DyDOTA system with the **Models 1,2,3,4,5** for the optimized position and the one rotated by 90°.

lesser extent even for $\alpha = 0°$ for which some rhombic contributions were instead found. Even if **M5** formally resembles very closely to the Model A/A' reported in Cucinotta *et al.*,[61] the behavior is completely different since the latter showed a change in the orientation of the easy axis of magnetization of about 90° instead of not showing almost any rotation effect. Such result, again, stresses the tiny modelization effects when partial, not to say "arbitrary", model are chosen.

Analyzing the computed energy values for the first eight multiplets for **M3-5** models (see Table 4.13) several important information can be extracted. First of all, comparing the computed trend for the ground and the first excited doublets for the three models, it results that the rotation of the apical water molecule has opposite effects on them: strongly destabilizing the former and slightly stabilizing the latter. Such a consideration becomes evident from the E_0 and E_1 values: in **M3** and **M5** the first excited state is stabilized passing from $\alpha = 0°$ to $\alpha = 90°$ while in M4 becomes, instead, destabilized. Moreover, as already pointed out

before, the energy quantum involved in the water rotation in $0° < \alpha < 90°$ was still found similar than in M1 and with slightly differences among the three models: 43 cm^{-1}, 41 cm^{-1}, 38 cm^{-1} for **M3**, **M4**, and **M5**, respectively. The agreement with the experimental E_0 and E_1 values is, however, qualitative for **M3** and **M4** while an excellent agreement was found, instead, for **M5** (see Table 4.13).

The strong dependence on the chosen model is also evident comparing the $E_2 - E_7$ values. In the case of **M3** and **M4** the values get stabilized passing from $\alpha = 0°$ to $\alpha = 90°$ while for **M5** we observed a destabilization trend as already found in **M2m**. The agreement with the experimental values is good for **M3** and **M5** up to E_4 and it gets worse for higher energys. For **M4** the agreement is overall poorer.

4.2.4 The role of water molecule

In the previous sections we have given a detailed insight on how crucial can be the correct modelization of lanthanide ion environment on determining the magnetic properties of the system. In details, we have shown that not only the first, second or third coordination sphere contributions are important but the correct electrostatic representation of the whole crystal around the lanthanide ion is a mandatory requisite for a proper description of the system under study.

The computed periodic trend of the variation of the doublets energy ladder in function of the α value in absence of a crystallographic symmetry suggested us that the interaction between Dy(III) ion and the water molecule could hide a more complex "courtship ritual" than the expected one given simple electrostatic interactions. For these reasons, we performed a series of further calculations aimed to shed some light on this appealing topic.

Indeed, the statement that the covalency in lanthanide complexes is not strong is more or less valid.[171] A different approach to study the electrostatic influence of the ligands on the direction of the magnetization is the following: from the total electronic density, at the end of the *ab initio* calculation, a fit is performed within the LOPROP scheme[170] obtaining an effective charge (q_i), dipole (p_i) and quadrupole tensor (Q_i) for each i-th atom. The electrostatic potential felt by the Ln(III) ion is then calculated with the equation:

$$V(\vec{r}) = \sum_{i}^{N} \frac{q_i}{||\vec{r_i} - \vec{r}||} + \frac{\vec{p_i} \cdot \vec{r_i}}{||\vec{r_i} - \vec{r}||^3} + \frac{\vec{r_i} \cdot (Q_i \times \vec{r_i})}{||\vec{r_i} - \vec{r}||^5} \tag{4.3}$$

where r_i is the position of the i-th atom respect to the r position in which

the potential is calculated and N is the total number of atoms in the ligands. This formula have been implemented in the CAlculated Molecular Multipolar ELectrostatics code (CAMMEL), developed at the Inorganic Theoretical Chemistry research group at the University of Rennes, in which it is possible to calculate and display the electrostatic potential at a radius from the metal atom given by the user, along with the three axis of the g-tensor. Its intensity is represented with a color code (blue = low potential, red = high potential). For the sake of graphics, it can represent also irregular surfaces in which the height of the surface is also proportional to the value of the potential, since this representation is considered more intuitive. With this procedure it is also possible to study each single component of the sum in Equation 4.3, namely the coulomb, dipole and quadrupole potential, to identify which one is the driving one. This, speaking in terms of future development, can also lead to a finer rationalization of the correlation between the environment and the easy-axis direction. The method uses the LOPROP charges due to their high reliability[172] and it has been already validated in different works.[173] It is important to stress out that this tool does not aim at the prediction of any magnetic behaviour (already the *ab initio* calculation is intended to do this), but to a rationalization of the electronic structure.

Origin of the rotation of the easy magnetization axis

The common assumption is that the electrostatic interactions are the main responsible of the ligand field effects in the lanthanides containing complexes and, therefore, their magnetic properties are strongly dependent by them. We have decided to perform an electrostatic contribution analysis of the potential generated by all the ligands around the Dy(III) ion. In particular, we have performed a multipolar analysis through which it has been possible to access also to the single charge, dipolar and quadrupolar contributions (LoProp, See computational Details) on **M1** and **M2m** for the following α values: 0°-90°-120° and 0°-59°-90°, respectively. We have chosen these two models, i.e. the most accurate model (**M1**) and the simplest one (**M2m**), to have clear indications without any loss of generality.

The results of the CAMMEL analysis for both models are reported in Figures 4.18. The emerged picture indicates the presence of four minima in the whole electrostatic potential which point toward the four coordinating carboxylic oxygen atoms. From the multipolar decomposition it is possible to ascribe the presence of the minima to the dipolar and quadrupolar contributions while the charges potential shows a more isotropic shape,

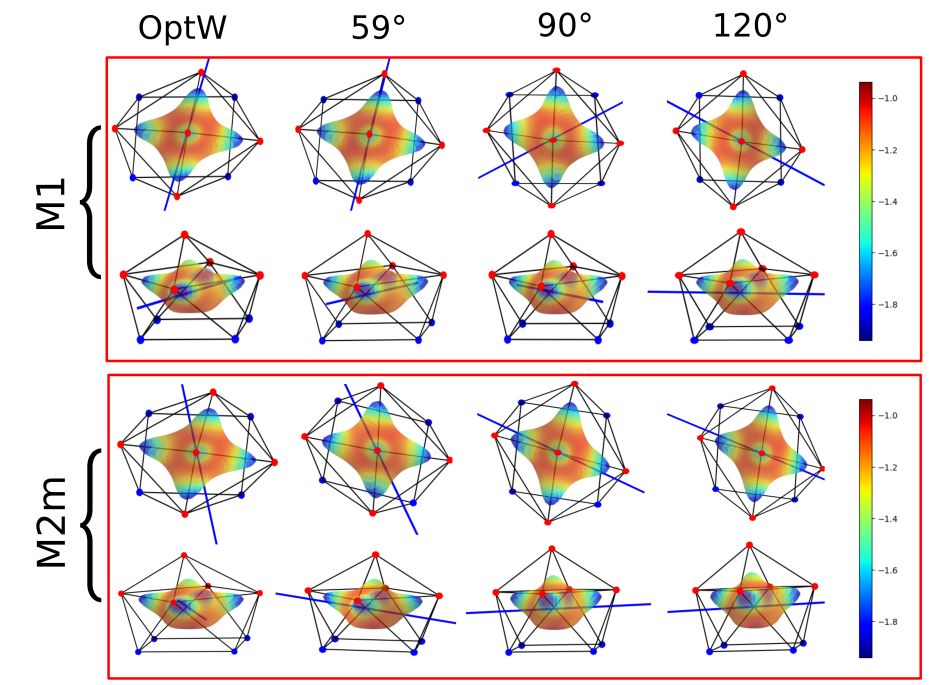

Figure 4.18: CAMMEL analysis of the total electrostatic potential around the Dy ion for **M1** and **M2m** for differents α angles. OptW corresponds to the position with $\alpha = 0°$. Only the atoms directly bonded to Dy ion are showed. Oxygens and Nitrogens are red and blue respectively. The orientation of the easy axis of magnetization for each geometry is also shown

as shown in figure 4.19. Such a scenario does not show any appreciable differences both for the two different models and for the two α sets of values and clearly indicates that the electrostatic environments show two equivalent preferential orientations for the easy axis of magnetization. For this reason, the analysis cannot give any indication on which of the two directions can be the one associated to the ground doublet. However, from the analysis of the plots reported in figure 4.18, it is not possible to grasp any evident information about the water molecule role. In this regard, we have tried to extrapolate the single electrostatic water molecule contributions plotting the difference between the potentials calculated for **M1** and its counterpart without the water molecule for the two sets of α values (see Figure 4.20). In both cases, we can observe that the quadrupole moments represent the strongest electrostatic contribution as expected for

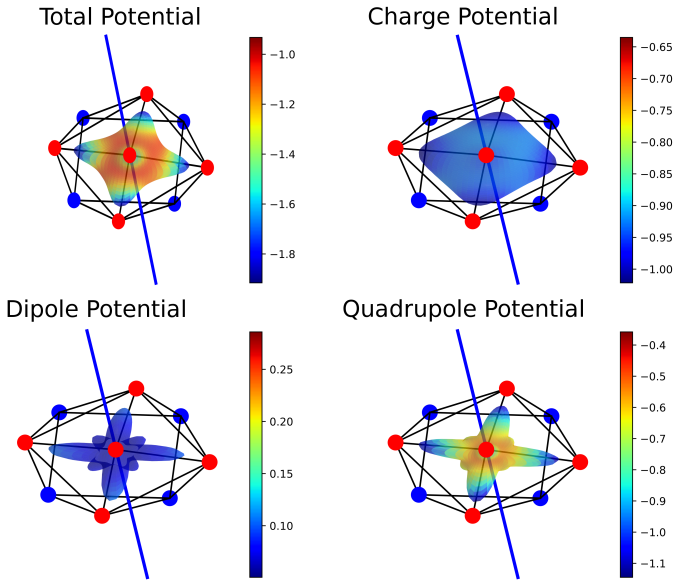

Figure 4.19: CAMMEL analysys: Different multipolar contributions of the total electrostatic potential around the Dy ion for **M2m** and $\alpha = 0°$. Only the atoms directly bonded to Dy ion are showed. Oxygens and Nitrogens are red and blue respectively. The orientation of the easy axis of magnetization for each geometry is also shown

a water molecule[174] (see also Figure 4.20) but a variation of the potential in function of the α values is observed only for the dipolar component. To verify if eventual variations for the quadrupole could be hidden by isotropic contributions, we have also re-plotted the maps differences subtracting the map difference obtained for $\alpha = 0°$ as reference (see Figure 4.21). The new plots evidenced a variation in the potential also for the quadrupole contribution and of the same order of magnitude of the dipolar component. In a nutshell, we can expect that the quadrupolar moment of the water molecule should have a major role in the re-orientation mechanism of the easy axis of magnetization while a minor role is expected for the dipole. In the case of the charge, we can exclude any significant role in it. Strong of such results, we have tried to put them on a stronger computational basis. In this regard, we have performed CASSCF /CASSI-SO calculations for **M1** for the set of α values with the trick of substituting the water molecule atoms with their multipolar expansion (**M1#**). With such an expedient we can evaluate the whole and the single electrostatic contributions and

readily verify their effects on the energy ladder and, consequently, on the orientation of the easy axis of magnetization. The results are reported in Table 4.14.

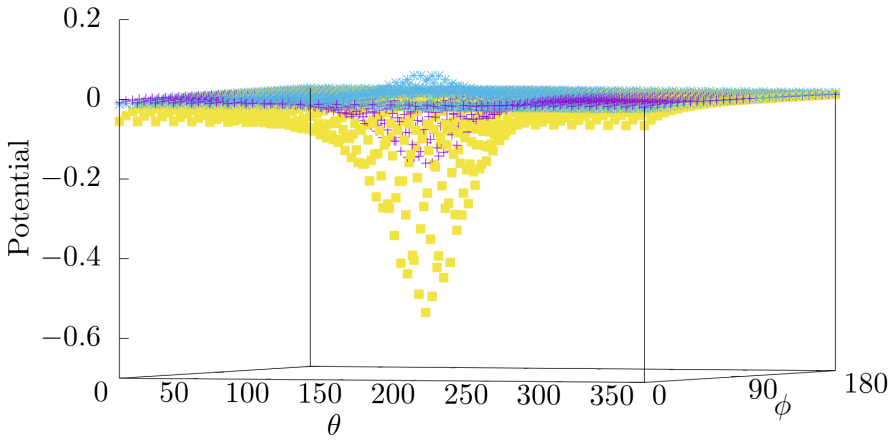

Figure 4.20: CAMMEL analysis of the total electrostatic potential of the water moelcule directly bonded to the Dy ion for **M1** and $\alpha = 0°$. The potential have been decomposed in the single charge (purple), dipolar (blue) and quadrupole contribution (yellow)

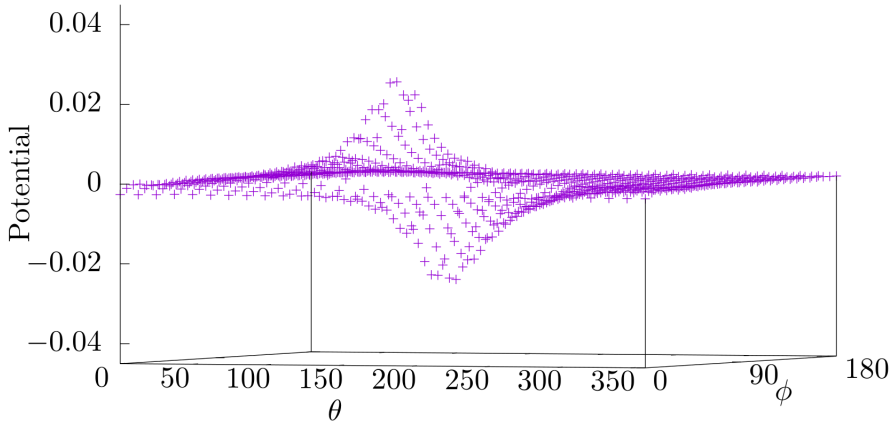

Figure 4.21: Differences between the quadrupolar moments, obtained from CAMMEL analysis, for $\alpha = 0°$, 90° of the water molecule in **M1**.

The results obtained for **M1#** indicate that the whole electrostatic contribution coming from the water molecule is able to rotate the easy

axis but not completely as found when the water molecule is explicitly considered ($\gamma_0 = 46.3°$). Comparing the E_0 and E_1 values for the $\alpha = 0°$ and 120° it is possible to assign an energy quantum of about 60-70 cm^{-1} ($E^{\sharp}_{rot}$+$E^{\sharp}_{cross}$). Such an energy value can therefore explain the computed intermediate γ_0 value since the starting E_1 is at 58 cm^{-1}, too high in energy to observe a complete flip. Interestingly, the computed ($E^{\sharp}_{rot}$+$E^{\sharp}_{cross}$) energies for **M1#** is the same previously found for the **M1** model for ($2E_{rot}$+E_{cross}). The two energies expressions describe, indeed, the same process: the only difference is that while for the former a total localization of the state is possible ($E_{1,\alpha=0°} < 50$ cm^{-1}), for the latter the localization is not possible because $E_{1,\alpha=0°} > 50$ cm^{-1}). Such result is important because it demonstrates that the rotation of the easy axis is almost totally driven by an electrostatic constant energy quantum. For this reason, the crucial importance of having an accurate description of the energy ladder must be stressed once again. This is possible only when orbital contributions are included and a reliable environment is modeled, too. However, slight orbital contributions can be hinted by looking at the differences found for $\alpha = 0°$ where a difference in γ_0 of 4° has been found. On the other hand, the difference in the energy ladders is significant and in the perspective of the energy flipping of the first two doublets can be a severe bias.

In the light of these results we have also investigated the eventual different roles of the electrostatic potential always using the **M1#**. The results are reported in Table 4.15. In agreement with the pure electrostatic approach, the driving force of the easy axis rotation is mainly due to the quadrupole moment (80%, $\gamma_0 = 36.2°$) and the charge contributions (15%, $\gamma_0 = 6.5°$) while the dipole moment has only a minor and opposite effect.

We have also performed *ab initio* calculations for **M1** and **Mi#** ($\alpha = 120°$) where the Dy-O_w bond was stretched for a maximum of 0.2 $\AA$, as shown in Table 4.16. The choice of the α angle has been motivated by the fact that the removal of the water molecule in **M1** leads to a $\gamma_0 = 4°$ and, therefore, it can give further hints about the nature of the Dy-O_w interaction and the factors ruling the rotation of the easy axis. Focusing on the energy trends of E_0 and E_1, in the case where orbital contributions for the water molecular are included, the E_1 values got stabilized as the Dy-O_w bond got stretched. This behavior is expected since the system tends toward the situation where the water molecule is absent, and, therefore, to a situation where E_1 must flip with E_1 in the range $70° < \alpha < 90°$. Indeed, associated to the E_1 stabilization a decrease of the γ_0 values is observed. Opposite situation is observed for **M1#**: E_1 energies get destabilized.

α		**M1**						**M2m**					
		0°(Opt)		90°		120°		0°(Opt)		59°		90°	
	Exp	*Orb*	*Charge*	*Orb*	*Charge*	*Orb*	*Charge*	*Orb*	*Charge*	*Orb*	*Charge*	*Orb*	*Charge*
		Principal g-values of the ground Kramers doublet											
g_x	3.4	0.3	0.0	1.0	0.1	0.9	0.5	1.1	0.1	1.0	0.3	0.3	0.0
g_y	4.9	0.7	0.1	6.1	0.2	4.1	1.8	7.8	0.6	6.1	0.9	0.9	0.15
g_z	17.0	19.2	19.8	13.9	18.7	16.0	14.6	12.8	19.2	14.3	18.1	19.0	19.5
		Direction Cosines g_z of the first Kramers doublet											
a	0.6700	0.684155	0.733288	0.689162	0.7325531	0.419056	0.670775	0.687617	0.703587	0.504959	0.718865	0.338244	0.351829
b'	−0.2920	−0.327447	−0.335766	0.293259	−0.252991	0.816357	0.485637	0.093666	−0.336994	0.726934	−0.226048	0.899246	0.907963
$c*$	0.6826	0.651698	0.591228	0.662612	0.6319511	0.397433	0.560551	0.720007	0.625620	0.465385	0.657370	0.277393	0.227639
		γ_0 Angle between experimental and calculated g_z											
		2.8°	6.8°	34.1°	5.1°	71.7°	46.3°	22.4°	4.5°	63.7°	4.9°	81.2°	82.8°
		Energy Levels (cm^{-1})											
E_0	0	0	0	0	0	0	0	0	0	0	0	0	0
E_1	52	47	58	18	16	20	6	18	18	19	11	43	27
E_2	112	140	131	123	105	122	97	128	107	128	104	137	109
E_3	198	212	181	193	151	194	144	201	153	202	152	214	160
E_4	287	298	261	281	236	281	229	293	238	294	239	305	246
E_5	400	369	335	352	307	351	298	369	311	370	314	382	321
E_6	454	451	422	432	386	430	378	459	395	457	399	469	405
E_7	574	590	529	568	480	566	470	610	491	607	499	618	504

Table 4.14: Results of the calculations on **M1** substituing the apical water molecule with the multipolar expansion

α		0°	120°					
	Exp	Orbitals	PC	D	PC+D	Q	PC+D+Q	Orbitals
	Principal g-values of the ground Kramers doublet							
g_x	3.4	0.3	0.7	0.5	0.5	0.7	0.5	0.9
g_y	4.9	0.7	3.5	1.9	2.1	7.6	1.8	4.1
g_z	17.0	19.2	16.5	18.2	17.8	12.6	14.6	16.0
	Direction Cosines g_z of the first Kramers doublet							
a	0.6700	0.684155	0.684684	0.655762	0.679510	0.643919	0.670775	0.419056
b'	−0.2920	−0.327447	−0.182068	−0.278592	−0.245083	0.329497	0.485637	0.816357
$c*$	0.6826	0.651698	0.705733	0.701685	0.691521	0.690507	0.560551	0.397433
		γ_0 Angle between experimental and calculated g_z						
		2.8°	6.5°	1.45°	2.72°	36.2°	46.4°	71.7°
	Energy Levels (cm^{-1})							
E_0	0	0	0	0	0	0	0	0
E_1	52	47	16	31	18	8	6	20
E_2	112	140	124	144	122	110	97	122
E_3	198	212	191	225	185	167	144	194
E_4	287	298	293	344	281	264	229	281
E_5	400	369	403	482	382	372	298	351
E_6	454	451	541	662	506	512	378	430
E_7	574	590	731	919	675	689	470	566

Table 4.15: Results of the calculations on **M1** for $\alpha = 120°$ substituing the apical water molecule with different multipolar expansions: point charges (PC), dipole (D), point charges and dipole (PC+D), quadrupole (Q), total (PC+D+Q).

Such result indicates that in **M1#** for $\alpha = 120°$ E_0 and E_1 are already flipped. For this reason, we can observe a similar trend of the E_1 destabilization as in M1 but associated to a sudden γ_0 decrease. while in **M1** a smoother decrease (overlap vs localized coulomb interaction) was found. Moreover, considering that we have shown that in M1# for $\alpha = 120°$ E_0 and E_1 are already flipped, we can reconsider the nature of the ($E^{\sharp}_{rot}$+$E^{\sharp}_{cross}$) energy quantum. Indeed, comparing the E_0 and E_1 values obtained for $\alpha = 0°$ we can now confidently say that the energy quantum of the water molecule rotation can be divided in about 45-50 cm^{-1} (75%) coming from an electrostatic contribution while about 10-15 cm^{-1} (25%) from an orbital contribution. Such a value is also compatible with the difference of few degrees computed for **M1** and **M1#** at $\alpha = 0°$. Such results undoubtedly indicate that the rotation of the easy axis is the result of the complex balancing of electrostatic and covalent contributions.

Å		0		0.05		0.1		0.15		0.2		noH_2O
	Exp	*Orb*	*Charges*	*Orb*	*Charges*	*Orb*	*Charges*	*Orb*	*Charges*	*Orb*	*Charges*	
					Principal g-values of the ground Kramer doublet							
g_x	3.4	0.9	0.5	0.9	0.6	1.0	0.7	1.0	0.7	1.0	0.7	0.6
g_y	4.9	4.1	1.8	5.0	3.5	5.8	3.9	6.5	4.0	6.9	3.8	2.9
g_z	17.0	16.0	14.6	15.1	14.6	14.3	15.0	13.7	15.4	13.3	15.8	17.3
					Direction Cosines g_z							
a	0.6700	0.451893	0.670775	0.455538	0.721735	0.504543	0.723114	0.564007	0.714081	0.623279	0.705448	0.658457
b'	−0.2920	0.776779	0.485637	0.774228	0.207586	0.707716	0.038142	0.605702	−0.048953	0.464996	−0.099936	−0.248230
$c*$	0.6826	0.438642	0.560551	0.439381	0.660308	0.494545	0.689675	0.561268	0.698349	0.628731	0.701681	0.710505
					γ_0 angle between experimental and calculated g_z							
		71.7°	46.3°	67.7°	29.1°	62.0°	19.2°	54.2°	14.2°	44.7°	11.2°	3.0°
					Energy Levels (cm^{-1})							
E_0	0	0	0	0	0	0	0	0	0	0	0	0
E_1	52	20	6	18	7	17	8	16	10	16	11	27
E_2	112	122	97	122	101	123	106	123	109	124	112	146
E_3	198	194	144	193	152	193	159	193	166	194	171	231
E_4	287	281	229	283	239	285	249	288	257	291	265	356
E_5	400	351	298	359	316	367	332	376	346	384	359	506
E_6	454	430	378	448	405	465	431	482	453	499	473	702
E_7	574	566	470	595	515	622	557	648	593	673	625	982

Table 4.16: Results of the calculations on DyDOTA system, model **M1**, in function of the Dy-O_w stretching in Angstrom for the rotation of 120°. Calculations substituing the H_2O with its multipole expansion have been performed

4.3 LnDOTA Isostructural Series

The isostructrural series of LnDOTA had been already investigated from experimental and computational point of view by Boulon *et al.*[156] by a combined employment of CASSCF/CASSI calculations, DC/AC single crystal magnetometry and luminescence spectroscopy. The results showed only a partial agreement between the directions of the computed and measured axes of magnetization. However, from the article the main weakness regarding the *ab initio* calculation could be evinced: the geometry employed has been the same one for the Dy derivatives of the article by Cucinotta *et al.*[61] by simple replacement of the central dysprosium ion with the other lanthanides of the series. Even if the whole series was found to be isostructural, this is a very strong geometry approximation.

On the other hand the experimental easy axes' orientation had been determined by single crystal magnetic measurements.[175,176] New measures have then been performed by Dott. Mauro Perfetti by cantilever torque magnetometry (CTM). CTM only probes the anisotropic part of the magnetization and therefore has higher sensitivity than single crystal magnetometry. Moreover the possibility to measure the magnetic anisotropy up to relatively high temperatures allows one to get an independent estimate of the gap between the ground and first excited doublet in lanthanide complexes.[131,177]

These new experimental results provided the possibility to validate our rigorous computational protocol, already applied on DyDOTA, tuned on the most recent advances in inorganic computational chemistry. Moreover the validation of the protocol for the other complexes of the series would be based on an experimental method able to provide the spacing of the energy levels of compounds for which the energy ladder had not been determined by other techniques, for instance luminescence measurements as in DyDOTA.[61]

4.3.1 Computational Method

Choice of the model

The calculations performed for the Dy derivative demonstrate that for these complexes any symmetry and structural approximation can lead to huge errors in the orientation of the anisotropy axes if not analyzed in details. Hence, structures of Nd, Gd, Dy, Ho, Er and Eu were taken from Crystallographic Cambridge database while for Ce and Pr the structure was solved. The Tb derivative was not investigated *ab initio* due to the good agreement already achieved between experiment and theory in the

paper by Boulon *et al.*[156] For the Yb complex instead the x-ray structure was not available and it was not possible to obtain it experimentally. The geometries resolved by x-ray diffraction were employed: the choosen model consisted of the lanthanide ion, the DOTA ligand, and the apical water molecule directly bonded to the lanthanide, i.e. analogues to the **M2m** model of the previous section. The cell parameters appear very similar throughout the series and, along with the isostructurality of the crystal packing, it partially justify the employment of the same model for all the series.

The position of the hydrogen atoms belonging to the water is responsible for a gradual change in orientation of the easy axis between two perpendicular positions, as investigated for the DyDOTA derivative. For this reason, all the calculations performed in this study were performed on experimentally determined structures, and the position of the water's hydrogen atoms was keep fixed on the positions optimized for the Dy derivative taking into account the interactions with neighboring chemical groups, as discussed in the previous chapter. Indeed, analysing the crystal packing along the whole structural series, the oxygens atoms framework around the apical water molecule is mantained for all the derivatives. Besides the carboxylic oxygens directly coordinated to the Dy ion, two other carboxylic oxygens of the neighbour LnDOTA molecules in the crystal lies at a distance less than 3 $\AA$ from the water's oxygen. Distances O_w-O_n between oxygens show a reduction in the order of the 0.2 $\AA$ passing from Ce to Dy for all the derivatives of interest, as it can be seen in table 4.18. This fact can be attributed to the diminution of the ionic radius along the series.

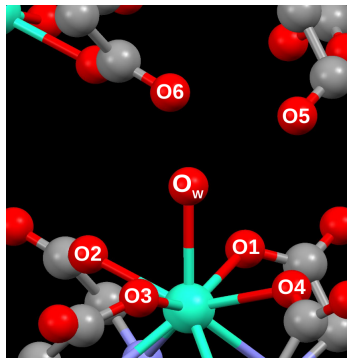

Figure 4.22: Oxygen's framework and numbering around the water molecule in LnDOTA.

Ln	*a*	*b*	*c*	α	β	γ
Ce	8.697(16)	9.239(13)	15.77(3)	83.41(15)	85.63(15)	81.39(16)
Pr	8.719(4)	9.179(5)	15.860(4)	82.71(3)	84.98(3)	80.86(4)
Nd	8.65(2)	9.23(2)	15.55(4)	82.99(19)	84.6(2)	80.4(2)
Eu	8.705(10)	9.123(7)	15.787(9)	82.57(8)	85.36(10)	81.36(8)
Gd	8.719(3)	9.110(6)	15.707(10)	82.79(5)	85.47(4)	81.43(4)
Tb	8.77(2)	9.12(2)	15.69(2)	83.02(16)	85.34(16)	81.4(2)
Dy	8.724(10)	9.046(16)	15.599(13)	83.04(11)	85.73(9)	81.66(12)
Ho	8.87(6)	9.12(3)	15.72(3)	83.2(2)	86.3(3)	81.9(4)
Er	8.697(13)	9.011(13)	15.568(17)	83.20(10)	86.30(11)	82.10(12)
Tm	8.806(10)	8.898(13)	15.74(2)	82.70(11)	85.31(10)	81.22(11)
Yb	8.738(16)	9.16(3)	15.599(18)	83.65(15)	85.88(12)	81.84(19)

Table 4.17: Cell parameters for all the LnDOTA derivatives.

Ln	*Ce*	*Pr*	*Nd*	*Eu*	*Gd*	*Dy*	*Ho*	*Er*
O_1	3.115	3.063	3.026	2.945	2.921	2.880	2.858	2.849
O_2	3.024	3.013	2.979	2.915	2.876	2.854	2.839	2.812
O_3	2.880	2.870	2.832	2.774	2.739	2.729	2.707	2.674
O_4	3.040	2.999	2.962	2.890	2.847	2.819	2.798	2.778
O_5	2.755	2.785	2.790	2.807	2.797	2.806	2.830	2.813
O_6	2.766	2.769	2.772	2.786	2.784	2.773	2.801	2.778

Table 4.18: Distances between the oxygen of the water molecule and i) the four carboxylic oxygens directly coordinated (O_1-O_4), ii) the two carboxylic oxygens of the neighbour LnDOTA molecules (O_5-O_6).

CASSCF/CASSI calculations

All the calculations were performed with MOLCAS 8.1 [101] Quantum Chemistry Software Package. The energy ladder of the electronic states for every lanthanide ion have been computed within the CASSCF/CASSI-SO method. The basis set employed is in table 4.19.The chosen active space for the lanthanides consists of the unpaired electrons in the seven $4f$-orbitals of the lanthanide ion in the oxidation state +3 : CAS (N,7), where N is 1 for Ce, 2 for Pr, 3 for Nd , 6 for Eu, 7 for Gd, 9 for Dy, 10 for Ho, 11 for Er . Due to hardware limitations, only the states with the highest spin multiplicity for each lanthanide, excluded Gd, were computed and included in the following spin-orbit calculation: 7 doublets for Ce, 21 triplets for Pr, 35 quadruplets for Nd, 7 septuplets for Eu, 21 sextuplets for Dy, 35 quintuplets for Ho, 35 quadruplets for Er. For Gadolinium were considered 1 octuplet, 48 sextuplets and 215 quadruplets.

Atom	Label	Primitives	Contraction
Dy	VTZP	[25s22p15d11f4g2h]	[8s7p5d3f2g1h]
Na	VDZ	[17s12p5d4f2g]	[4s3p]
N	VTZP	[14s9p4d3f2g]	[4s3p2d1f]
O	VTZP	[14s9p4d3f2g]	[4s3p2d1f]
C	VDZP	[14s9p4d3f2g]	[3s2p1d]
H	VDZ	[8s4p3d1f]	[2s]

Table 4.19: Contractions of the ANO-RCC basis set used for all CASSCF calculations.

The g and susceptibility tensors for each ion were computed with the SINGLE_ANISO module. For Kramers' ion, the magnetic anisotropy was investigated within the pseudospin framework and their anisotropy axes were calculated with a pseudospin $S = \frac{1}{2}$. For ions with even number of electrons the anisotropy axes were extrapolated diagonalizing the susceptibility tensor at 2 K. The Tm derivative was not computed due to the not availability of the x-ray structure.

Results and discussion

The values and the direction of the computed easy axis of magnetization are in tables 4.20 and 4.21. The angle ϵ between the computed easy-axis and the Ln-O_w bond is shown in table 4.22. By geometry considerations the LnDOTA geometry possesses a pseudo-C_4 axis along the Ln-O_w

Ln	axis	Value	a	b'	$c*$
Ce	g_x	0.719323143	−0.733058	−0.004421	0.680152
	g_y	2.063547073	−0.230784	0.942273	−0.242611
	g_z	3.000829882	0.639816	0.334815	0.691761
Nd	g_x	0.349568447	−0.738126	0.040051	0.673473
	g_y	2.759472662	−0.070829	0.988120	−0.136392
	g_z	3.318517636	0.670934	0.148376	0.726520
Gd	g_x	1.840471776	−0.707511	−0.002451	0.706698
	g_y	5.651488732	0.038386	−0.998651	0.034966
	g_z	10.122635571	0.705659	0.051866	0.706651
Dy	g_x	0.960373921	0.714018	−0.028468	−0.699548
	g_y	5.395416081	0.122245	0.988894	0.084531
	g_z	14.900410827	0.689372	−0.145873	0.709568
Er	g_x	1.966395370	0.658552	−0.430484	0.617246
	g_y	2.564767375	0.206304	0.892074	0.402047
	g_z	13.430222975	−0.723704	−0.137429	0.676288

Table 4.20: Values of the main anisotropy axes of the groun Kramers' doublet for the investigate derivatives with even number of electrons and their orientations in the crystal frame. For the gadolinium derivatives, the main magnetic axes of the zero field splitting tensor and their orientations are reported

Ln	axis	$\chi_M T$(cm^3 K/mol)	a	b'	$c*$
	x	0.0024	−0.7409	0.0526	0.6695
Pr	y	0.0337	−0.0275	−0.9985	0.0481
	z	0.0494	0.6710	0.0173	0.7412
	x	0.0099	−0.6829	−0.1010	−0.7235
Eu	y	0.0108	−0.0463	0.9944	−0.0951
	z	0.0693	−0.7291	0.0315	0.6837
	x	0.0480	0.7415	0.0023	−0.6710
Ho	y	1.6683	0.0547	−0.9969	0.0571
	z	7.5579	0.6687	0.0790	0.7393

Table 4.21: Values of the main anisotropy axes for the investigate derivatives with odd number of electrons and their orientations in the crystal frame. The axes were computed diagonalizing the Van Vleck susceptibility tensor at 2K

bond. Hence, an easy-axis or an easy-plane perpendicular to it could be expected along with the unexpected easy axis behavior as observed for the Dy derivative. Indeed, the result shows that the Ce, Pr and Nd present, even if not perfect, an easy-plane anisotropy and the easy-plane is perpendicular to the Ln-O_w bond, i.e. in the plane of the carboxylic groups. The other derivatives, instead, show a pronounced easy-axis anisotropy. The directions of the easy axes, however, are not unambiguous because they lie only for the Eu and Er compound along the Ln-O_w bond. For the Ho and Dy complexes (and for Tb as shown by Boulon *et al.*) it points in direction perpendicular to it as already seen for the Dy derivative, i.e. it is in the carboxylic plane where at least an easy-plane could be expected, as found for Ce, Pr and Nd compounds.

These results have to be compared with the previous ones already presented in the paper by Boulon *et al.*. In our case, no intermediate direction of the easy axis between the parallel and perpendicular one with respect to the Ln-0_w bond was found. Instead previously tilting angles of 58° and 48° had been reported by Boulon *et al.* for the Er and Ho derivatives, respectively. For that derivatives moreover no experimental data on the direction of the magnetization was available.

The results of the CASSCF calculations provided appear very reliable in comparison with experimental data provided by CTM. The agreement

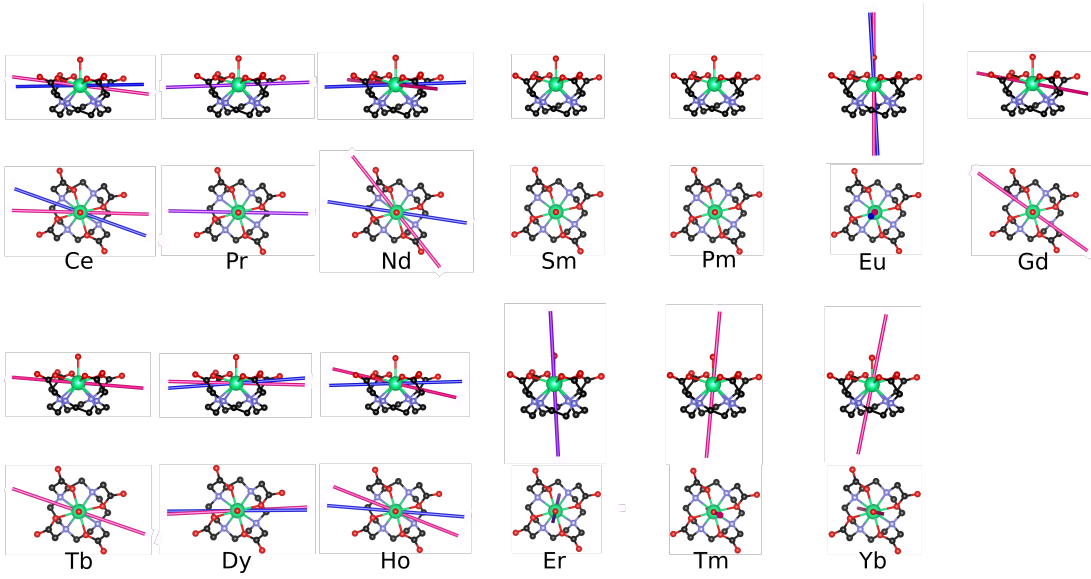

Figure 4.23: Theoretical (blue) and experimental (pink) orientation of the easy axis of magnetization for all the studied derivatives of the LnDOTA family. Violet axes indicate that the theoretical and experimental are superimposable. Data for Tb and Yb were taken from Boulon *et al.*[156]

between ϵ_{theo} and ϵ_{exp} is remarkably good for all the derivatives, as reported in table 4.22, considering an error of 5° estimated for the experimental results. The calculations correctly provide the orientation of the easy-axis with respect of the Ln-O_w bond. Problems can arise with the orientation of the easy axis inside the plane of the carboxylic oxygens, i.e. for ϵ 90°. The angle ζ between experimental and theoretical axis is reported in table 4.22. The values are in excellent agreement for Pr, Eu, Dy and Er derivatives: the angles ζ are again inside the experimental error. However, for Ce, Nd, Gd and Ho, ζ deviations of 20°, 43°, 35° and 22° respectively were observed. This is not surprising for Ce and Nd since the plane orthogonal to the Ln-O_w bond is almost an easy plane in these derivatives, making thus hard to correctly predict the orientation of the easiest anisotropy axis: the calculations however provide a correct orientation of the 'hard-axis' along the Ln-O_w bond and of the easy-plane in the plane formed by the four carboxylic groups complexing the Ln(III) ion. Regarding the Gadolinium derivative, it has a very low zero-field splitting: the four Kramers' doublets arising from the ${}^8S_{\frac{7}{2}}$ term lie within 1 cm^{-1}. Hence it can be considered isotropic at first approximation, as expected.

Ln	z-axis, *ab initio*			z-axis, experimental			$\zeta(^\circ)$	$\epsilon_{theo}(^\circ)$	$\epsilon_{exp}(^\circ)$
	a	*b′*	*c∗*	*a*	*b′*	*c∗*			
Ce	0.640	0.335	0.692	0.543	0.038	0.839	20	89	83
Pr	0.671	0.017	0.741	0.662	0.018	0.767	< 1	88	88
Nd	0.670	0.148	0.727	0.400	0.787	0.469	43	88	86
Eu	−0.729	0.032	0.684	−0.760	0.090	0.640	6	4	4
Gd	0.706	0.052	0.707	0.440	0.584	0.682	35	86	81
Dy	0.689	−0.146	0.710	0.619	−0.047	0.784	8	85	88
Ho	0.668	0.079	0.739	0.447	0.376	0.812	22	88	78
Er	0.724	0.137	−0.676	0.728	0.137	−0.672	< 1	13	13
Tm	*NOTCALC.*			0.820	−0.040	−0.570	−	−	6

Table 4.22: Director cosines in the ab'c* reference frame for all the investigated derivatives obtained by calculations and experiments. The angle ζ is the angle between the calculated and experimental axes. The angles ϵ and ϵ_{exp} are the angles between the calculated or experimental axis and the Ln-O_w bond, respectively.

However, the calculation clearly predicts also for this derivative an easy-axis perpendicular to the Gd-O_w bond in agreement with the experiment. For Holmium compound, the relatively high value of the angle ζ, about 22°, will be discussed along with the computed energy spacing, and it can be explained on the basis of the small E_0 e E_1 gap (see previous chapters). Summarizing, the calculations performed here are extremely accurate in the prediction of the tilting angle between the easy axis and the axial bond, but for some derivatives deviations in the 'easy plane' are observed.

Observing the computed energy levels, at first sight a repetitive pattern appears. In the first half of the series the first excited state is about one hundred of wavenumbers, the closest one is found for the Nd derivative, 81 cm^{-1}. The second and third excited states are more than three hundreds of wavenumbers. This time the closest ones to the ground state are in the Pr complex, where four singlets are under 250 cm^{-1}. For the Gd derivative, as expected from a not orbitally-degenerate ion, the zero-field splitting is quasi negligible and all the Kramers'doublets originating from the ground atomic term lie within 1 cm^{-1}. For the second part of the series the situation is totally different: several states are separated by less than one hundred wavenumbers from the ground state. Therefore, in principle each one can influence the magnetism behaviour at low temperatures, differently from what found in the first part of the series. These considerations suggest to move from the simplest model **M2m** applied for the investigation of these compounds towards a more sophisticated one as it is **M1**. However, the comparison with the experimental data shows

$Ce(^2F_{\frac{5}{2}})$	$Pr(^3H_4)$	$Nd(^4I_4)$	$Eu(^7F_0 - {}^7F_1)$	$Gd(^8S_{\frac{7}{2}})$	$Dy(^6H_{\frac{15}{2}})$	$Ho(^5I_8)$	$Er(^4I_{\frac{15}{2}})$
0.000	0.000	0.000	0.000	0.000	0.000	0.000	0.000
0.000	111.795	0.000	95.346	0.000	0.000	8.286	0.000
109.236	145.211	81.397	339.942	0.134	17.994	24.617	40.526
109.236	235.614	81.397	355.007	0.134	17.994	45.096	40.526
706.001	424.929	309.136	728.465	0.385	128.340	102.501	86.511
706.001	491.939	309.136	733.524	0.385	128.340	169.562	86.511
	521.421	345.735	739.500	0.762	201.759	177.786	141.837
	674.801	345.735	752.899	0.762	201.759	197.527	141.837
	838.160	424.696	939.437		293.583	205.148	155.080
		424.696			293.583	211.041	155.080
					369.632	227.484	202.761
					369.632	272.630	202.761
					458.869	302.575	317.018
					458.869	310.991	317.018
					610.464	315.442	361.767
					610.464	359.746	361.767
						360.946	

Table 4.23: *Ab Initio* Computed energy ladder of the *ab initio* investigated derivatives.

that even this simplest approach provide reliable results.

By means of these computed states, crystal field parameters expressed in terms of Extended Stevens' Operator have been extracted. The 27 parameters necessary to reproduce the electronic structure in low symmetry environment were keeped fixed in order to fit the CTM curves at several temperatures. The agreement is good, as it can be observed in fig 4.24 and this confirms the validity of this approach.

Regarding the Ho compound, some clarifications should be made. The easy axis of magnetization was extracted by diagonalizing the Van Vleck susceptibility tensor. This tensor is computed in function of the temperature, hence it is very sensitive to the spacing of the energy levels. In Dy and Er derivative instead the easy axis are defined by mapping the fundamental state on the pseudospin hamiltonian because we are in presence of Kramers' ions: therefore, even if the spacing is not perfectly reproduced, the orientations of the easy axis is temperature independent. Since we have seen that the model influences more strongly the spacing of the levels than the orientation/magnitude of the main magnetic axes, the calculation of Dy and Er would show the correct orientation even in presence of an uncorrect separation between the ground and excited state. Instead for a non-Kramers' ion as Holmium, the orientation of the axes is not temperature independent, it is not an intrinsic properties of a doublet:

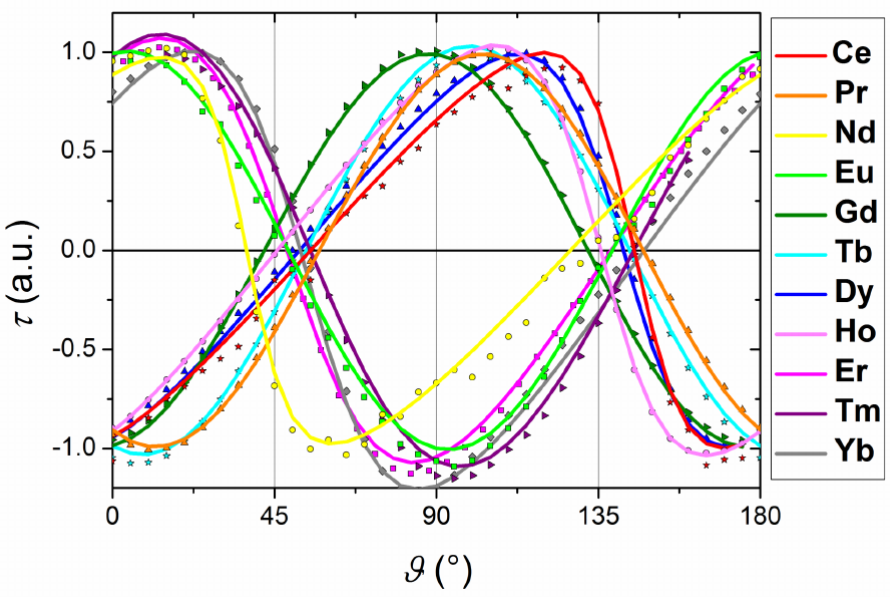

Figure 4.24: Normalized experimental (dots) and fitted (lines) data recorded by one rotation in the CTM for all Ln. The temperature was 2K for all derivatives except for Er (5K). The magnetic field was 12T for Ce and Nd, 9T for Pr and Eu, 5T for Er, 3T for Gd, Tb and Yb and 2T for Dy and Ho and 1.5T for Tm.

the uncorrect reproduction of the energy ladder significantly influences the computed easy axis.

B_k^q	$Ce(^2F_{\frac{5}{2}})$	$Pr(^3H_4)$	$Nd(^4I_4)$	$Eu(^7F_0-{}^7F_1)$	$Gd(^8S_{\frac{7}{2}})$	$Dy(^6H_{\frac{15}{2}})$	$Ho(^5I_8)$	$Er(^4I_{\frac{15}{2}})$
B_2^{-2}	$-0.40564626430493E+00$	$-0.43738573556058E+00$	$-0.10731070666214E-01$		$-.39905541847762E-04$	$-0.16791243090160E+00$	$0.58483869696695E-01$	$-0.11128709807286E+00$
B_2^{-1}	$-0.79085346240630E+00$	$0.25908049561149E+01$	$0.52041024534944E+00$		$.19652266089382E-05$	$0.20551617532061E+00$	$0.34102759234254E-02$	$0.79391995507233E+00$
B_2^0	$-0.19406610236959E+02$	$-0.60563559989926E+01$	$0.36865337422827E+01$		$-.11787555361704E-01$	$-0.14209389472602E+01$	$-0.56118339196739E+00$	$-0.11643963065350E+01$
B_2^1	$0.33899011767922E+01$	$0.13898147559060E+01$	$0.26030029303083E+00$		$.12601902638745E-03$	$0.21386240587523E+00$	$-0.70558359413436E-01$	$0.51234642660694E+00$
B_2^2	$0.48943353414377E+02$	$0.17310090626004E+02$	$-0.30954917239923E+00$		$.30308251378227E-01$	$0.39051931521116E+01$	$0.15385246378866E+01$	$0.14329421437472E+00$
B_4^{-4}	$-0.29852819728790E+00$	$-0.22742134309930E-02$	$-0.24786635150289E+00$		$-.39635126479103E-05$	$-0.20346127941318E-04$	$0.15096380099780E-03$	$-0.13499409301875E-01$
B_4^{-3}	$-0.42306408495488E+01$	$0.11727663736108E+01$	$-0.38031230140391E-01$		$-.41417256717979E-04$	$-0.34838335130880E-01$	$-0.20284871785098E-01$	$-0.18368275953249E-01$
B_4^{-2}	$-0.44439978371591E+00$	$0.18381591246329E-01$	$-0.40595776602551E-02$		$-.30810316340330E-05$	$0.21188201233893E-02$	$0.11655728445984E-02$	$0.10322400318187E-02$
B_4^{-1}	$-0.27332413315903E+01$	$0.71479570274617E+00$	$-0.91670178141707E-03$		$-.32583833360170E-04$	$-0.23948738084867E-01$	$-0.17692019658575E-01$	$-0.12657652211171E-02$
B_4^0	$-0.75617988687198E+00$	$-0.20326920267050E-01$	$-0.55988080515136E-02$		$-.40560441547812E-06$	$-0.44449015483920E-02$	$-0.19086844819842E-03$	$0.18072111683118E-03$
B_4^1	$-0.12986109548236E+00$	$0.12857252914711E-01$	$-0.88565383418994E-02$		$-.14576379048192E-05$	$0.31321919950972E-02$	$0.33478523067683E-03$	$0.26168068686982E-03$
B_4^2	$-0.42560525931507E+01$	$-0.13090210699310E-01$	$0.10054970807996E-01$		$.26694206305491E-05$	$-0.14477165946336E-01$	$0.11840567627743E-02$	$-0.79589772256166E-03$
B_4^3	$0.13592928533768E+01$	$-0.60033906619460E-01$	$-0.25837779648058E-01$		$.11008112180269E-04$	$0.98058708784598E-02$	$0.29870256075709E-02$	$0.70454328046453E-02$
B_4^4	$-0.14809826525012E+01$	$-0.10472202683829E+00$	$0.73177426838481E-01$		$-.93239940622259E-05$	$-0.71935199801003E-02$	$-0.29922346369951E-03$	$0.21462927805825E-01$
B_6^{-6}		$0.31035866167809E-02$	$-0.27718920298449E-02$		$.18526414549669E-08$	$0.24690119228288E-04$	$-0.63586879171239E-04$	$-0.98312321023020E-04$
B_6^{-5}		$0.79484796656570E-01$	$-0.89436797085235E-02$		$.26326707658526E-07$	$-0.63592423624263E-04$	$0.89391864514784E-03$	$-0.35109052110503E-03$
B_6^{-4}		$-0.15885113827582E-02$	$0.22633074911301E-01$		$-.21944156282786E-08$	$-0.28984492964501E-05$	$0.47926189654445E-04$	$0.48567880015246E-03$
B_6^{-3}		$0.26357569800039E-01$	$0.21201106975416E-02$		$.18761239619181E-07$	$-0.70152162560570E-04$	$0.46436134877464E-03$	$0.42143087495329E-03$
B_6^{-2}		$-0.20770417921753E-02$	$-0.10382832065940E-02$		$-.20390105997524E-08$	$-0.12102514405671E-04$	$0.36826862448680E-04$	$0.68229981661801E-04$
B_6^{-1}		$-0.14981267152577E-01$	$0.13855174154031E-02$		$-.82902108416859E-08$	$-0.80374902949651E-05$	$-0.21853647502087E-03$	$-0.20645511187358E-03$
B_6^0		$0.23860637764542E-02$	$-0.56254876715230E-03$		$.39211593635901E-09$	$0.22743308016064E-04$	$-0.12261543884022E-04$	$0.19702017147963E-04$
B_6^1		$0.46658674198801E-02$	$-0.32155521212135E-03$		$.12131529855292E-08$	$-0.92830101774493E-04$	$0.17321821471525E-04$	$-0.11617463651562E-03$
B_6^2		$0.96371752661645E-03$	$-0.46552444738976E-03$		$.13455953734161E-08$	$0.14634891628868E-05$	$-0.48889063309095E-04$	$0.70838073620511E-04$
B_6^3		$0.33676098491572E-02$	$0.28456689197933E-02$		$-.25180304806192E-08$	$-0.16317903518961E-03$	$-0.28171858589764E-04$	$0.18729626874773E-03$
B_6^4		$-0.32674260334400E-01$	$0.69847811646255E-02$		$-.82057735776543E-08$	$-0.38259102880509E-03$	$0.27849694441005E-03$	$-0.21433937389496E-03$
B_6^5		$-0.31093363383860E-02$	$0.36396042567042E-02$		$-.20909585138567E-07$	$0.30962361004120E-03$	$-0.24060480531877E-03$	$0.11022069922838E-02$
B_6^6		$-0.28120870740333E-02$	$-0.15222696954329E-02$		$.38263958643170E-09$	$-0.29804783725779E-04$	$-0.80258444712035E-04$	$-0.12071762993577E-03$

Table 4.24: *Ab Initio* Computed Extended Stevens'parameter for the investigated derivatives

4.3.2 Summary

The investigation by CASSCF method of the $\{Ln(DOTA)(H_2O)\}^-$ derivatives proved all the potentiality of *ab initio* methods to get insights about real mechanism behind finest effects such as the influence of the orientations of the ligands on the magnetic properties, i.e. the orientation of the easy axis of magnetization and the energy ladder.

The several models tested for DyDOTA demonstrated that the electrostatic environment in the crystal cannot be easily neglected: this approximation, even if can lead to acceptable results, has to be carefully validated by comparing the theoretical results with experiments and/or with more accurate models. More in details, the accurate modeling of the crystal electrostatic environment for DyDOTA has been necessary not only in order to reproduce the experimental data, for instance the energy ladder, but also the peculiar influence of the apical water molecule on the magnetic structure. The best model was built by embedding the $\{Dy(DOTA)(H_2O)\}^-$ complex in huge number of point charges computed by DFT with periodic boundaries, without any arbitrary assumption about the molecular cluster to include in the calculation, as in the paper by Cucinotta[61] *et al.* Indeed the **M1** was built *a priori* by a simple set of rules that can be extended in general for molecular crystals: i) only the molecules directly bonded to the lanthanides have to be treated explicitly, ii) the environment has to be reproduced by an electrostatic potential computed periodically.

Regarding the debate in literature about the influence of the bonded water molecule, the calculations confirmed the infuence of the molecule on the easy axis and the electonic structure: the switching of the main magnetic axis between two extreme positions takes place, as found by Cucinotta *et al.*,[61] however this change is gradual and not abrupt as previously suggested. It experiences many intermediate positions between the two extremes in function of the rigid rotation of the bonded water. More about this aspect, the dihedral angle formed by the plane of the water molecule and the Dy-O_w bond influences the smoothness of this modulation, along with the electrostatic potential of the environment, and hence the quantum of energy involved.

This dynamic property is modulated by the rotation of the water molecule which stabilizes/destabilizes the first excited and the ground state: their magnetic easy-axes are perpendicular to each other and therefore which one is the lowest in energy determines the orientation of the computed fundamental easy-axes: the energy separation between them and the energy involved in the rotation are therefore fundamental to reliably model the phenomenon and correctly foresee this new behaviour

which could find applications in several other fields besides the molecular magnetism, for instance, MRI and structural biology. Beeing both energies model dependent it is worth to stress again the importance of the modelization.

The electrostatic analysis performed by substituiing the water molecule with their multipolar expansion unveiled the nature of the bonding between the lanthanide and the ligand. Analyzing the energy trends, the electrostatic potential is the main driver (75%) but it is not sufficient to completely explain the theoretically observed mechanism: at least 25% of the energy involved in the rotation of the water molecule can be attributed, by exclusion, to an interaction between the MOs of the ligand and the AO localized on the lanthanide ion. In this regard, the fundamental role of the electric quadrupole moment was evidenced: such analysys can be extended to other ligands also characterized by a large quadrupole, in order to investigate the presence of the same effect in other complexes and its eventual general validity.

Finally the calculations performed on the LnDOTA series validated the proposed approach and confirmed the validity of the simplest model (**M2m**) as a good strating point to compare with the experiments. It proved to be able to discriminate between easy axis and easy plane behaviour, to reproduce the orientation with respect to the pseudo-symmetry of the molecule as showed by the angle ϵ, and, finally, to provide a reliable energy ladder between the ground and excited states. Last but not least, it evidenced the importance of a more refined modelization for complexes presenting low-lying in energy excited states (less than few tens of wavenumbers). Indeed, the application of model **M1** to Gd and Ho derivatives can be suggested as a futher development of the presented work.

Author Contribution

Matteo Briganti performed all the *ab initio* calculations. Guglielmo Fernandez Garçia performed the CAMMEL analysis on the DyDOTA derivative. Mauro Perfetti synthesized all the complexes of the LnDOTA series, performed and simulated the torque data.

Chapter 5

Heterospin systems

5.1 Introduction

The coupling of stable organic radicals with transition metals and lanthanides is a long-lasting story: the ligands employed[74] range from carbenes to semiquinonoids[178] and nitroxides. Each class has its peculiarity deriving for instance from the number of binding positions or the electronic structure. The 2,2,6,6-tetramethylpiperidine-1-oxyl (TEMPO) and the 4,4,5,5-tetramethylimidazolidine-1-oxyl-3-oxide (or Nitronyl-Nitroxides, NNit) (see figure 5.1) are two of the most widely employed radical ligands. Both these two molecules belong to the family of the nitroxide organic radicals, where the unapired electron resides in a π^* antibonding orbital localized on the NO groups. This group is able to directly coordinate the metallic centre and hence to bring the $2p$ unpaired electron directly in contact with the $3d/4f$ orbitals, offering the possibility to pursue stronger exchange couplings. Their structure can be functionalized by the attachement of different types of groups which allows the design of a large amount of structures.

The TEMPO radical is an aliphatic nitroxide and, therefore, is a better candidate to pursue stronger exchange coupling[179] due to the localized nature of the unpaired radical along a single bond. Its stability is attributed to the hyperconiugation and to the steric hyndrance of the four methyl groups situated in α respectively to the NO group which stabilize the unpaired electron and protect it from the environment.

Nitronyl-Nitroxides are stabilized due to the delocalization of the unpaired electron along the π moiety. Due to the presence of two equivalent NO groups, the unpaired electron is more delocalized then in TEMPO rad-

icals. However, the two nitroxide groups offers more than one coordination sites in order to create a wider variety of molecular architectures than the TEMPO radical. Indeed, in the history of molecular magnetism NNits are a milestone, having been employed to obtain the first purely organic ferromagnet.[180] Since then, it became one of the building blocks to synthesize magnetic materials and SMMs, as for example the $[Mn(hfac)_2NitPh]_6$ molecular wheel,[181] and SCMs as the already cited CoPhOMe[39] and the CoPyrNN.[40] This last coordination polymer will be investigated in the last chapter of the thesis.

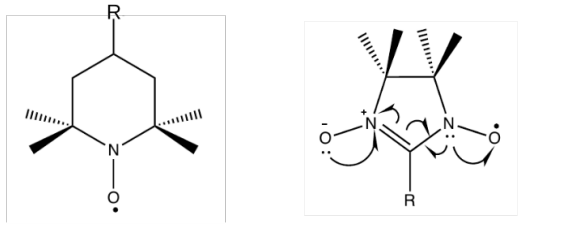

Figure 5.1: Nitronyl-nitroxide and TEMPO radicals.

In this chapter an *ab initio* computational study of heterospin complexes containing organic radicals will be presented. As already explained in the introduction, such types of compounds are intersting due to the possibility to suppress the QTM by exchange coupling and consequently increase the blocking temperature of the SMM.

Three compounds have been designed using as a ligand the TEMPO molecule functionalized with an additional phosphinic amide coordinating group (see figure 5.2). Gd, Tb and Dy derivatives were synthesized: Tb(III) and Dy(III) ions are of interest as they are good candidates for SMM behaviour, and in order to quantify the magnetic interaction between the metal ion and the TEMPO radical, the gadolinium derivative was obtained. The Tb and Dy derivatives of the series then showed an interesting feature: two different relaxation processes of the magnetization clearly visible from DC magnetometry.[182] From the huge number of SMMs characterized to date, there are several examples showing two relaxation processes. The known examples of compounds with two relaxation processes are obtained rather serendipitously. Such a behavior has been addressed to one of the following causes: (i) co-existence of two crystallographically different, either mono- or oligonuclear, molecular entities in the crystal;[183] (ii) the oligonuclear species contain two crystallographically/chemically non-equivalent metal centers.[184,185] The binuclear

lanthanide complex family, with non-equivalent metal centers, belongs to this second class.

The energy levels in these systems are very sensitive to the coordination geometry of the metal ions, with direct implication to the luminescence, the Tb(III) ion shows a green luminescence, and magnetic properties, including magnetic relaxation. The compounds showed both for Tb and Dy derivatives two different relaxation processes of the magnetization, and the inequivalence of the two Tb ions was also proved by luminescent measurement. Moreover in the synthetic design it was assumed that the ligand does not provide a sizable superexchange path connecting two lanthanide ions in order to have a SIM and an SMM inside the same molecule.

These compounds offered an opportunity to test and verify our protocol to systems where two or more more magnetic centers are interacting. *Ab initio* CASSCF calculations performed with our proposed approach supported the previous experimental assumptions and showed to give extremely useful insights to interpret and reproduce static magneti properties in $2p$-$4f$ heterospin compounds. Exchange couplings between the radical and the lanthanide have been computed, together with the single ion anisotropies for both the ions in the Dy and Tb derivatives.

Moreover, on the basis of the reliability of our approach in reproducing the magnetic static properties, then we focused on the possibility to explain also the dynamic behaviour, into the Cotton-Waller framework, of heterospin complexes. The complexes investigated were synthesized with a new heterotopic end-off compartmental ligand. This ligand selectively interact with $3d$ and $4f$ metal ions, leading to predictable heterospin complexes. In our case, one compartment is made by the Mannich-base moiety, while the other one is built by the nitronyl-nitroxide pendant arm (see fig. 5.8). The phenoxido oxygen atom acts as a bridge when two metal ions are hosted by the compartmental ligand.

Employing the compartmental ligand , three types of heterospin systems can be obtained: (a) $2p$-$4f$ complexes, with the oxophilic lanthanide ion located into the compartment formed by the phenoxido and nitroxide oxygens; (b) $2p$-$3d$ complexes, with the two compartments occupied by $3d$ metal ions; (c) $2p$-$3d$-$4f$ complexes, with the 3d metal ion hosted into the first (ONN') site and the $4f$ ion into the second one (OO'). Compounds have been sythesized belonging to each of the three classes but the magnetic measurements were performed only on the lanthanide contanining compound: the $2p$-$4f$ complex with Dysprosium and the $2p$-$3d$-$4f$ with Dy(III) and Co(II), which validates the rational synthetic strategy towards $2p$-$3d$-$4f$ complexes using the new ligand (Figure 5.8).

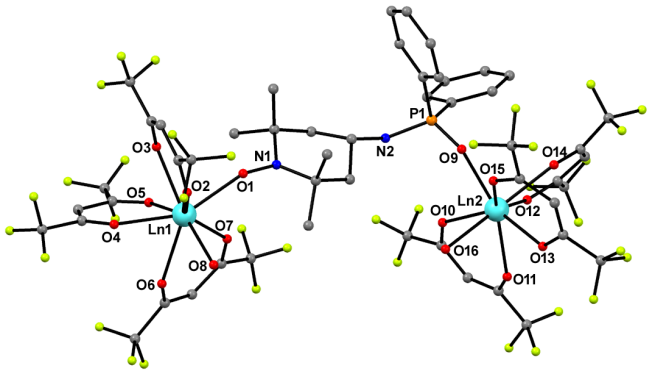

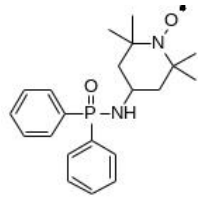

(a) dppn-TEMPO radical

Figure 5.2: Molecular structure of $[Ln_2(hfac)_6(H2O)_2(dppnTEMPO)]$ (Ln = Gd **1**, Tb **2** and Dy **3**). Hydrogen atoms were omitted for the sake of clarity.

Indeed the sythesized $2p$-$4f$ compound showed field-induced slow relaxation of the magnetization, instead, the heterotrispin one did not present any SMM feature, despite the presence of a strongly anisotropic Dy(III) and Co(II) ions. The possibility to rationalize this aspect has been the final aim of this computational investigation. Moreover this offered the possibility to test our protocol on a unique $2p$-$4f$-$3d$ compound synthesized with a new and promising approach that offers the possibility to obtain predictable heterotrispin systems by one-step reactions.

5.2 Binuclear Lanthanide Compounds Coupled with Organic Radical dppnTEMPO

5.2.1 Structure and Experimental Data

Compounds **1**, **2** and **3** are isostructural and the crystal structures consist of binuclear neutral species (Figure 5.2) in which the metal ions are bridged by the dppnTEMPO ligand. Both lanthanide ions show a distorted square antiprismatic coordination geometry; one lanthanide ion (Ln1) is coordinated by eight oxygen atoms, six arising from three hfac chelating ligands (O2-O7), one from the dppnTEMPO radical nitroxide, and one from a water molecule, Ln1-O1 bond lengths are typical for Gd, Tb and Dy coordinated to nitroxide radical, as reported elsewhere.[186] Ln-O bond lengths are slightly shorter for the dysprosium containing complex

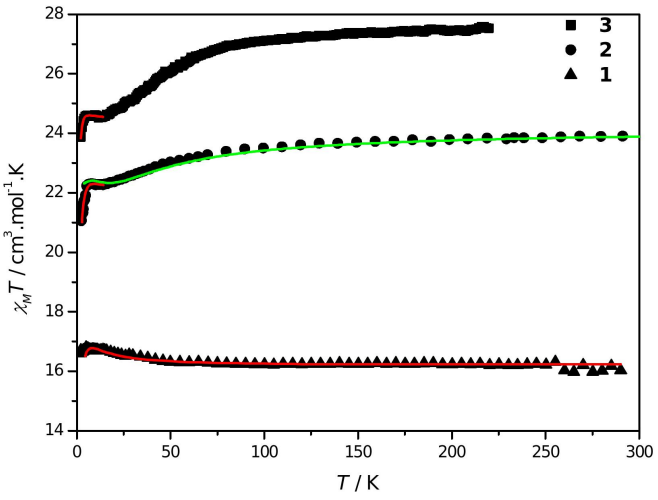

Figure 5.3: Plots of $\chi_M T$ vs. T for compounds **1-3**, measured at H = 1 kOe for **1** and 200 Oe for **2-3**. The red lines correspond to the best fits for **1-3** (vide text), while the green line represents the best simulation for **2** (vide text)

due to the smaller ionic radii when compared with Gd(III) and Tb(III) ions.

For compound **1** on lowering temperature, $\chi_M T$ increases up to 16.7 $cm^3mol^{-1}K$ around 6 K, resulting from a ferromagnetic interaction between one Gd(III) ion and the radical and then decreases slightly at lower temperatures, coming from antiferromagnetic intermolecular dipolar interactions.

The global behavior of $\chi_M T$ vs. T is quite similar for both compounds **2** and **3**. On lowering temperature down to about 15 K, $\chi_M T$ decreases, then increases slightly between 15 and 7 K, and finally drops at lower temperatures. For compounds containing lanthanide ions other than Gd(III), the depopulation of the crystal-field split M_J states occurs simultaneously with possible magnetic exchange interaction. In the high temperature range, the decrease of $\chi_M T$ values are dominated by the crystal field states, which persists below 15 K. Therefore, the slight increase below 15 K can be attributed to a ferromagnetic interaction between the radical and one lanthanide ion, as observed in compound **1** and in several other compounds.

5.2.2 Computational Method

To afford the characterization of the systems we have adopted the *divide et impera* approach: the doped method.

Indeed, we have split the systems in two model dimers whose geometry was derived from $Ln_2(hfac)_6(H_2O)_2$(dppnTEMPO) X-ray geometries. Such an approach has been previously and successfully applied on organometallic clusters.[88,178] Each model included one of the two lanthanide ions surrounded by the ligands (three hfac and one water molecule) and the radical dppnTEMPO (see figure 5.4).

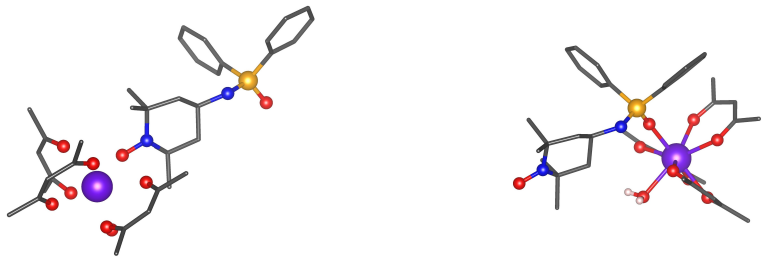

Figure 5.4: Fragment **A** (left) and **B** (right). Hydrogen and fluorine atoms are hidden for sake of clarity.

All the calculations were performed with MOLCAS 8.0 Quantum Chemistry Software Package.[101] All electron ANO-RCC[102,168,169] basis sets were employed in all the calculations(see table 5.1 for details and contraction schemes). In order to compute the isotropic magnetic coupling between the radical and the Ln ions, CASSCF calculations were performed without spin-orbit contribution for the two dimers. Such an approximation can be considered acceptable only in the case the lowest in energy spin-free multiplet contributes significantly to the fundamental spin-orbit doublet. Indeed, the values of the exchange coupling constants were computed within the Heisenberg model. For **2** and **3** the active space consisted of the seven 4*f*-orbitals of the lanthanide ion plus the antibonding π^* orbital of the nitroxide group where the unpaired electron is localized, for a total of 9 electrons in 8 active orbitals, CAS(9,8), and 10 electrons in 8 active orbitals, CAS(10,8), respectively. For **1**, the Restricted Active Space (RASSCF) approach consisting of two spaces was employed: the first one defined as CAS, i.e. with no restrictions on excitations within the chosen orbitals, while the second one as a RAS, where a maximum number of electrons is allowed to be excited in it. The CAS includes nine orbitals: the seven 4f orbitals plus the antibonding π^* orbital of the nitroxide group; the RAS includes six virtual orbitals corresponding to the

6s and 5d empty orbitals of Gd: a maximum of only two electrons were allowed in such a space. Overall the active space consisted of 10 electrons in 15 orbitals. Extension of the RAS subspaces (in this case with a maximum number of holes allowed in it) towards the occupied π orbitals of the TEMPO radical have been tested withou any improvement of the results.

Calculations were performed converging on both the ferromagnetic and antiferromagnetic states resulting from the coupling of the unpaired electron localized on the radical and the unpaired electrons on the lanthanide ions: the lowest nonuplet and septuplet for **1**; the lowest octuplet and sextuplet for **2**; and on the septuplet and quintuplet for **3**, respectively. Ferromagnetic interactions were found for model **A** with a J = 8.4 cm^{-1} for 1, a J = 11.4 cm^{-1} for compound **2** and a J = 1.7 cm^{-1} for compound **3** while a non-magnetic solution for model **B** was computed for all the ions.

Atom	Label	Primitives	Contraction
Gd	VTZP	[25s22p15d11f4g2h]	[8s7p5d3f2g1h]
Tb	VTZP	[25s22p15d11f4g2h]	[8s7p5d3f2g1h]
Dy	VTZP	[25s22p15d11f4g2h]	[8s7p5d3f2g1h]
N	VTZP	[14s9p4d3f2g]	[4s3p2d1f]
O	VTZP	[14s9p4d3f2g]	[4s3p2d1f]
C	VDZP	[14s9p4d3f2g]	[3s2p1d]
F	VDZ	[14s9p4d3f2g]	[3s2p]
H	VDZ	[8s4p3d1f]	[2s]

Table 5.1: Contractions of the ANO-RCC basis set used for all CASSCF calculations.

The energy ladder of the electronic states for Tb and Dy ions have been computed within the CASSCF/RASSI-SO method and doping the dppnTEMPO radical with an extra electron in order to turn it into a diamagnetic ligand. The computed energies are shown in Tables 5.2 and 5.3. The chosen active space consists of eight electron for Tb and nine electron for Dy in the seven $4f$-orbitals of the lanthanide ion: CAS(8,7) and CAS(9,7), respectively. Due to hardware limitations, only the seven septuplets for Tb ion and the 21 sextuplets for Dy ion were computed and included in the following spin-orbit calculation. The g-tensors were computed with the SINGLE ANISO module. Their magnetic properties were investigated within the pseudospin framework and their anisotropy axes were calculated with a pseudospin S = $\frac{1}{2}$ Despite the Tb(III) is a

non-Kramer ion, the ground spin-orbit state and the first excited one are found to be quasi-degenerate (see table 5.2) with an energy gap about 0.3 cm^{-1} for Tb1 and 0.1 cm^{-1} for Tb2. Similar composition in terms of spin-free functions were also computed for both spin states giving an Ising Doublet with a small intrinsic gap. Instead Dy(III) is a Kramers' ion due to its odd number of electrons.

5.2.3 Results and Discussion

Since Gd(III) has a ${}^8S_{\frac{7}{2}}$ ground term, with no orbital contribution, the magnetic behavior of compound **1** could be investigated on the basis of an isotropic spin Hamiltonian, considering only the magnetic coupling between one Gd(III) and radical.

$$\mathcal{H} = -J_{Heis}(\hat{S}_{Gd} \cdot \hat{S}_{rad}) \tag{5.1}$$

The solid line in figure 5.3 shows the best fit found with $g = 2.000 \pm 0.001$; $J = 2.7 \pm 0.1$ cm^{-1} and zJ' = -2x10^{-2} ± 2x10^{-4} cm^{-1}, where zJ' corresponds to the mean-field intermolecular magnetic interaction parameter. The value of the coupling parameter between Gd(III) and radical lies within the range already observed for other compounds.[179,187,188] The ferromagnetic coupling is also confirmed by the *ab initio* calculations, even if a stronger magnitude of the interaction was found, with a computed $J = 8.4$ cm^{-1}. This is in agreement with the statement by Kahn who supposed the interaction between Gd and other centers to be in the most part of the cases ferromagnetic. Indeed in the paper by Andruh *et al.*[75] it was suggested that a Ln-Cu(II) interaction should be overall antiferromagnetic for the f^{1-6} configurations, from Ce to Eu, and overall ferromagnetic for the f^{7-14} configurations, from Gd to Yb: this conclusion was deduced on the basis of the main exchange mechanism of between Gd and Cu(II). A prominent role of the ferromagnetic contribution coming by an electron transfer mechanism from a Cu(II) *3d* towards an empty orbital *5d* of Gd was suggested, and it was confirmed subsequently by CASSCF[76] and DFT[77] calculations. Indeed the usual antiferromagnetic contribution of the charge trasfer mechanism between single occupied *3d* and *4f* orbitals would not be active due to their negligible overlap. In the paper by Rajaraman however the possibility of an overall antiferromagnetic interaction was not excluded due to a small overlap between *3d* and *4f* orbitals. For a lanthanide directly bonded to an organic radical the same considerations in principle could be done: the radical is directly bonded to the lanthanide and *2p-4f* overlap could not be excluded. Moreover the necessity to include into the active space both the *6s* and *5d* orbitals to recover a value

near the experimental value, points a role of both s and d shells of the lanthanide to determine the strength of the magnetic interaction.

The overall ferromagnetic interaction between lanthanides of the second part of the series and other paramagnetic species is confirmed by subsequent CASSCF calculations with no spin-orbit contributions on the model unit Ln1-dppnTEMPO, mapping the interaction on an Heisenberg Hamiltonian, where S is the spin angular momentum operator

$$\mathcal{H} = -J_{Heis}(\hat{S}_{Ln} \cdot \hat{S}_{rad}) \tag{5.2}$$

In these cases, a J_{Heis} ferromagnetic interaction has been computed for **2** and **3** leading respectively to $J_{Tb-rad} = 11.4$ cm^{-1} and $J_{Dy-rad} = 1.7$ cm^{-1}.

However the low magnetization value of 9.5 and 12.2 μB mol^{-1} at 90 kOe, respectively for **2** and **3**, supports the presence of a significant magnetic anisotropy. In this regard, CASSCF/RASSI-SO calculations on model complexes with quenched spin moment on the radical by adding an extra electron have also been performed (see computational details). Strong local easy axes for Tb1 and Tb2 have been computed and are reported in Figure 6.4. In the case of Tb1 the easy axis points nearly orthogonal to the NO direction while for the Tb2 the easy axis is almost parallel to the PO group. This can be visualized by considering both axes directions lying parallel to the square faces of the antiprismatic coordination environment. Detailed orientations are reported in Table 5.4. The relative orientation of the two easy axes is almost orthogonal, indicating the different local coordinative environment and their orientations with respect to the crystal frame of the two Tb(III) ions.

The same procedure was employed for the calculation of single ion anisotropy of Dysprosium ions in **3**. The calculation evidenced for both ions ground Kramers' doublets well isolated in energy from the first excited state with a very strong axial character of the g-tensor, with a $g_z = 19$, near the theoretical limit of 20, as shown in tables 5.2 and 5.3. The orientation of the main magnetic axes in relation to the coordinative environment is similar to compound **2** (Figure 5.6): the axis calculated for Dy1 almost orthogonal to the N-O bond while the other one relative to Dy2 almost parallel to the P-O group (see Figure 5.6).

The results from the CASSCF/RASSI-SO calculations for **2** were employed to simulate the magnetic $\chi_M T$ vs. T data. In the Lines'model[79] the Heisenberg isotropic exchange interaction is firstly computed between isotropic spin multiplets (S=3 for Tb) and then projected on the basis of the previously computed ab initio spin-orbit states. In our model for compound **2** only the exchange coupling interaction between the lanthanide

Energy Levels	$Tb1$	$Tb2$
1	0.000	0.000
2	0.363	0.097
3	129.474	95.745
4	133.342	100.817
5	235.475	142.823
6	243.206	172.041
7	310.229	175.811
8	320.771	205.938
9	370.752	207.261
10	438.542	246.822
11	460.504	247.965
12	669.021	439.670
13	672.329	439.684

Table 5.2: Computed Energy levels at CASSCF/CASSI-SO level for both fragments of compound **2**

Energy Levels	$Dy1$	$Dy2$
1	0.000	0.000
2	203.709	117.322
3	328.026	175.102
4	392.150	217.390
5	513.136	241.914
6	606.205	311.872
7	662.829	387.395
8	859.427	569.660

Table 5.3: Computed Energy of the Kramers'doublets at CASSCF/CASSI-SO level for both fragments of compound **3**

		Value	a	b'	$c*$
$Tb1$	g_x	0.000	−0.472	−0.823	0.316
	g_y	0.000	0.847	−0.323	0.422
	g_z	17.72	−0.245	0.466	0.422
$Tb2$	g_x	0.000	−0.300	−0.644	0.704
	g_y	0.000	−0.170	−0.690	−0.704
	g_z	17.23	0.939	−0.331	0.097

Table 5.4: Compound **2**: values of the main anisotropy axes for Tb1 and Tb2 and their orientations in the crystal frame.

		Value	a	b'	$c*$
$Dy1$	g_x	0.010	0.03901	0.028602	−0.998829
	g_y	0.018	0.01907	0.999387	0.029363
	g_z	19.88	0.999057	−0.020193	0.038441
$Dy2$	g_x	0.033	−0.122201	−0.671268	0.731072
	g_y	0.056	0.947320	−0.298609	−0.115834
	g_z	19.61	0.296060	0.678404	0.672396

Table 5.5: Compound **3**: values of the main anisotropy axes for Dy1 and Dy2 and their orientations in the crystal frame.

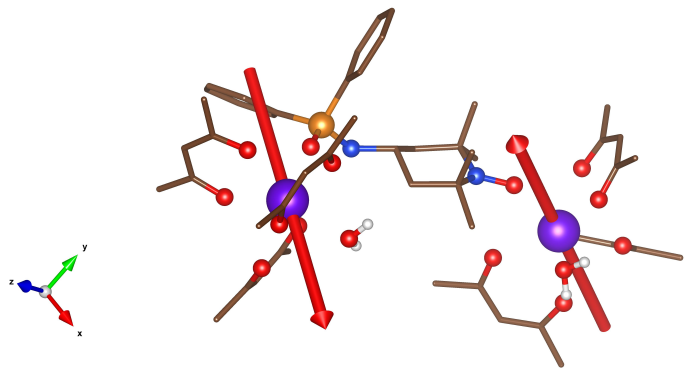

Figure 5.5: Direction of the computed easy axis for Tb1 and Tb2 ions for compound **2**. Terbium, carbon, nitrogen, oxygen and phosphorus are purple, brown, blue, red and orange respectively. Hydrogen and fluorine atoms were omitted for the sake of clarity. The crystallographic orthogonal reference is also shown.

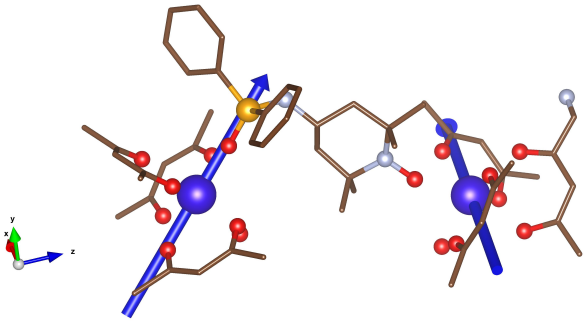

Figure 5.6: Direction of the computed easy axis for Dy1 and Dy2 ions for compound **2**. Dysprosium, carbon, nitrogen, oxygen, phosphorus are blue, brown, pale blue, red and orange, respectively. Hydrogen and fluorine atoms were omitted for the sake of clarity. The crystallographic orthogonal reference is also reported.

and the coordinated isotropic S = $\frac{1}{2}$ of the radical was taken into account, in agreement with the results of the *ab initio* calculation that showed no magnetic interactions with Tb2. The exchange interaction involved only the two lowest states in energy of the Terbium ion with the isotropic doublet of the radical. In order to reproduce the high temperature data also the single ion crystal field splitting for the two inequivalent lanthanides was included in the model within the Extended Stevens'Operator approach.[54,55] As shown in figure 5.3, below 6 K the $\chi_M T$ drop can be due, on the other hand, to intermolecular antiferromagnetic dipolar interaction between lanthanide ions. Therefore our model also considered the dipolar interactions between lanthanide ions Indeed the x-ray structure showed that in the crystal packing every Terbium atom is near another one with the same coordination environment at a distance less than 6 $\AA$. Finally the Hamiltonian employed was

$$\begin{aligned}\hat{\mathcal{H}} = & \sum_{n=Tb1,Tb2} \frac{\mu_0}{4\pi r^3}\left[\boldsymbol{\mu}_n \cdot \boldsymbol{\mu}_{n'} - \frac{3}{r^2}(\cdot\boldsymbol{\mu}_n \cdot r)(\cdot\boldsymbol{\mu}_{n'} \cdot r)\right] \\ & + \sum_{k=2,4,6}\left(\sum_{q=-k}^{k} B^q_{k(Tb1)}\hat{O}^q_{k(Tb1)} + B^q_{k(Tb2)}\hat{O}^q_{k(Tb2)}\right) + \\ & - J_{lines}\left(\hat{S}_{Tb1}\hat{S}_{rad}\right) + \mu_B g_J\left(\hat{J}_{Tb1}\cdot I + \hat{J}_{Tb2}\cdot I\right)\cdot\vec{B} + \mu_B g_e \hat{S}_{rad}\cdot\vec{B}\end{aligned} \tag{5.3}$$

where $B^q_{k(Tb1)}$ and $\hat{O}^q_{k(Tb1)}$ are the extended Stevens'parameters and operators for the two Tb ions, g_J are the g factors for the lanthanide ions and the radical's unpaired electron, $\hat{J}$ and $\hat{S}$ are the total angular and total spin momentum operators, $\vec{B}$ is the magnetic field and finally J_{lines} is the effective exchange coupling constants between magnetic centers. J_{lines} is the only fitting parameter of the simulation, because all the other terms are computed *abinitio*.

The best simulation was obtained with a ferromagnetic $J_Lines = 5.3$ cm^{-1} (green solid line in Figure 5.3). The experimental curve is well reproduced: the simulation shows the peak at about 7 K and the same slope at higher temperatures.

Within this theoretical framework of a pure Ising-type local magnetization on each Ln(III) ion in compounds **2-3**, the $\chi_M T$ vs. T data were fitted below 15 K considering $S_{eff} = 1/2$ with anisotropic g values for each lanthanide ion. Furthermore, due to the short intermolecular distances between lanthanide ions, the intermolecular dipolar interaction had to be considered between the lanthanide ions Ln1 and Ln2 of different molecules ($J_{Dipolar}$). The solid red lines in Figure 5.3 show the best fits obtained for compounds **2-3** using the MagProp routine in the DAVE software suite.[189] The parameters found for **2** are $g_{rad} = 2$ (fixed), $g_{Tb,x}$= $g_{Tb,y} = 0$ (fixed), $g_{Tb,z} = 18.6 \pm 0.1$, $J_{Ising} = (15.6 \pm 1.8)$ cm^{-1} and J_{Dip} = -(1.0 ± 0.1) cm^{-1}. The parameters found for **3** are g_{rad}= 2 (fixed), $g_{Dy,x} = g_{Dy,y} = 0$ (fixed), $g_{Dy,z} = 19.62 \pm 0.02$, $J_{Ising} = (7.8 \pm 0.6)$ cm^{-1} and J_{Dip} = -(0.61 ± 0.05) cm^{-1}. In both cases, the magnetic exchange interaction between the radical and the Ln1 ion is ferromagnetic and is higher in **2** with respect to **3** as expected from the first principles calculations. The *ab initio* computed J_{Heis} for **2** and **3** are in good agreement with experimental fit values. Moreover the exchange coupling constants are close to the ones found in other compounds. In order to compare the simulation with the fit, the relationship between the two exchange coupling constants was extrapolated matching the energy difference between the parallel and anti-parallel configurations in function of J. Considering the description of the lanthanide ion as a $S_{eff} = \frac{1}{2}$ spin within the Ising model, the obtained J_{Ising} (15.6 cm^{-1}) is lower than J ($J_{Ising} = 6J$, for **2** , where $J = 5.3$ cm^{-1}) and greater than J_{Heis} (11.4 cm^{-1}) but still of the good order. Finally, the J_{Dip} of the magnetic dipolar interaction parameters are of the right order of magnitude considering two effective half spin.

Observing the complete picture of the exchange constants obtained in table 5.6 we should discuss if the CASSCF calculations have been able

$J(cm^{-1})$	Gd	Tb	Dy
Computed	8.4	11.4	1.7
Fitted	2.7	15.6	7.8
Lines	–	5.3	–

Table 5.6: Exchange coupling constants extracted from the several models employed: the fitted on experimantal data employing the Ising model; the computed *ab initio* employing the Heisenberg model; the simulated with the Lines' model by means of POLY_ANISO software.

to reproduce the Ln-Rad exchange constants. Some considerations can be made. Firstly the order of magnitude of the exchange constants and the complexive trend are reproduced. The Tb compound presents the largest exchange interaction while for Gd and Dy J are smaller. However, only for **2** we have a very good agreement in the magnitude with the experiment. However from the experiment the lowest one is found in **1** while from CASSCF in **3**. Hence in **1** the model employed to simulate and fit the magnetic data is the same, i.e. an isotropic Heisenberg model, further improvement could derive from further increasing of the active space towards virtual orbitals beyond the $6s$ and $5d$ orbitals.

Regarding the Dy compound instead, the main problem arises from the different models employed: Ising to fit experimental data, Heisenberg to map the results from CASSCF. In the Ising model the spin can assume only two values ± 1 while in the Heisenberg Hamiltonian the spin multiplicity assumed employed is the real one of the rare earth free-ion. In order to compare the two values, eventually also with the results of the simulation by Lines'model, such an aspect have to be taken into account. Hence the CASSCF calculation is performed without taking into account Spin-Orbit coupling, only the orbital part of the magnetic interaction is evaluated in the CASSCF step of the calculation. If we assume that this difference in energy from the ferromagnetic and antiferromagnetic states is determined only by the radial part of the magnetic orbitals and that their shape is not altered by the application of the spin-orbit coupling, in order to compare the several values the energies fro CASSCF should be mapped on an Heisenberg hamiltonian where the pseudospin are employed, i.e $\tilde{S_{Dy,Tb}} = \frac{1}{2}$. This assumption, however, is valid only if, after the spin-orbit calculation, the ground spin-orbit state is a well isolated pseudo-doublet or Kramers'doublet as in the cases of compounds **2** and **3**, respectively. Applying this approximation, the computed J for Tb and

Dy becomes, respectively, 39.9 and 5.1 cm^{-1}, with a significative improvement of the agreement with the fitted data for **3** but not for **2**. From these considerations we can conclude therefore that for Dy the mapping of the CASSCF states on an Heisenberg pseudospin hamiltonian seems to provide very reliable results, while for the Tb compound an Heisenberg hamiltonian with the real value of the spin appears more justified.

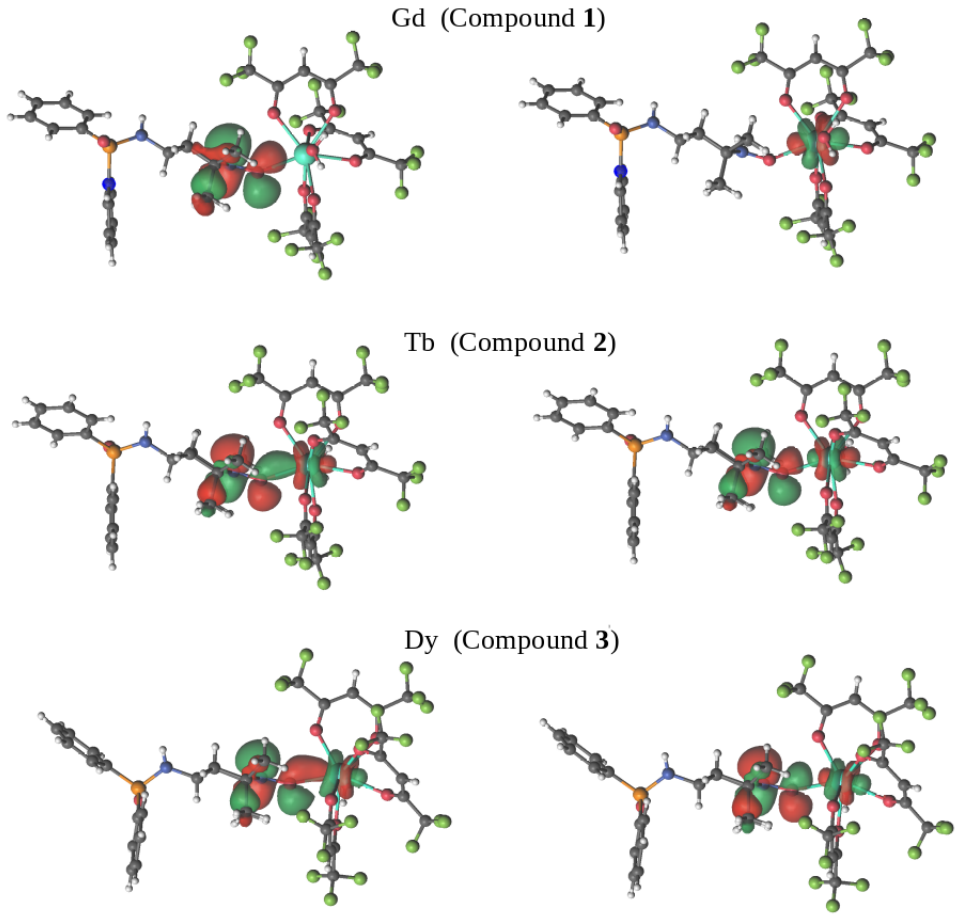

Figure 5.7: Magnetic orbitals involving the radical $\pi*$ orbital and f_{z^3} metal orbital. The isovalue level is set to 0.02. For compounds **2** and **3** bonding (left) and anti-bonding (right) interaction between the $\pi*$ and f_{z^3} orbitals are visible.

In order to find a qualitative rationalization of the ferromagnetic isotropic exchange coupling constants obtained for isostructural **1**, **2** and **3**, we have also analyzed the magnetic orbitals involving the radical π^* orbital and f

metal orbitals. Unexpectedly, only one f orbital of the metal ions interacts considerably with the π^* orbital, the f_0 orbital in the spherical basis. This is more evident for **2** and **3** where an increased overlap between the two orbitals is observed in the same order (see Figure 5). Indeed, a bonding and antibonding interaction between the two orbitals is observed as result of an effective energy matching. Moreover, it can be also evidenced that a smaller overlap between the two magnetic orbitals is observed for **2** than **3**. Indeed, due to a larger difference in Ln1-O1-N1, 143.6°vs. 156.7°, and a slightly shorter Ln1-O1 distance, 2.32 $\AA$ vs. 2.28 $\AA$, the π^* orbital in **3** can interact via an effective π-like interaction with f_0. On the other hand, a more ferromagnetic exchange is expected for **2** in virtue of a smaller σ-like overlap given by smaller Ln1-O1-N1 angle and larger Ln1-O1 distance. A different scenario is present for **1**. In such a case, the π^* and f_{z^3} are well localized suggesting a less effective interaction (longest Ln1-O1, 2.33 $\AA$ and smaller Ln1-O1-N1 angle, 141.7°). Indeed, in such a geometrical arrangement, the π^* points to the f_0 nodal plane leading to a quasi-orthogonal situation. Finally we verified the possible presence of other exchange mechanisms in addition to the direct exchange mechanism by analyzing the composition of computed natural orbitals for the three compounds. From such calculation, it came out that the Ln(III) f orbitals are completely localized while the π^* are very slightly delocalized on Ln(III) $5d$ and $6s$ orbitals in all the systems. Such findings support that the direct mechanism is the driving exchange interaction with respect to the charge transfer one as observed for Cu(II)-Ln(III).[77]

Such a qualitative analysis points out that in the case of the interaction of NO radical it could be possible to selectively modulate the magnitude of the exchange interaction by choosing the Ln1 ion and by acting on geometrical parameters as Ln1-O1-N1 angle. This result suggests a closer resemblance of the lanthanides ions with transition metals than expected in regards of their interactions with nitroxides radicals.

5.3 *2p-3d* and *2p-3d-4f* Chimeric compounds

5.3.1 Structures

The Dy(III) ion in **1** (Figure 5.8) has a coordination number of eight, with a bicapped trigonal prismatic geometry (six oxygen atoms from the three hfac$^-$ ligands, one from the nitroxide group, and one from phenoxido oxygen atom), with bond lengths ranging between 2.249(4) and 2.432(4) $\mathring{A}$. One nitrogen atom is protonated because the organic molecule acts as a ligand in the zwitterionic form. In compound **2** the end-off compartmental ligand coordinates selectively the two metal ions, being bridged-coordinated by an oxygen atom from the phenoxido group and by another one arising from one of the hfac$^-$ ligands coordinated to the Dy(III) ion. Dy(III) is eight-coordinated by three hfac$^-$ ligands (one out of the six oxygen atoms acts as a bridge), one nitroxide oxygen atom, and the bridging phenoxido oxygen atom, showing a dodecahedral geometry (bond distances range between 2.322(6) and 2.412(5) $\mathring{A}$). The intramolecular distance Co-Dy between the metal ions is 3.732 $\mathring{A}$. Cobalt ion is hexacoordinated by the two nitrogen atoms from the Mannich moiety of the ligand, by two oxygen atoms from the chelating hfac$^-$ ligand, an oxygen atom from the phenoxido bridge and the sixth one from the bridging hfac$^-$ ligand.

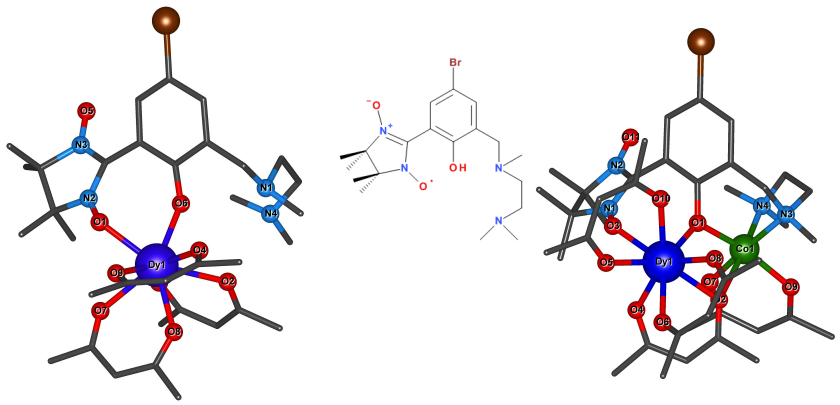

Figure 5.8: Molecular structures for **1** (left), **2** (right) and the compartmental ligand sythesized (centre). Dysprosium, cobalt, oxygen, nitrogen, bromine and carbon are blue, green, red, pale blue, brown and grey, respectively. Hydrogen and fluorine atoms are not shown for sake of clarity

5.3.2 Computational approach

All the calculations were performed with MOLCAS 8.0 Quantum Chemistry Software Package.[101] All electron ANO-RCC[102,168,169] basis sets were employed in all the calculations(see table 5.7 for details and contraction schemes). The divide et impera approach was adopted. For compound **1**,

Atom	Label	Primitives	Contraction
Dy	VTZP	[25s22p15d11f4g2h]	[8s7p5d3f2g1h]
Co	VTZP	[21s15p10d6f4g2h]	[6s5p3d2f1g]
La	VDZ	[24s21p15d5f3g2h]	[7s6p4d2f]
Zn	VDZ	[21s15p10d6f4g2h]	[5s4p2d1f]
Br	VDZ	[20s17p11d4f2g]	[5s4p2d1f]
N	VTZP	[14s9p4d3f2g]	[4s3p2d1f]
O	VTZP	[14s9p4d3f2g]	[4s3p2d1f]
C	VDZP	[14s9p4d3f2g]	[3s2p1d]
F	VDZ	[14s9p4d3f2g]	[3s2p]
H	VDZ	[8s4p3d1f]	[2s]

Table 5.7: Contractions of the ANO-RCC basis set used for all CASSCF calculations.

the geometries resolved by x-ray diffraction were employed without further modifications and optimizations. For compound **2**, x-ray structures were employed modeling -CF_3 and CH_3 groups by hydrogens atoms to reduce the number of primitive functions. No further optimization was carried on. To verify the adopted structural approximation on **2**, we have also performed the CASSCF/CASSI-SO calculations on 1 substituting the -CF_3 and CH_3 with hydrogens atoms, **1***.

The energy ladder of the electronic states for Dy(III) and Co(III) ions have been computed within the CASSCF/CASSI-SO method and doping the radical with an extra electron in order to turn it into a diamagnetic ligand. The single ion anisotropies of the two metal ions in **2** have also been computed on the individual center by diamagnetic substitution. The chosen active space for Dy(III) consists of nine electrons in the seven 4f-orbitals of the lanthanide ion: CAS (9,7). Due to hardware limitations, only the 21 sextuplets were computed and included in the following spin-orbit calculation. The chosen active space for CoIII consists of 7 electrons in the seven 3d-orbitals of the metal ion: CAS (7,5). The 10 quadruplets and the 40 doublets were computed and included in the following spin-orbit calculation. No perturbative method in order to recover part of the

dynamical correlation was performed, due to memory limitation.

The g-tensors were computed with the SINGLE_ANISO module. Both are Kramers' ion due to their odd number of electrons. Their magnetic anisotropy was investigated within the pseudospin framework and their anisotropy axes were calculated with a pseudospin $S = \frac{1}{2}$.

The energy ladder and magnetic anisotropy computed for **1**, **1***, and **2** have been reported in Table 5.8 and Tables 5.9, respectively. The small differences computed between **1** and **1*** justify the reliability of the adopted structural simplification. Significant deviations have been computed only for energy ladder values from the second excited state ahead, that is with small affection of the magnetic properties, at least at low temperature and for the single ion anisotropy.

In order to compute the isotropic magnetic coupling between the radical and the metal ions, CASSCF calculations were performed without spin-orbit contribution for the two compounds. In compound **2**, the exchange couplings between the metal ions and the radical were computed substituting them in turn by a diamagnetic equivalent ion: La(III) for Dy(III) and Zn(II) for Co(II). For the Dy(III)-nitronyl-nitroxide radical (NNit) interactions in **1** and **2**, the chosen active space consisted of nine electrons in the seven 4f-orbitals of the lanthanide ion and the unpaired electron in the π^* orbital of the O_2-N_2-C_π-N_1-O_1 system on the radical, CAS (10,8). For the Cobalt-Radical interaction in **2**, the active space consisted of the five 3d orbitals and the π^* molecular orbital of the radical, CAS (8,6). Finally in order to compute the Co-Dy interaction the GASSCF approach was employed: the radical was not doped but its π^* orbitals was let inactive. A maximum of two excitations were allowed from the seven $4f$ orbitals of the lanthanides to the five $3d$ orbitals of the Cobalt: by means of this method it was possible to converge to the lowest decuplet and octuplet in energy.

Calculations were performed converging on both the ferromagnetic and antiferromagnetic states resulting from the coupling of the unpaired electron localized on the radical and the unpaired electrons on the lanthanide ions: the lowest septuplet and quintuplet state for the interaction Dy(III)-NNit; the lowest quintuplet and triplet for the exchange Co(II)-NNit; the lowest . The values of the exchange coupling constants were computed within the Heisenberg model without spin-orbit coupling:

$$J_{Heis} = -\frac{E_{HS} - E_{LS}}{S_{HS}} \tag{5.4}$$

This approximation is acceptable when the spin-orbit coupling doesn't drastically affect the orbital shape and the difference between the energy

barycenter of the two spin states. The validity of this approximation will be discussed in the following section.

The $\chi_M T$ curves were simulated by means of the POLY_ANISO software with the Lines' model (see Table 5.11 and 5.12). In the Lines model the Heisenberg isotropic exchange interaction is firstly computed between isotropic spin multiplets (S = 5/2 for Dy and S = 3/2 for Co) and then projected on the basis of the previously computed spin-orbit states. In our models, for compound **1** only the exchange coupling interaction between the lanthanide and the coordinated isotropic S = $\frac{1}{2}$ of the radical was taken into account, while for compound **2** the three exchange coupling interactions between the lanthanide, the cobalt ion and the radical were considered, in agreement with the results of the ab initio calculation. In compound **1**, the energy of the first excited doublet was shifted 80 cm^{-1} upward. The exchange interaction involved only the six lowest states in energy of the lanthanide ion, the four lowest of the Cobalt ion and the isotropic doublet of the radical. In order to reproduce the high temperature data also the single ion crystal field splitting for the two inequivalent lanthanides was included in the model. In this Hamiltonian, the exchange coupling constant J_{Lines} is the only parameter of the methodology, because all the information about crystal field splitting and magnetic anisotropy are computed *ab initio*.

5.3.3 Static Magnetic Properties

The magnetic properties of compounds **1** and **2** were investigated in the temperature range 2-300 K. The results of the DC measurements are shown in the form of $\chi_M T$ vs T plots in Figure 5.9. The room temperature values of the $\chi_M T$ product are 14.4 and 17.5 $cm^3mol^{-1}K$ for compounds 1 and 2, respectively. The found $\chi_M T$ values are very close to the non-interacting spin carriers (14.5 $cm^3mol^{-1}K$) for 1, and slightly higher for 2 due to the orbital contribution of the magnetic moment of the Co(II) ion (17.5 $cm^3mol^{-1}K$ vs. the theoretical value of 16.4 $cm^3mol^{-1}K$, neglecting the orbital contribution for Co).

For the mononuclear Dy(III) complex **1**, on lowering the temperature, $\chi_M T$ decreases continuously to 13.2 $cm^3mol^{-1}K$ at 45 K, then increases slightly up to 13.3 $cm^3mol^{-1}K$ at 14 K and, finally, goes down to 11.2 $cm^3mol^{-1}K$ at 2 K. The high temperature decrease corresponds to the intrinsic magnetism of the Dy(III) ion with the depopulation of the M_J sublevels of the ${}^6H_{\frac{15}{2}}$ state. On the contrary, the increase is due to the ferromagnetic interaction between the Dy(III) ion and the radical, as confirmed by the *ab initio* calculations. Indeed, a ferromagnetic interaction

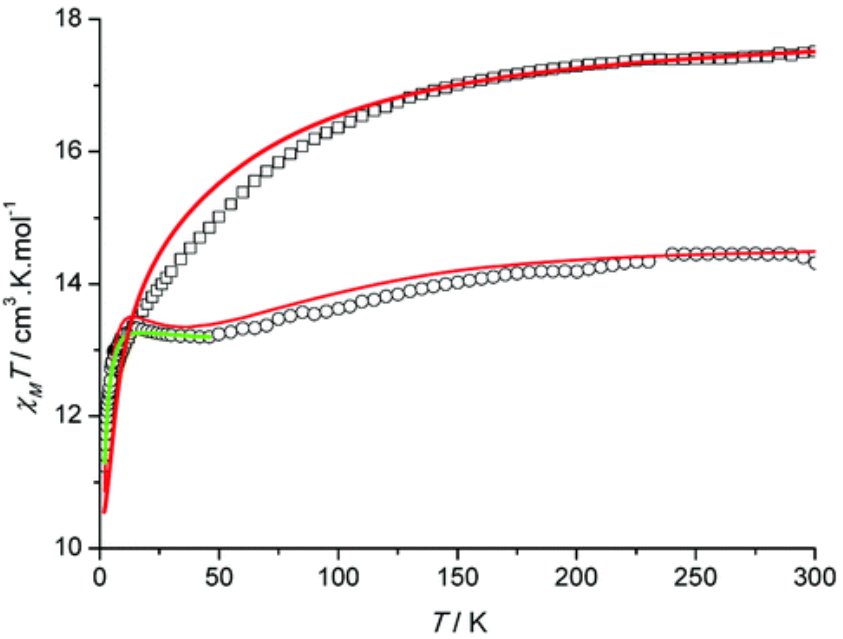

Figure 5.9: Plots of $\chi_M T$ vs. T for compounds **1** (open circle) and **2** (open squares), measured at H = 1 kOe. The green line corresponds to the best fit for 1 (vide text). The red lines correspond to the best simulations (vide text)

between the lanthanide and the radical (J = 2.4 cm^{-1}) was computed by CASSCF method with no spin-orbit contributions (SOC),[8] within the Heisenberg model $\hat{H} = -J(S_{Dy} \cdot S_{Rad})$, where $S_{Dy} = \frac{5}{2}$ and $S_{Rad} = \frac{1}{2}$.

The single ion anisotropy and the energy levels of the Dy(III) ion were obtained with the CASSCF/CASSI-SO method. The fundamental Kramers' doublet shows a strong easy-axis anisotropy, $g_z = 19.2$, while the first excited state is found well separated at 112 cm^{-1} higher in energy (Tables 5.8 and 5.9). Using the computed magnetic parameters, the $\chi_M T$ curve was simulated within the Lines' model (red lines in Figure 5.9).[9] As already explained, this is an effective exchange coupling model which allows to reproduce the magnetic exchange properties of strongly anisotropic ions. In order to simulate the curve, a ferromagnetic Dy-Rad exchange coupling $J_{Lines} = 8.5$ cm^{-1} (with an effective $S_{Dy,eff} = \frac{1}{2}$) was employed, in fairly agreement with the computed one. The simulated curve reproduces very well the experimental one, showing the peak around 14 K. Furthermore, from the CASSCF/CASSI-SO results, the $\chi_M T$ vs T data of **1** were fitted below 45 K considering $S_{eff} = \frac{1}{2}$ with anisotropic

g values for the Dy(III) ion. The solid green line in Figure 5.9 shows the best fit using the MagProp routine in the DAVE software suite,[10] with g_{rad} = 2 (fixed), $g_{Dy,x} = g_{Dy,y}$ = 0 (fixed), $g_{Dy,z}$ = 20.1 ± 0.1 and J = 7.9 ± 0.2 cm^{-1}, which is in good agreement with the magnetic exchange coupling used for the simulation.

With respect to the heterobimetallic complex **2**, upon cooling temperature, $\chi_M T$ decreases continuously down to 11.4 $cm^3mol^{-1}K$ at about 2 K. Since the depopulation of the crystal-field M_J sublevels occurs simultaneously with possible magnetic exchange interaction and magnetic anisotropy effects, it is very difficult to interpret, even qualitatively, the magnetic behavior of compound **2**.

However, *ab initio* calculations have given useful insights. The calculations and the following simulations were performed with the same procedure employed for compound **1**. The organic radical interacts ferromagnetically both with the Dy(III) and the Co(II) ions. Employing the Heisenberg spin Hamiltonian

$$\hat{\mathcal{H}} = -J_1(\hat{S}_{Dy} \cdot \hat{S}_{Rad}) - J_2(\hat{S}_{Co} \cdot \hat{S}_{Rad}) - J_3(\hat{S}_{Dy} \cdot \hat{S}_{Co}) \qquad (5.5)$$

with $S_{Dy} = \frac{5}{2}$, $S_{Co} = 2$, and $S_{Rad} = \frac{1}{2}$, J_1 = 0.78 cm^{-1}, J_2 = 0.12 cm^{-1} and J_3 = -0.35 cm^{-1} were found at the CASSCF level.

The reduction of J_1 passing from **1** to **2** can be explained on the less efficient overlap between the radical π*(NO) orbital and the dysprosium f orbitals: indeed, in 1 the π*(NO) orbital interacts via π interaction with an f_{z^3}-like orbital while in **2** it interacts more efficiently with an $f_{x(x^2-3y^2)}$-like orbital via π interaction. The variation of the Dy-O_2-N_2-C_π dihedral angle from 75.9°to 61.7°is claimed as the reason of the increase of the anti-ferromagnetic contributions (see Figure 5.11).

Regarding the single ion properties, Dy(III) and Co(II) ions present strong easy axis anisotropy of their own ground Kramers' doublets, with g_z factors of 19.8 and 6.7 respectively (Table 5.10). The first excited doublet of the Dy(III) ion is at 140 cm^{-1} while the one of the Co(II) ion at 132 cm^{-1} (Table 5.8). The computation of single ion anisotropies allowed the simulation of the $\chi_M T$ data still within the Lines' model. In order to reproduce the shape of the curve, an antiferromagnetic interaction between the lanthanide and the transition metal ions is needed to be imposed. The best simulation set of values was obtained with J_{Lin1} = 0.9 cm^{-1}, J_{Lin2} = 0.1 cm^{-1}, J_{Lin3} = -2.0 cm^{-1} in very good agreement with the computed values regarding the magnitude and the sign.

Moreover if we apply the pseudospin Heisenberg hamiltonian as proposed in the previous section, we obtain the following values: J_1 = 2.7

Energy Levels	**1**	**1∗**	**2**	
Energy Levels	Dy	Dy	Dy	Co
1	0.000	0.000	0.000	0.000
2	112.531	98.170	140.797	132.124
3	215.490	161.035	178.363	1096.691
4	285.629	178.859	229.729	1355.810
5	321.419	224.317	275.502	1533.178
6	354.075	256.749	343.242	1671.687
7	378.896	277.452	429.786	
8	556.928	467.884	562.921	

Table 5.8: Computed Energy of the Kramers'doublets at CASSCF/CASSI-SO level for **1**, **1*** and **2**

		Value	a	b'	$c*$
$Dy(\mathbf{1})$	g_x	0.055	0.623422	0.0778704	0.070468
	g_y	0.116	−0.678844	0.0583780	−0.445390
	g_z	19.23	−0.387965	0.229829	0.892559
$Dy(\mathbf{1}*)$	g_x	0.082	0.630194	0.772287	0.080178
	g_y	0.162	−0.685277	0.601779	−0.410192
	g_z	19.11	−0.365036	0.203556	0.908468

Table 5.9: Compound **1**: values of the main anisotropy axes for Dy (model 1 and model 1*) and their orientations in the crystal frame.

cm^{-1}, J_2 = 0.24 cm^{-1} and J_3 = -1.57 cm^{-1}. Hence the shape of the simulated curve is not very influenced by the values of J_{Lin1} and J_{Lin2}, but it is very dependent from the magnitude of the Co-Dy interaction, the employment of these new values to simulate the curve shows again an excellent agreement.

5.3.4 Dynamic Magnetic Properties

The dynamic magnetic properties were investigated by AC magnetic susceptibility measurements. Compound **1** clearly exhibits slow relaxation of magnetization, with frequency dependence for both in-phase (χ') and out-of-phase (χ'') susceptibilities under H = 0 Oe static magnetic field. The increase at low temperatures both for the in-phase and out-of-phase parts is an indication of the occurrence of quantum tunneling of the magnetiza-

		Value	a	b'	$c*$
Dy	g_x	0.025	−0.005575	0.616216	0.787557
	g_y	0.044	−0.120925	0.781374	−0.612235
	g_z	19.8	−0.992646	−0.098648	0.070160
Co	g_x	1.947	0.803778	0.487388	−0.341164
	g_y	3.704	−0.238447	0.789300	0.565817
	g_z	6.688	0.545053	−0.373442	0.750638

Table 5.10: Compound **2**: values of the main anisotropy axes for Dy and Co and their orientations in the crystal frame.

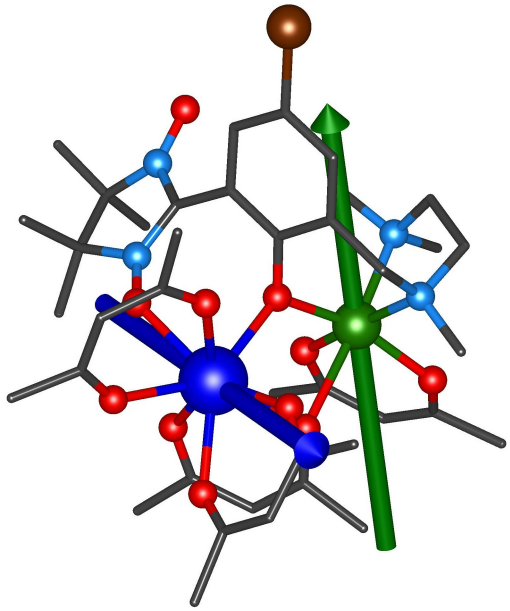

Figure 5.10: Orientations of the magnetic easy axes for **2**. Dysprosium, cobalt, oxygen, nitrogen, bromine and carbon are blue, green, red, pale blue, brown and grey, respectively. Hydrogen and fluorine atoms are not shown for sake of clarity.

tion (QTM). It is well known that for SMMs and SIMs, QTM occurring at resonance fields, mainly in zero field, can be hampered by an energy barrier caused by a nonzero external field. Therefore, the ac susceptibilities were also measured under a static magnetic field, which shifted the

frequency dependence curves to higher temperatures. For applied field H = 1 kOe, compound **1** exhibits frequency-dependent maxima for both in-phase and out-of-phase susceptibilities.

Isothermal AC susceptibility measurements were also performed while varying the AC frequency at different temperatures under 1 kOe applied magnetic fiel. These data were fitted by a generalized Debye model[134] to extract the relaxation times τ and to obtain the Arrhenius plot. The fit results gave an energy barrier of $\Delta E/k_B = 23.5 \pm 0.2$K and a pre-exponential factor $\tau_0 = 9.4 \pm 0.5 \cdot 10^{-8}$s, supporting the presence of a SMM behavior.

Such results are in agreement with the *ab initio* computed transition probabilities between the exchange states (Figure 5.12). Compound **1** has an even number of unpaired electrons and therefore a tunneling splitting, Δ_{tunn}, is expected also in zero field. The computed Δ_{tunn} is of the order of $\sim 10^{-2}$ cm^{-1} and $\sim 10^{-2}$ cm^{-1} for the ground and the first excited pseudo-doublets states (see Table 5.11), respectively. The magnitude of the two Δ_{tunn} is large and it would support the presence of strong active QTM between the pseudo-doublets, above all for the first-excited one. However, the pseudo-doublets are the result of the strong exchange coupling (J_{Lines} = 8.5 cm^{-1}) between DyIII and the radical spins, limiting the effective rate of QTM. Therefore, the first excited pseudo-doublet being at 20 cm^{-1} from the ground state and considering that an effective barrier of 16 cm^{-1} was experimentally found, we can conclude that the whole magnetic behavior of **1** is given by a balance between the exchange coupling driven interaction and the intrinsic tunneling splitting one, where the former is favored. This result is also in agreement with a recent paper[86] showing how the SMM behavior is influenced by the correspondence between large Δ_{tunn} and a relatively strong J.

In contrast with compound **1**, no frequency dependence was evidenced for the heterobimetallic complex **2** under H = 0 Oe static magnetic field, and only a very weak one was observed when applying a non-zero magnetic field. Even in this case, *ab initio* calculations are in agreement with the experimental findings. Indeed, the computed energy exchange spectrum (see Figure 5.13) presents four Kramers' doublets in the low lying energy frame (10 cm^{-1}), making several relaxation paths accessible at very low temperatures. Moreover, the QTM is, even in this case, significant due the relatively large transversal g-factors of the ground and first Kramers' doublets (see Table 5.12). Last but not least, the computed easy axis for Dy(III) and Co(II) ions are almost orthogonal to each other (they form an angle of 63°) (see Figure 5.10): in the former case the easy axis is along

Energy(cm^{-1})	$\Delta_{tunn}(cm^{-1})$	g_x	g_y	g_z
0.02750188	0.055	0	0	21.225508713
20.35845105	0.228	0	0	17.225626521

Table 5.11: Compound **1**: energy and values of the main anisotropy axes of ground and first excited exchange doublets computed within POLY_ANISO software.

the direction individuated by the Dy-O_{hfac} bond almost in opposition to the Dy-O_{Rad} one; in the latter, the easy axis points to one of the two NNO faces of the CoII octahedron. Such a situation, i.e. lowering the axial character of the resulting exchange states, has been recently claimed as a reason of the relaxation barrier decrease.[190,191]

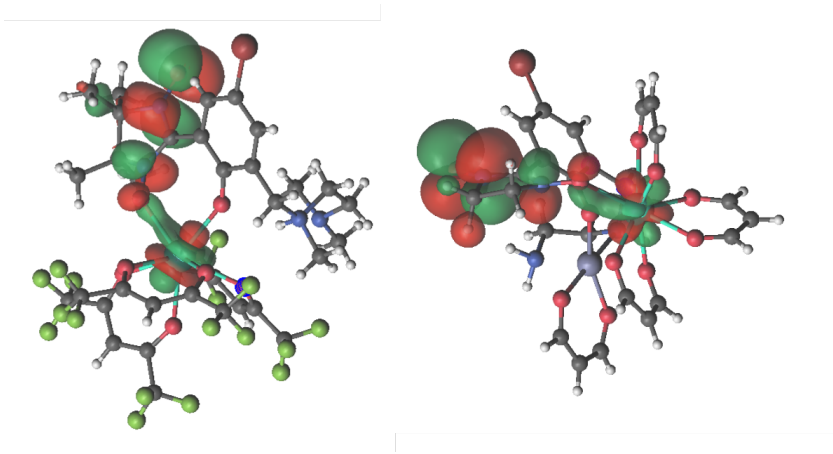

Figure 5.11: In-phase $\pi*$(NO)-f(Dy) magnetic orbitals in compounds **1** (left) and **2** (right).

5.4 Summary

The mandatory synergic interplay between the computational and experimental approaches needed for a successful characterization of such complex systems was clearly evidenced. The fitting model applied was justified and suggested by the *ab initio* calculations. The comparison between the different mapping of the spin states allowed to conclude that, at least for Karmers'ions, the pseudospin approach is justified allowing a direct

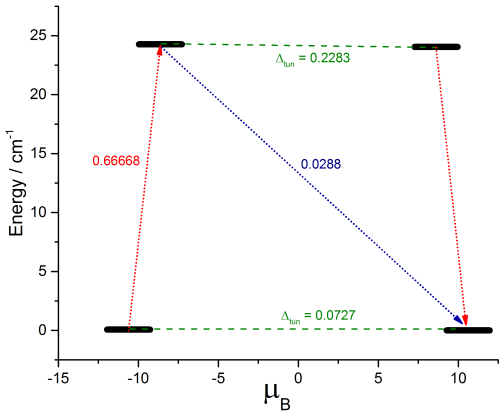

Figure 5.12: Low lying exchange states and transition moments for **1**. The thick black horizontal lines indicate the Kramers' doublets as a function of the projection of the magnetic moment on the chosen quantisation axis (the one of the ground multiplet). The dotted arrows show the possible pathways of different Orbach processes. The dashed green lines represent the presence of quantum tunnelling between the connecting states. The numbers reported for each arrow are the mean absolute value for the corresponding matrix element of the transition magnetic moment.

Energy(cm^{-1})	g_x	g_y	g_z
0	0.023512787	0.026142566	18.701640695
2.162	0.029051134	0.030623601	14.798816948
6.768	0.007785101	0.008092576	25.575389258
9.067	0.000881785	0.011931634	21.616072267

Table 5.12: Compound **2**: energy and values of the main anisotropy axes of low lying exchange doublets within POLY_ANISO software.

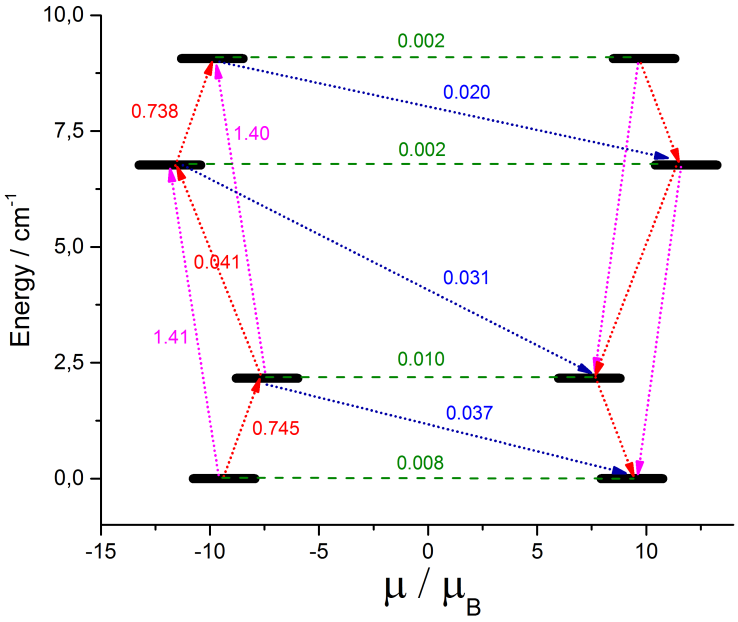

Figure 5.13: Low lying exchange states and transition moments for **2**. See Figure 5.12 for the legend.

comparison between the simulation and the *ab initio* computed magnetic exchange constants

More in detail, regarding the binuclear lanthanide compounds, the *ab initio* calculations showed to reproduce the 2*p*-4*f* magnetic coupling and the inequivalence of the magnetic centers inside the molecule in order to rationalize the susceptibility measurements. Also here the importance of the crystal environament was pointed out: the intra-molecule interaction between magnetic centers inside the crystal revealed necessary in order to simulate magnetic data.

The magnetic properties in 2*p*-4*f* and 2*p*-3*d*-4*f* systems have been successfully rationalized by state-of-art *ab initio* calculations. The minimal extension of the active space proves to be able to reproduce the sign and the magnitude of the exchange couping interaction between magnetic centers and the 3*d*-4*f* interaction was estimated by means of CASSCF calculations.

The lack of SMM behaviour for the heterotrispin compound was rationalized by means of *ab initio* computed transition moment. The re-

sults presented herein for **1** and **2** are perfectly in agreement with what reported recently: in order to improve the SMM behavior coupling two strongly anisotropic ions, the two easy axis should be almost parallel or one of the spin unit at least isotropic. In this regards, the improvement of magnetic properties of the $2p$-$3d$-$4f$ complexes could be achieved by tuning the stereochemistry of the Ln(III) ions (for instance, the hexafluoroacetylacetonato ligands coordinated to Ln(III) ions could be replaced by different fluoro-beta-diketonato ligands) and by using the isotropic and size-comparable Mn(II) ion. Moreover, the $2p$-$4f$ exchange coupling could be enhanced engineering the dihedral Dy-O_2-N_2-C_π angle.

The results showed that the exchange coupling constant between the paramagnetic centre inside the hehterospin complex can be modulated by variation of the coordination geometry around the transition metals: this way is promising because new other dissymmetric compartmental ligands can be easily synthesized by varying the amines employed in the Mannich reaction Chiral ligands and, consequently, chiral heterospin complexes can be obtained as well, when chiral amines are chosen. This would add functionalities that can be further investigated.

Author Contribution

Samira G. Reis and Sergiu Calancea synthesized the Ln_2dppnTEMPO derivatives and performed the X-ray diffraction measurement. Guillerme Guedes solved the X-ray structures. Stephane Soriano performed the AC and DC measurements and fitted the magnetic data.

Andrei Patrascu and Sergiu Calancea synthesized the complexes employing the compartmental ligand, performed X-ray measurement, solved X-ray structures. Stephane Soriano performed the AC and DC measurements and fitted the magnetic data.

Matteo Briganti performed all the *ab initio* calculations.

Chapter 6

The CoPyrNN Single Chain Magnet

6.1 Introduction

The polycyclic aromatic hydrocarbon (PAH) substituted nitronylnitr- oxide-2-(1'-pyrenyl)-4,4,5,5-tetramethyl-4,5-dihydro-1H-imidazole- 3-oxide-1-oxyl (PyrNN organic radical) is incorporated into a $[Co(hfac)_2PyrNN]_n$ helical chain (hfac = hexafluroracetylacetonate). The coordination polymer has a strong antiferromagnetic exchange interaction between the Co(II) and the radical units and presents Single Chain Magnet (SCM) behaviour. A record blocking temperature of 14 K is usually attributed to the rigidity of the structure due to the large pyrenil unit which isolate each chain, preventing intrachain interaction and 3D ordering.[40,192]

The structure is shown in figure 6.1. The chain crystallizes in a $p2_1/c$ space group. The unit cell is monoclinic and the cell parameters are reported in table 6.1. The unit cell contains two chains each formed by two cobalt ions and two organic radicals. Inside the unit cell both chains are generated by only one cristallographic unit of cobalt ion bonded to two $hfac^-$ molecules and a PyrNN radical, the $[Co(hfac)_2PyrNN]$ unit. The cobalt-cobalt intrachain distance is 7.48 $\AA$ and the shortest interchain distance between cobalt(II) ions is a relatively large 11.15 $\AA$. However, the symmetry generated structures give rise to two inequivalent Cobalt-radical bonds, characterized by differents lengths, angles and dihedrals. Hence this structure can suggest two slightly different exchange parameters and that the observed one is only an average between two constants. The volume between the chains is occupied by disordered solvent, n-heptane and

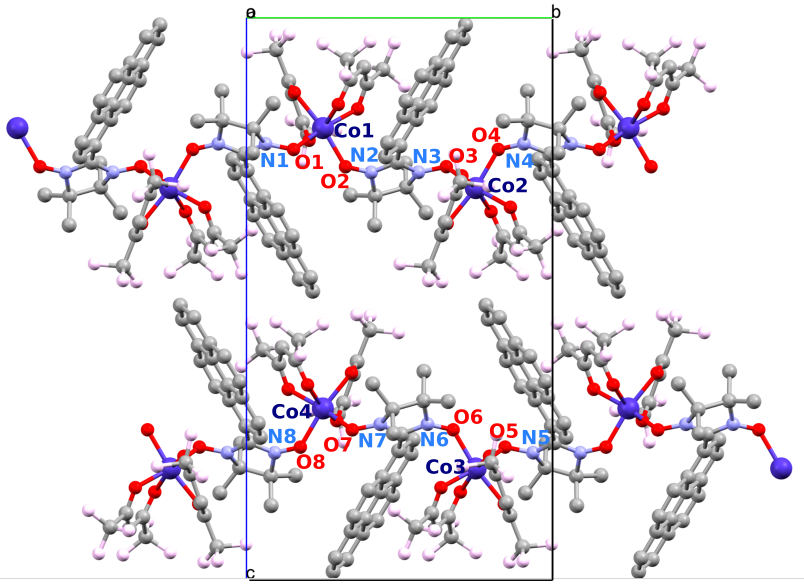

Figure 6.1: Bulk structure of the $[Co(hfac)_2PyrNN]_n$. Cobalt, carbon, nitrogen, oxygen and fluorine are blue, brown, pale blue and pink respectively. Hydrogen atoms and disordered molecules of solvent were omitted for the sake of clarity.

chloroform. However, even if from the stoichometry only two molecules of $CHCl_3$ and two of n-heptane are present, the solvent molecules are intrinsecally disordered and for each solvent four position are possible, with an occupation probability 50% each. This aspect will be discussed in section 6.1.2.

The spin hamiltonian parameters[40] obtained by fitting the $\chi_M T$ data with the branch chain model[193] gives an antiferromagnetic exchange coupling constant metal-radical $J_{Exch} = -161$ cm^{-1} and a single ion anisotropy parameter for Cobalt $D_{Co} = -100$ cm^{-1}. On the other side the exchange coupling strength found by employing the single branch model[194] has a value of $J_{Exch} = -129$ cm^{-1}. Even if the two values are not in perfect accordance, both confirm a strong intrachain antiferromagnetic interaction.

The photomagnetism behaviour of the chain has been investigated and it shows different magnetic properties before and after the interaction with light. For such interesting behavior, the adsorption of these systems on Au(111) surface and silica is currently under investigation and several attempts have already been performed. The rationalization of this system needs therefore an *ab initio* protocol able to deal with the 3D bulk crystals

a	$11.1512\mathring{A}$
b	$13.8502\mathring{A}$
c	$25.7429\mathring{A}$
α	$90°$
β	$99.372°$
γ	$90°$

Table 6.1: Cell parameters employed for the pDFT calculations on the CoPyrNN chain.

	Length ($\mathring{A}$)	Angle $\widehat{CoON}$	Dihedral $\widehat{CoONC}$
Co-O_2	2.046	124.1°	79.1°
Co-O_6	2.043	127.5°	83.9°

Table 6.2: Structural parameters of the Co-O_{rad} bonds

and the 2D surfaces, all applied on a one dimensional system which is intrinsecally periodic as a coordination polymer. The study of bulk one-dimensional systems in literature usually is performed extracting from the periodic structure a fragment whose reduced dimensions allows to perform calculations on the obtained isolated structure at the DFT level[195] or CASSCF,[196] our idea instead is a study fully periodical.

In order to characterize the $[Co(hfac)_2PyrNN]_n$ chain from a theoretical point of view a multilevel procedure is necessary. In the first phase, the choice about the adopted method is made on the basis of its ability to reproduce the bulk properties of the system, in the phase where structural and magnetic properties are determined with a low level of ambiguity, i.e. the crystal. The same final computational protocol, will be successively employed for the study the adsorption of the SCM@surface scenario, where the interpretation of the magnetic, electronic and structural data is an hard and challenging task. The tuning procedure on the bulk data is necessary and unavoidable in order to refine a computational protocol able to move from the isolated molecular units to extended periodic systems. From all these considerations, the following steps were defined:

- ***Divide et Impera Post*-HF calculation on the single repetitive unit.** Indeed the orbitally degenerate high spin Co(II) ions are usually characterized by a pronounced anisotropy and a *post*-HF method to determine the nature of this anisotopy was necessary. The validity of this model have been discussed in the previous chap-

ters: the results of these calculations were employed as a reference to compare the results coming from the DFT calculations.

- **pDFT calculations on the trimeric unit.** At the same time the extended nature of polymeric chains needs a periodic DFT protocol in order to reproduce structural and magnetic properties. CASSCF method is not implemented for periodic calculation and since the final goal is the study of the adsorption process on surface, GPW-pDFT approaches as in CP2K can conjugate accuracy with hardware affordability. Several functionals have therefore been tested on a reduced model, the trimer unit constitued by the Co(II) ion bonded to two PyrNN radicals to have useful hints about the magnetic structure and about it is affected by the functional's choice.

- **pDFT Calculations on the bulk structure.** Finally the best functional (revPBE + U), was finally tested on the real bulk structure of the SC. Geometry optimizations were performed varying the U parameter on the cobalt ion. The reproduction of the bulk geometry, and the experimental exchange coupling constants, have been the main parameters employed to choose the best set of U values on the different atoms.

6.1.1 *Post*-Hartree Fock Calculations

Computational method

All the calculations on the dimer model were performed with MOLCAS 8.1 Quantum Chemistry Software Package.[101] All electron ANO-RCC[102,168,169] basis sets were employed in all the calculations(see table 6.3 for details and contraction schemes). The *divide et impera* approach previously outlined was adopted. A trimeric unit composed by a Co(II) ion fully coordinated by the two $hfac^-$ and the two PyrNN radicals was extracted by the x-ray structure. From this structure two dimer models were made substituing one of the two radicals by an hydroxyl group with the OH bond along the previous ON bond of the radical, in order to preserve the bond's directionality. The substitution by a water molecule, as already performed in literature,[196] was not taken into account. This structural modification gave to the two dimer models a negative total charge.

The energy ladder of the electronic states and the single ion anisotropy of the Co(II) ion have been investigated only for one dimer within the CASSCF/CASSI-SO method and doping the radical with an extra electron in order to turn it into a diamagnetic ligand. The chosen active space for

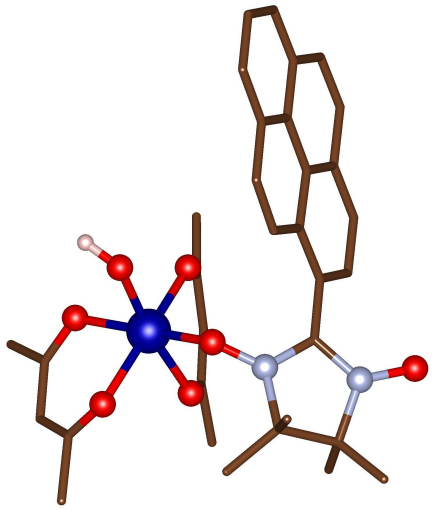

Figure 6.2: One of the two dimer models. Cobalt, carbon, nitrogen and oxygen are blue, brown, pale blue respectively. Hydrogen and fluorine atoms were omitted for the sake of clarity.

Co(II) consists of 7 electrons in the seven 3d-orbitals of the metal ion: CAS (7,5). The 10 quadruplets and the 40 doublets were computed and included in the following spin-orbit calculation. No perturbative method in order to recover part of the dynamical correlation was performed, due to memory limitation.

Atom	Label	Primitives	Contraction
Co	VTZP	[21s15p10d6f4g2h]	[6s5p3d2f1g]
N	VTZP	[14s9p4d3f2g]	[4s3p2d1f]
O	VTZP	[14s9p4d3f2g]	[4s3p2d1f]
C	VDZP	[14s9p4d3f2g]	[3s2p1d]
F	VDZ	[14s9p4d3f2g]	[3s2p]
H	VDZ	[8s4p3d1f]	[2s]

Table 6.3: Contractions of the ANO-RCC basis set used for all CASSCF calculations.

The g-tensor was computed with the SINGLE ANISO module within the pseudospin framework on the lowest Kramers'doublet. Indeed Co(II) is a Kramers' ion due to its odd number of electrons ($3d^7$ configuration).

Energy Levels	Co
E_0	0.000
E_1	182.718
E_2	721.142
E_3	1081.536
E_4	1270.861
E_5	1427.683

Table 6.4: Computed Energy in (cm^{-1}) of the Kramers'doublets at CASSCF/CASSI-SO level for the Cobalt ion in the dimer model

The real spin $S = \frac{3}{2}$ for Co(II) ion was employed to map the magnetic anisotropy tensor $\mathbf{D}$ on the ground and first excited doublets.

In order to compute the isotropic magnetic coupling between the radical and the metal ion, CASSCF calculations were performed without spin-orbit contribution. For the Cobalt-Radical interaction, the active space consisted of the five $3d$ orbitals and the π^* molecular orbital of the radical, CAS (8,6) as in the chimeric $2p$-$3d$-$4f$ compound showed in the previous chapter. The exchange constants were mapped onto the energies of the lowest quintuplet and triplet in energy, as outlined in the previous chapter for the Co-Rad interaction.

Results

The *post*-HF calculations on the single repetitive units confirmed the pronounced anisotropy of the Co(II) ion as observed by experiments. However, the situation is intermediate between an easy axis and an easy-plane scenario. Indeed the values of the g-factors reported in table 6.5 show the presence of an intermediate situation, where g_z is high but also g_y is not negligible. If the two lowest ground Kramers' doublet are mapped on the folowing hamiltonian

$$\mathcal{H} = D\hat{S}_z^2 + E(\hat{S}_x^2 - \hat{S}_y^2) \tag{6.1}$$

The parameter D is negative and large in magnitude, -84 cm^{-1}, near the experimental value of -100 cm^{-1}, and E is prononuced, 21 cm^{-1}, near the limit $-\frac{D}{3} < E < \frac{D}{3}$. The Ising hamiltonian employed to fit the magnetic data is, therefore, only partially justified: an isolated ground state is present (see table 6.4), far from the first excited Kramers' doublet, but its anisotropy is not perfectly axial as an Ising hamiltonian should require. The energy differences between the ferromagnetic and anti-ferromagentic

	Value	a	b'	$c*$
g_x	2.006858657	−0.262675	−0.545288	0.796029
g_y	2.451133404	−0.954874	0.265436	−0.133264
g_z	2.869776429	0.138627	0.795113	0.590405

Table 6.5: Dimer model: values of the main anisotropy Co and their orientations in the crystal frame.

state in the two dimers differ of about one wavenumber, $\Delta E_1 = 112$ and $\Delta E_2 = 113$ cm^{-1}, respectively. Therefore, the exchange coupling constants computed for the two dimers are almost the same, independently of the Hamiltonian employed. Therefore, the obtained values for J_1 and J_2 suggests that in the bulk phase the observed J is not an average, as it could be expected by the slighty different structural parameters for the Co-O_2 and the Co-O_6 bond, but it is the effective value for the Co-NNit exchange coupling.

Assuming for Co(II) a pseudospin $\tilde{S} = 1/2$ as proposed in the previous chapter, the ΔE corresponds exactly to the two theoretical exchange constants mapped on an Heisenberg Hamiltonian. In this case they are very similar in magnitude and sign to the J fitted from experimental data, 112 cm^{-1} against 128 cm^{-1} (or 166 cm^{-1}) respectively.

6.1.2 Density Functional Theory Calculations

Computational Details All the pDFT calculations were performed with the CP2K program package,[95] and the RVV10[165] parametrization approach was used to introduce the dispersion correction term. Norm-conserving Goedecker-Teter-Hutter (GTH) pseudopotentials[166] were used along with GTH double-Z polarized molecularly optimized basis sets for all the atomic species. An energy cut-off of 400 Ry was applied to the plane- wave basis sets. Two different functionals were employed for the calculations: the hybrid functional B3LYP and the meta-GGA functional revPBE.

The geometry optimizations were performed employing the rev-PBE and revPBE+U functionals: the EPS convergence criteria for the single SCF step were fixed to $1 \cdot 10^{-6}$ which corresponds to a energy change about 10^{-6} hartree while the maximum force component were set to $4.5 \cdot 10^{-4}$ Hartree Bohr^{-1}. Single point calculations on the several models, on the x-ray structures and on the optimized ones were performed with revPBE, revPBE+U and B3LYP functionals with a tighter EPS convergence crite-

rion: $1 \cdot 10^{-8}$.

The trimer model was obtained extracting from the X-ray structure a Cobalt ion fully coordinated by the two hfac$^-$ ligands and the two PyrNN radicals (see figure6.3). The Rad-Co-Rad unit was inserted in a cubic cell with 40 $\mathring{A}$ side lengths in order to avoid interaction between the replicas: the Van der Walls radius of the trimer has approximately a diameter about 15 $\mathring{A}$. The unit cell for the calculations of the bulk structure was set coincident to the crystal unit cell from X-ray diffraction measurements, [40] as reported in table 6.1. All the pDFT calculations are fully periodic in the three directions of space.

All the single points calculations were performed by Orbital Transformation method[197] (OT) both for the trimer and for the bulk structures.

In order to reproduce magnetic properties, i.e. the exchange coupling constants, the addition of the Hubbard's U parameter to the revPBE functional is crucial. This method allows to reduce the overdelocalization of the d orbitals in order to reduce the antiferromagnetic constant without loosing computational performance. Optimization of the geometry by periodic DFT was performed with and without the co-cristallized solvent.

The optimization runs were, instead, performed applying a constant smearing of the occupation numbers of the molecular orbitals with a Fermi-Dirac distribution with a temperature of 2500 K. Each optimization was perfomed converging on the ferromagnetic state, even if the ground states is ferrimagnetic, where the radical and the Cobalt spin sublattices are antiparallel between each other. The reasons of this choice are explained more in detail in the discussion about the bulk structure. Such a choice is justifed by the fact that Co(II) has a multi-determinant nature and, within DFT, the optimizazion could lead to biased structures.

Trimer Model

The analysis on the trimer model was performed in order to choose the best density functional able to reproduce the magnetic exchange coupling constants between the transition metal and the PyrNN radical inside the coordination polymer. The trimer model was chosen as a suitable synthesis to map three of the four possible J's, the two Co-Rad interaction and the Rad-Rad one, and do it in a relative short time, compared of doing it on the crystal cell.

The first set of calculations were performed with the hybrid B3LYP functional. Hybrid functionals proved to reproduce magnetic properties in strongly correlated systems in complexes containing transition metals.[178,198,199] However, their application on periodic extended systems is

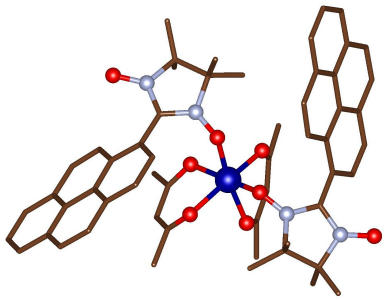

Figure 6.3: Trimer model. Cobalt, carbon, nitrogen and oxygen are blue, brown, pale blue respectively. Hydrogen and fluorine atoms were omitted for the sake of clarity.

not affordable for the accessible computational resources. Therefore, we chose to employ hybrid functionals in order to have *ab initio* unbiased reference calculations, as for the previous *post*-HF calculations, in order to have a reference for less robust methods as the DFT + U: the value of the U in our approach is tuned on its ability to reproduce geometrical and magnetic experimental data.

The main exchange parameters were evaluated by using the broken symmetry appoach, as developed by Noodleman and Norman.[106,107] The spin hamiltonian employed for the trimer consists of three different exchange coupling constants, one for each of the two cobalt-radical bond and one for the Rad-Rad next-nearest neighbour one.

$$\mathcal{H} = J_1 S_{Co} S_{Rad1} + J_2 S_{Co} S_{Rad2} + J_3 S_{Rad1} S_{Rad2} \tag{6.2}$$

Single point energies with different multiplicities were computed on the models. Four determinants are possible, as shown: In principle, from the energies of four determinants, three exchange constants can be extrapolated. The exchange couplings were than obtained by solving the following linear system, where the HS determinant is the high spin one where all the spins are parallel.

$$\begin{pmatrix} E_{HS} - E_{dud} \\ E_{HS} - E_{uud} \\ E_{HS} - E_{duu} \end{pmatrix} = 2 \begin{pmatrix} S_{Co}S_{Rad1} & S_{Co}S_{Rad2} & 0 \\ 0 & S_{Co}S_{Rad2} & S_{Rad1}S_{Rad2} \\ S_{Co}S_{Rad1} & 0 & S_{Rad1}S_{Rad2} \end{pmatrix} \begin{pmatrix} J_1 \\ J_2 \\ J_3 \end{pmatrix} \tag{6.3}$$

The functionals employed were the B3LYP, revPBE and the revPBE+U with three different sets of U parameters acting on the different elements

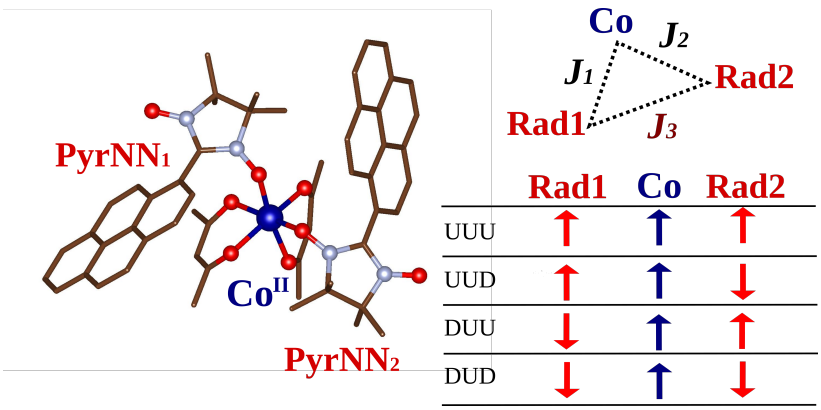

Figure 6.4: Broken symmetry states and spin topology employed for the trimer model. Cobalt, carbon, nitrogen and oxygen are blue, brown, pale blue respectively. Hydrogen and fluorine atoms were omitted for the sake of clarity.

of the structure. The U sets employed are reported in table 6.6. Regarding the set 1, an Hubbard potential U has been applied to the *p*-shell of the donor atoms of the ligands (oxygen and nitrogen): the chosen values for the ligands were reported in a previous paper from Ninova *et al.*[90] In the paper, the HF-like potential acting on the ligands were tuned simulating different experimental data for a derivative of the tetrairon Fe_4Ph family SMM. Hence exchange coupling constants and UV-photoemission spectroscopy have been reproduced by DFT calculation. As stated in the third chapter, even if the Hubbard potential should be tuned for each system, their transferability in this case is justified by the following fact: the iron atoms, in the investigated Fe_4ph molecules, complete their coordination sphere by binding β-diketonates, as the $hfac^-$ in our SCM. In that paper the best values for Oxygen and Fluorine were 3 eV and 2.5 eV respectively, and the same U parameters were applied to our SCM. Regarding the nitrogen atoms, we choose to apply the same value employed for Oxygen ones. Once defined the localizing potential on the ligands, we investigated the effect of this Hubbard like potential on the Cobalt ion: as a preliminary screening, values of 0, 1, and 3 eV, have been choosen. This last value has been choosen because it is similar to what found in literature.[200–202] The tuning of the Hubbard U potential on Cobalt was perfomed on the bulk structure, observing also the effect on the geometry optimization (see next section).

The energies of the determinants are reported in table 6.7. Several

U(eV)	Co	N	O	F
set 0	0.0	3.0	3.0	2.5
set 1	1.0	3.0	3.0	2.5
set 2	3.0	3.0	3.0	2.5

Table 6.6: The two different sets of Hubbard parameters U applied to the elements

	B3LYP	**revPBE**	**revPBE + U (set0)**	**revPBE + U (set1)**	**revPBE + U (set2)**
UUU	-945.41139491	-947.77176721	-946.58361617	-946.5728340	-946.54600628
UUD	-945.41513232	-947.77721477	-946.58681341	-946.5744902	-946.57086162
DUU	-945.4151832	-947.77721360	-946.58717502	-946.5755022	-946.54722619
DUD	-945.4186717	-947.78495164	-946.59011175	-946.5768395	-946.54880796
J_1	536	833	502	369	231 / 205
J_2	529	833	449	219	178 / 205
J_3	44	107	57	70	- / -79

Table 6.7: Energies of the broken symmetry determinants (in Hartree) for the trimer model and exchange coupling constants (in cm^{-1}).

considerations can be made regarding these energies. Starting from the analysis of the different functionals, the UUD, UUD and DUU determinats are quasi-degenerate in energy both in the hybrid (B3LYP) and meta-GGA case (revPBE). Also for 'set-0' (without the localizing potential on Cobalt) the determinants are very close in energy, as expected from *post*-HF calculations. Consequently J_1 and J_2 values are very similar. On the other side, the exchange coupling constants are not in agreement with the experimental data: in the best cases (B3LYP and revPBE+U/set-0) the exchange constants are almost three times the experimental one (129 or 166 cm^{-1}). For hybrids/BS approach, such a result is not surprising.[178]

RevPBE/Set-1 gives two very different values for J_1 and J_2, even if a consistent value of J_3 was found. Instead, the RevPBE/Set-2 gives an inconsistent energy for one determinant: the UUD determinant appears more stable than the DUD one which should be the ground state spin configuration, coherently to what found in the first three cases. Consequently, since that determinant cannot be considered, two options of spin mapping are possible on the determinants whose energy ladder is coherent with the other cases (UUU, DUU and DUD):

- $J_1 = J_2$. The average exchange constant Co-Rad is in good agreement with the experimental data, while J_3 is opposite in sign, i.e. ferromagnetic, in disagreement with the previous cases.

- $J_3 = 0$. In that case the J_1 and J_2 are quite different, their ratio is 0.77, in agreement with the values found form Scarrozza *et al.*[93] for the CoPhOMe chain. However, they found also a rad-rad ferromagnetic interaction, an order of magnitude smaller than the Co-rad one: this is in contrast with our results that show a J_3 around $\frac{1}{3}J_1$

In our opinion the correct interpretation should be the first one based on two considerations: i) the results of the *post*-Hartree Fock calculations show that J_1 and J_2 should be similar; ii) When B3LYP functional is employed, which is the most confident DFT method, the two determinats UUD and DUU are almost degenerate in energy: Totti *et al.*[118] demonstrated that from single-point energies of the broken symmetry states, the spin topology of a multi-spin system can be deduced.

Therefore the quality of our computed energies has been checked in order to confirm if the BS calculation is converging on the correct states. In order to verify that the *3d*-orbitals have been plotted in order to check the consistency of the d orbitals throughout the different determinants.

Observing the orbitals computed with the B3LYP functional (see figure 6.5) it can be evinced that the same energy structure was preserved in the three determinants. The three unoccupied β orbitals have the same orientation shape and numerical order in all the spin configurations. The same considerations apply to the occupied ones, even if their order is inverted: 212 and 208 cm^{-1} of DUU configuration correspond to 209 and 212 cm^{-1} in UUD, respectively. Conversely, the orbitals computed with the revPBE + U/set-2 aproach (see fig 6.6) show that the method is not sufficiently robust to converge into the same state for all the configurations. The computed states need therefore to be carefully checked in order to be sure about the calculated solutions.

In this case, we can observe that DUU and DUD configurations preserve the same sets of orbitals, while the UUD set seems to converge on an electronic state characterized by a different arrangement of *3d*-orbitals: the exclusion of the UUD determinants from the BS mapping is justified since it does not produce a coherent electronic configuration within the $3d$ orbitals.

In conclusion, from the series of calculation performed on this trimer model, the revPBE + U approach seems justified and gives the best results in terms of the value of exchange coupling. The possibility to use a meta-GGA functional moreover allows to speed up the calculation and, as a consequence, the application of this protocol to scenarios consisting of hundreds of heavy atoms: the SCM adsorbed on metallic surfaces as the

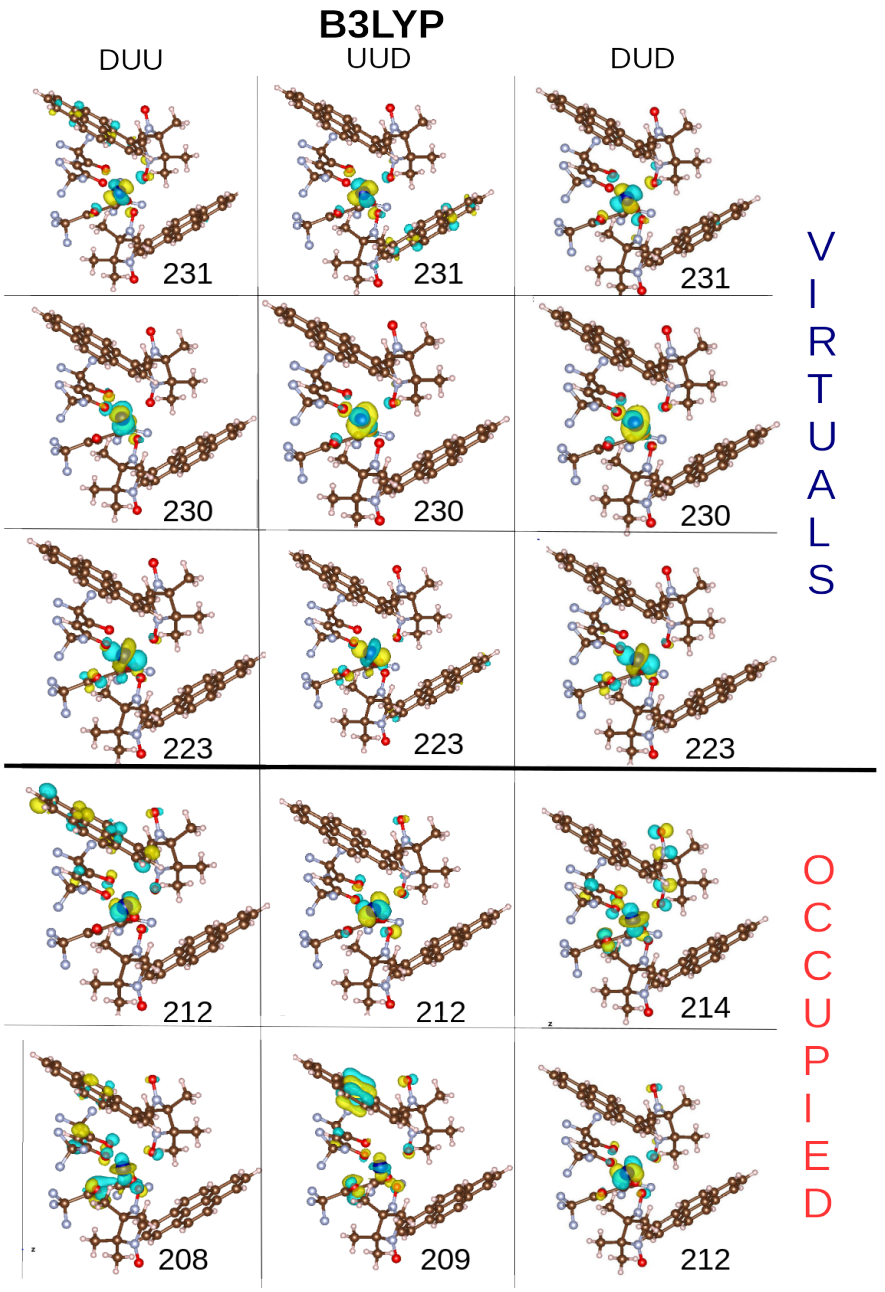

Figure 6.5: Trimer model. β *3d*-orbitals of the cobalt ion computed with the B3LYP funtional for three different BS determinats. The isosurface level was set to 0.05 $e \cdot (a.u.)^{-3}$. Cobalt, carbon, nitrogen and oxygen are blue, brown, pale blue respectively.

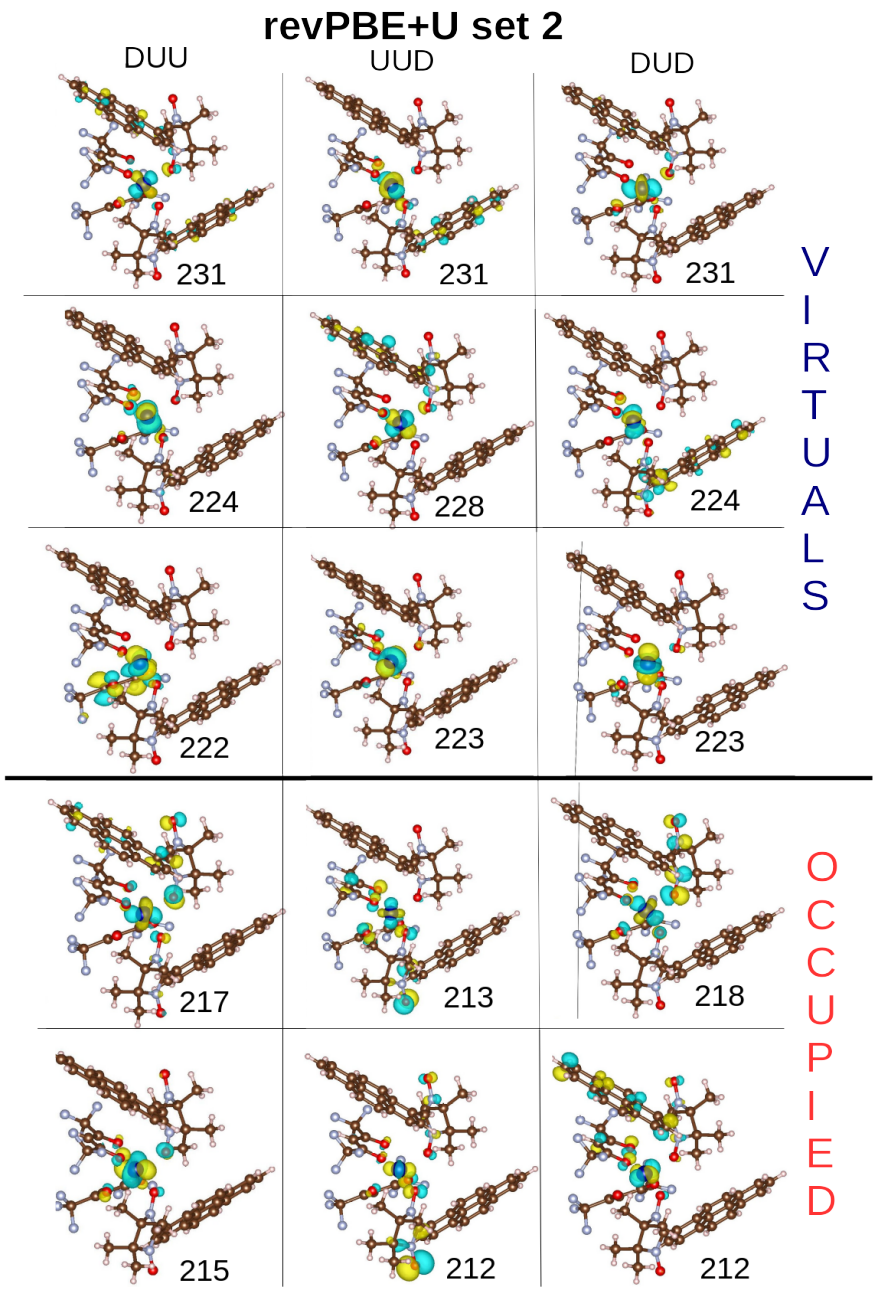

Figure 6.6: Trimer model. β *3d*-orbitals of the cobalt ion computed with the revPBE + U funtional and with the set of parameters number 2 for three different BS determinants. The isosurface level was set to 0.05 $e \cdot (a.u.)^{-3}$. Cobalt, carbon, nitrogen and oxygen are blue, brown and pale blue respectively.

Au(111).

Crystal Bulk Structure

An adsorbed molecule on a surface will experiment structural modifications that can seriously affect magnetic and electronic properties. A reliable picture of this process is possible only applying a protocol that proved to reproduce the experimental data in a situation where their interpretation is not ambiguous: in that case, structural and magnetic data of the bulk structure. The structure of the CoPyrNN chain has been well resolved by x-ray diffraction measurements, and the magnetic properties have been extrapolated by different methods which provided a coherent picture, as outlined in the introduction.

Structural analysis Inside this framework, however, a main problem arises in order to deal with the optimization of the bulk geometry by periodic DFT: the presence of disordered solvent molecules inside the crystal structure. Indeed, the unit cell is composed by two parallel chains each constituted by two Co(II) and two organic radicals with two molecules of $CHCl_3$ and two of n-heptane interposed. They are necessary in order to stabilize the packing because they occupy the intrachain space. However the solvent molecules are intrinsecally disordered and with a 50% occupation probability for each position. Four possible arrangements are therefore possible by the point group symmetry. Two of them imply that one chain is surrounded only by molecules of Chloroform and one by molecules of n-heptane. In the other two arrangements each chain is surrounded by one molecule of n-heptane and one of $CHCl_3$. Therefore, in order to probe the effect of the solvent, optimizations were performed with and without the solvent. At this level, the revPBE functional with no Hubbard U parameter was employed. Moreover the optimizations without solvent were performed converging on the ferrimagnetic (with the two spin sublattices anti-parallel to each other), which is the experimental ground state, and the ferromagnetic state (Cobalt and radical spins parallel). Being the DFT a monodeterminatal method, the ferrimagnetic state is not eigenfunction of the total spin operator and its ability to converge to a reliable solution in presence of complex orbital degeneracy as fo Co(II) ions is not always possible. The main structural parameters regarding the Co-Rad bonds are shown in tables 6.8 and 6.9.

The results regarding the two optimizations without solvent show, firstly, that the values of the Co-O_rad bond lengths and angles present only small variations. The maximum bond length variation is 0.05 $\AA$,

	Co_1-O_1	Co_1-O_2	Co_2-O_3	Co_2-O_4	Co_3-O_5	Co_3-O_6	Co_4-O_7	Co_4-O_8	Average
X ray	2.05	2.04	2.05	2.04	2.05	2.04	2.05	2.04	**2.045**
				Without solvent					
Ferrimagnetic	1.998	1.995	1.997	1.994	2.003	2.028	2.010	2.023	**2.006**
Ferromagnetic	2.048	1.999	2.049	1.997	2.052	1.963	2.046	1.998	**2.019**
				With solvent					
Ferromagnetic	2.069	2.045	2.040	2.039	2.040	2.038	2.066	2.046	**2.047**

Table 6.8: Lengths of the Co-O_{rad} bonds for the optimized structures.

	$\widehat{Co_1O_1N_1}$	$\widehat{Co_1O_2N_2}$	$\widehat{Co_2O_3N_3}$	$\widehat{Co_2O_4N_4}$	$\widehat{Co_3O_5N_5}$	$\widehat{Co_3O_6N_6}$	$\widehat{Co_4O_7N_7}$	$\widehat{Co_4O_8N_8}$	Average
X ray	124.1	127.5	124.1	127.5	124.1	127.5	124.1	127.5	**125.8**
				Without solvent (revPBE)					
Ferrimagnetic	122.7	126.8	122.7	126.9	122.0	126.6	124.1	126.7	**124.8**
Ferromagnetic	124.6	127.1	124.5	127.0	125.4	127.4	124.5	127.1	**126.0**
				With solvent (revPBE+U/set-1)					
Ferromagnetic	124.1	127.6	125.4	128.3	125.5	128.3	124.0	127.7	**126.3**

Table 6.9: Angles Co-O_{rad}-N_{rad} for the optimized structures.

while for the angles is less than 2°. However, the optimization in the ferrimagnetic state shows stronger variations with respect to the optimization in the ferromagnetic one. The average values, both for angles and bond lengths, is closer to the x-ray one for the optimization in the ferromagnetic states: it appears the best option in order to perform a geometry optimization on the bulk structure.

The optimizations without the co-crystallized solvent, at the same time, evidence that the Co-O_{rad} bonds tend to differentiate themselves into two different groups: one with a lower, about 2.00 $\AA$, and one with a larger bond distance, about 2.05 $\AA$. This variation is not present in the x-ray structure, where both Co-O_{rad} bonds have the same value, about 2.04-2.05 $\AA$. In order to probe if this differentiation is due to the absence of the solvent, we performed an optimization on an isotructural chain, the $[Co(hfac)_2NaphNN]_n$ chain[203] (CoNaphNN) which has the same structure but a different pendant arm, a naftyl group instead of a pyrenyl one. In this second chain there is no solvent in the crystal unit cell. The two Co-O_{rad} bonds show indeed a more pronounced variation regarding lengths and angles in the x-ray structure: 0.03 $\AA$ and 2°, respectively. These ranges of values are kept after the optimization, as it is shown in tables 6.10 and 6.11: the absence of co-crystallized solvent allows a stronger differentiation of the two bonds on the two sides of the radical which is observable on the x-ray geometry and optimized one. However, even if the effect of the solvent is a partial simmetrization of the two Co-O_{rad} bonds for each metal ion, and a better agreement in the average with the experimental data, it is worth to stress that the choice of an arbitrary position of

	Co_1-O_1	Co_1-O_2	Co_2-O_3	Co_2-O_4	Co_3-O_5	Co_3-O_6	Co_4-O_7	Co_4-O_8	Average
X ray	2.06	2.04	2.06	2.04	2.06	2.04	2.06	2.04	2.05
Ferro	2.045	2.073	2.045	2.072	2.043	2.073	2.043	2.073	2.058

Table 6.10: Lengths of the Co-O_{rad} bonds for the optimized structures of CoNaphNN.

	$\widehat{Co_1O_1N_1}$	$\widehat{Co_1O_2N_2}$	$\widehat{Co_2O_3N_3}$	$\widehat{Co_2O_4N_4}$	$\widehat{Co_3O_5N_5}$	$\widehat{Co_3O_6N_6}$	$\widehat{Co_4O_7N_7}$	$\widehat{Co_4O_8N_8}$	Average
X ray	125.5	127.6	125.5	127.6	125.5	127.6	125.5	127.6	126.6
Ferro	124.7	126.6	124.7	126.6	124.7	126.6	124.7	126.6	125.7

Table 6.11: Angles Co-O_{rad}-N_{rad} for the optimized structures of CoNaphNN.

the solvent between the four possible induces the removal of the punctual symmetry on behalf of a localized situation as for CoNaphNN.

Once defined that the presence of the solvent molecules are necessary, the geometry optimization was performed with the parameters of the 'set-2' employed for the trimer model: the employment of the localizing potential was necessary due to the impossibility to reach SCF-convergence employing the pure revPBE functional. The arrangement of the two molecules of n-heptane and the two molecules of chloroform was choosen in order to have around each chain one molecule of both species. We expect an influence on the optimized geometry due to the application of the U parameter on the metal ion, as shown by the optimization on the bulk structure performed on the Fe_4Ph molecule by Ninova *et al.*:[204,205] the bond lengths are slightly different for the optimization with and without U as observed here for the $[Co(hfac)_2PyrNN]_n$ chain. So the obtained results are not directly comparable with the optimization performed without the solvent where no U parameter was applied.

The values obtained for the Co-O bond lengths confirm the presence of the solvent is not innocent with respect to the Cobalt-radical main structural parameters. However, the agreement with the experimental x-ray structure is excellent both for the average values of the bond length and angles, as shown in tables 6.8 and 6.9. The x-ray geometry and the optimized one (set 2), have been superimposed in figure 6.7.

Starting from this optimized geometry with revPBE+1 (set2), several optimization runs have been performed varying the Hubbard U parameter on the Cobalt ion and keeping constant the values on the others atoms (3.0 eV for O, N an 2.5 eV for F). The RMSD values, the spin densities on the Cobalt ions and the computed exchange coupled parameters are in table 6.12.

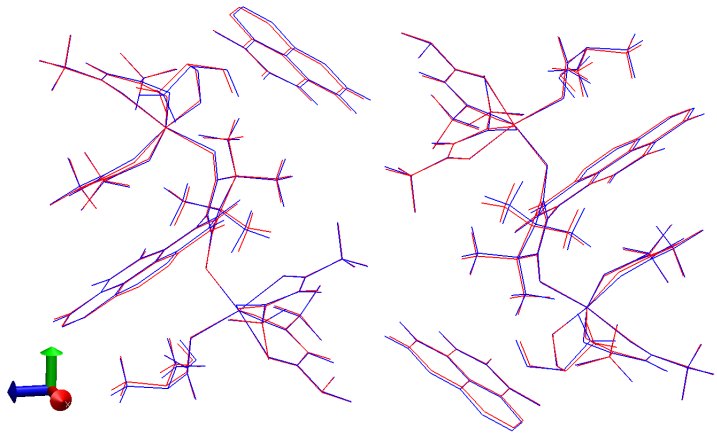

Figure 6.7: Superimposed x-ray geometry (red) and optimized one (blue) with revPBE+1/set-1 functional.

$U_{Co}(eV)$	$RMSD$		ρ_{Co}	
	without H	with H	$UUUU$	$UDUD$
1.5	0.0951	0.1384	2.74	2.67
2.5	0.0954	0.1389	2.77	2.73
3.0	0.0955	0.1390	2.78	2.74
3.5	0.0954	0.1389	2.79	2.75
4.0	0.0956	0.1391	2.80	2.77
4.5	0.0957	0.1392	2.81	2.79
5.0	0.0958	0.1394	2.82	2.80
5.5	0.0959	0.1395	2.83	2.81
		X-ray		
no U	–	–	2.75	2.43
3.0	–	–	2.78	2.73
$B3LYP$	–	–	2.77	2.68

Table 6.12: RMSD of the optimized structure with respect to the experimental one and the Löwdin spin densities on Co atoms. The RMSDs have been computed without considering the molecules of solvent, since their coordinates were disordered

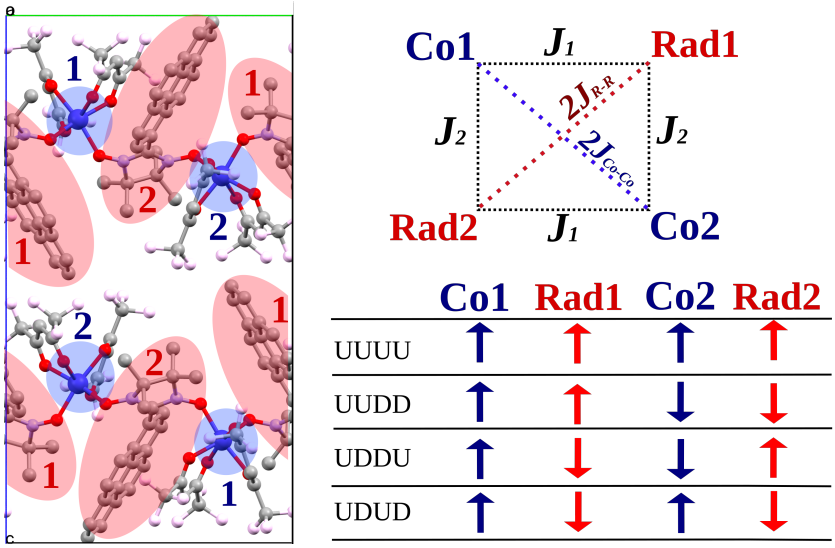

Figure 6.8: Broken symmetry determinants and spin topology employed for the calculations on the bulk structure of the chain. Cobalt, carbon, nitrogen, oxygen and fluorine are blue, brown, pale blue and pink respectively. Hydrogen atoms were omitted for the sake of clarity.

From the RMSD values, the optimized geometry showed only minimal modifications between each other and therefore, as already evidenced, with the x-ray structure. The RMSD rises with the increasing of U on the cobalt ions, but it still remains quite low for all the optimized structures. As expected, being U a localizing Coulomb potential, the spin density on the transition metal increases together with U.

Magnetic Properties On the optimized geometry the exchange coupling constant J_{Co-Rad} were then computed. Regarding the magnetic properties, the main question is the definition of the best spin topology to apply in order to map the BS energies for each multiplicity. In order to have a reliable picture of the main interactions, firstly single point calculations on the X-ray structure with the B3LYP hybrid functional have been performed. The calculations on the trimer model indeed showed that the hybrid functionals are quite robust and are able to converge to a coherent set of states for all the BS configurations. The energies of the determinants are showed in table 6.13. The employed spin topology took into account the two possible exchange constants for the Co-Rad iteraction (J_1 and J_2) and the two possible Co-Co and Rad-Rad interactions. These two

	B3LYP	**revPBE+U/set-2**
UUUU	-3006.077696909	-3008.61459134
UDUD	-3006.113625467	-3008.63421016
UUDD	-3006.098771362	-3008.62742137
UDDU	-3006.098123296	-3008.62504467
UUDU	-3006.092133863	-3008.60295549
UDUU	-3006.095007499	-3008.61310348

Table 6.13: Energies of the broken symmetry determinants (in Hartree) computed on the x-ray structure.

	B3LYP fitted	**B3LYP linear system**	**revPBE+U/set1 Fitted**
J_1	645 (100)	657	316(68)
J_2	669 (100)	657	402(68)
J_{R-R}	309 (382)	-92	-
J_{Co-Co}	1 (41)	-41	-

Table 6.14: Exchange coupling constants (in cm^{-1}) computed on the x-ray structure. The standard errors (in cm^{-1}) are in the parentesis.

last next-nearest neighbour couplings along the chain were expressed as $2J_{R-R}$ and $2J_{Co-Co}$ respectively: the factor of 2 is needed to account the double interactions for the two kinds of next nearest neighbour exchange interactions in the real linear chain. The complexive exchange constants were then fitted by minimum square method, as showed by Bencini and Totti,[118] with the following system of linear equations.

$$\begin{cases} \frac{E(UUUU)}{2} = 2J_1\frac{3}{4} + 2J_2\frac{3}{4} + 2J_{R-R}\frac{1}{4} + 2J_{Co-Co}\frac{9}{4} \\ \frac{E(UDUD)}{2} = -2J_1\frac{3}{4} - 2J_2\frac{3}{4} + 2J_{R-R}\frac{1}{4} + 2J_{Co-Co}\frac{9}{4} \\ \frac{E(UUDD)}{2} = 2J_1\frac{3}{4} - 2J_2\frac{3}{4} - 2J_{R-R}\frac{1}{4} - 2J_{Co-Co}\frac{9}{4} \\ \frac{E(UDDU)}{2} = -2J_1\frac{3}{4} + 2J_2\frac{3}{4} - 2J_{R-R}\frac{1}{4} - 2J_{Co-Co}\frac{9}{4} \\ \frac{E(UUDU)}{2} = 0J_1\frac{3}{4} + 0J_2\frac{3}{4} + 2J_{R-R}\frac{1}{4} - 2J_{Co-Co}\frac{9}{4} \\ \frac{E(UDUU)}{2} = 0J_1\frac{3}{4} + 0J_2\frac{3}{4} - 2J_{R-R}\frac{1}{4} + 2J_{Co-Co}\frac{9}{4} \end{cases} \tag{6.4}$$

The comprehensive spin topology employed is showed in figure 6.8. The results evidence that the convergence to a correct solution is not an easy task.

The obtained constants are shown in table 6.14. The energies obtained with the hybrid functional appear coherent: the energies of the BS states are inside the range defined by the energies of the states that, in principle, should be the highest and the lowest one in energy, i.e. the ferromagentic

(UUUU) and the ferrimagnetic (UDUD) one. However, employing the whole set of determinants, the fitting gives an acceptable value for J_1 and J_2, at least in agreement with the calculations performed on the trimer model (see table 6.7). Moreover, the equivalence of the Co-Rad exchange interaction is again confirmed: the UUDD and UDDU determinats are quasi-degenerate in energy and the difference between the computed J is inside the error value. On the other side, regarding the next-nearest neighbour interaction, the values obtained are smaller than the computed error: the fitted value is therefore not reliable. However, if we map the BS spin hamiltonian as we made for the trimer model, excluding from the linear system the UUDD and UDDU determinats and imposing $J_1 = J_2$, the solution we obtain is presented in the second column of table 6.14. The Co-Co and the Rad-Rad interactions are both ferromagnetic and of the same order of magnitude, $0.14J_1$ and $0.06J_1$ respectively: these two values are inside the previous determined errors.

An indication that some determinants did not converge correctly, it can be found observing the Löwdin spin densities on the Cobalt ion. For the states computed by B3LYP functional both chains inside the unit cell seem to converge to the same states, as can be observed comparing the values of the spin densities on equivalent Cobalt ions of different chains in table 6.15 (Co1 is equivalent to Co3, Co2 is equivalent to Co4, see also figure 6.1. On the other side, for the solution with revPBE+U, the two chains appear not to converge into the same solution: for instance, if we observe determinant UDUU, Co4 has not the same spin density of Co2, and the same can be observed for UUDU, were both Cobalt ions of the second chain show a spin density which is 0.1 lower with respect of the first one. These two states indeed present an unreliable energy, higher than the ferromagnetic state's one.

The same procedure was applied to optimized geometry in presence of the co-crystallized solvent. The choice of the optimization procedure have been already discussed in the previous section. The energies of the computed states and the exchange coupling constants are showed in table 6.16 and 6.17. The obtained exchange constants obtained by fit of the energies and by solving the linear system are again in agreement between each other: both shows a not negligible radical-radical antiferromagnetic interaction and an about five times stronger metal radical magnetic exchange. At the same time both mapping methods show an order of magnitude lower antiferromagnetic Co-Co interaction.

Regarding the results with the revPBE+U approach instead, the energies are not employable to extract a reliable set of exchange costants.

	UDUD	UUUU	UUDD	UDDU	UDUU UUDU	
			B3LYP			
Co1	2.684549	2.770707	2.715264	2.724450	2.730801	2.768387
Co2	2.684551	2.770696	-2.715264	-2.724458	2.720935	-2.678772
Co3	2.684549	2.770696	2.715262	2.724448	2.730345	2.767918
Co4	2.684552	2.770701	-2.715263	-2.724447	2.722925	-2.676254
			revPBE+U/set-2			
Co1	2.732992	2.773454	2.751634	2.749811	2.751853	2.789079
Co2	2.732993	2.773455	-2.751636	-2.749812	2.753694	-2.732102
Co3	2.732993	2.773454	2.751634	2.749812	2.752675	2.771637
Co4	2.732992	2.773454	-2.751635	-2.749811	2.715149	-2.723322

Table 6.15: Spin densities on cobalt ions computed on x-ray gometry by revPBE+U/set-2 and B3LYP.

	B3LYP	**revPBE+U/set-2**
UUUU	-3207.6017032511	-3211.1012596948
UDUD	-3207.6313995266	-3211.1103733782
UUDD	-3207.6164969914	-3211.0786820331
UDDU	-3207.6217530638	-3211.1173838905
UUDU	-3207.6174790608	-3211.0677846836
UDUU	-3207.6170217870	-3211.0941810680

Table 6.16: Energies of the broken symmetry determinants (in Hartree) computed on the optimized structure.

	B3LYP fitted	**B3LYP linear system**
J_1	639 (25)	543
J_2	447 (25)	543
J_{R-R}	166 (64)	101
J_{Co-Co}	12 (7)	5.7

Table 6.17: Exchange coupling constants (in cm^{-1}) computed on the optimized structure. The standard errors (in cm^{-1}) are in the parentesis.

	UDUD	UUUU	UUDD	UDDU	UDUU	UUDU
			B3LYP			
Co1	2.687970	2.773356	2.726369	2.733334	2.737429	2.775154
Co2	2.697576	2.779061	-2.732116	-2.736064	2.734550	-2.692936
Co3	2.691937	2.775135	2.734401	2.738359	2.731123	2.773398
Co4	2.694653	2.776091	-2.725096	-2.733020	2.729833	-2.683204
			revPBE+1/set-2			
Co1	2.735697	2.773510	2.756432	2.752284	2.753645	2.772130
Co2	2.743182	2.776420	-2.758658	-2.754939	2.759290	-2.741686
Co3	2.745287	2.797322	2.758998	2.755388	2.720959	2.745584
Co4	2.736289	2.794893	-2.756576	-2.752644	2.770543	-2.698844

Table 6.18: Spin densities on cobalt ions computed on optimized gometry by revPBE+U/set-1 and B3LYP.

Indeed observing the spin densities in table 6.18, in the DFT+U case only few states (UUUU, UDUD, UUDD) show the same values for both chains. Therefore from these determinats only a screening, in function of U, of the average Co-Rad exchange coupling constants is possible. This approximation can appear brutal, due to the neglecting both next nearest neighbour exchange interactions and the eventual two different J_1 and J_2. However, the equivalence of J_1 and J_2 has been already proved by the calculations on the trimer model and on the x-ray structure. The eventual inequivalence can be attributed at this point to the localization induced by the choice of a specific arrangements of the solvent between the four different possibilies.

As expected, the computed J_{Co-Rad} values show a strong influence with respect to U, (see table 6.19). It changes from 255 to 73 cm^{-1}, for U values on Cobalt which ranges from 1.5 to 5.5 eV. As expected, the J value decreases in function of the increase of the localization of the $3d$ orbitals: the reduction of the overlap with the π^* radical orbital gradually reduces the antiferromagnetic contribution. From the obtained value we can conclude that an optimal U value on the Co(II) ion can be from 3.0 to 4.0 eV: the mapped exchange contant indeed is included between the two experimental ones.

From B3LYP calculation it emerged that the J_{Co-Co} can be, in principle, neglected. The same cannot be said for the $J_{Rad-Rad}$ and more effort should be done to overcome the determinants convergence problems.

However the unsuccessful mapping of the $J_{Rad-Rad}$ interaction is a not a limiting factor. Once a reliable method is found to converge to the correct solution for the UUDU and UDUU spin configurations, for instance

$U_{Co}(eV)$	$J_{Co-Rad}(cm^{-1})$
1.5	255
2.5	191
3.0	166
3.5	144
4.0	124
4.5	105
5.0	88
5.5	73
no U	876
$B3LYP$	543

Table 6.19: Exchange coupling constants J_{Co-Rad} (in cm^{-1}).

by inverting occupied and unoccupied orbitals, the best Co-Rad exchange constants can be choosen by a list of different options already tested and reliable.

6.2 Summary

The multilevel calculations performed on the $[Co(hfac)_2PyrNN]_n$ chain showed that a multilevel characterization of magnetic coordination polymers is a challenging but unavoidable task. Indeed, without the informations coming from different methods and different levels of theory, the lack of reliability of the protocol could lead to misinterpret the experimental findings and viceversa. Instead in this case, the computational results can shed new light on the common interpretation of the magnetic properties of ferrimagnetic SCMs.

The *post*-HF calculations performed on the dimeric unit showed a pronounced rhombic anisotropy which could question the application of the simple Glauber model to interpret the magnetization dynamic. At the same time, the substantially equivalence of the two J_{Co-Rad} has been demonstrated. Despite the two slightly different Co-O_{Rad} bond lengths and Co-O_{Rad}-N_{Rad} angles, the two magnetic interactions are practically undistinguishable. An extrapolation of this dimeric unit from the optimized SCM@surface in order to monitor effects on the anisotropy and the ladder of the excited states.

Regarding the calculations on the trimer model, the revPBE + U approach appears necessary in order to reproduce the experimental magnetic constants, and the equivalence between the two J_{Co-Rad} is confirmed by the calculation with hybrid B3LYP functionals and pure revPBE. The

reliability of the revPBE approach has been also determined by means of a careful analysis of the molecular orbitals localized on the cobalt ion. Moreover a not negligible ferromagnetic interaction, about 1/3 of J_{Co-Rad}, between next-nearest neighbour radical units has been determined. Such result suggests the possibilty that the magnitude of the experimental value of the J_{Co-Rad} could be biased by this ferromagnetic interaction. Such a point will be further investigated.

The optimizations performed on the bulk structure finally validated the proposed protocol. In details: i) the optimization should be performed in the ferromagnetic state and in presence of the solvent, even if it introduces an asymmetrization of the chain's structure; ii) the DFT+U approach is a reliable protocol able to determine the strength and the sign of the Co-O_{Rad} exchange coupling, but hard access to the correct determinants necessary to map the Co-Co and Rad-Rad interaction.

This is not true for the isolated trimer model, where an extrapolation from the optimized structure of a representative dimeric and trimeric units could be made in order for the calculation of the unaccessible magnetic interaction.

The work presented in this chapter will represent a solid base for the the characterization of the system once adsorbed on surface.

Chapter 7

Final Remarks

The different molecular magnetic materials investigated in this work of thesis proved all the potentiality of *ab initio* methods, *post*-HF and DFT. Their versatility allows to study different types of systems, each characterized by a peculiar magnetic structure.

The deep analysis carried on mononuclear lanthanide containing SIMs showed that all the main experimental data, necessary to fully characterize the magnetic properties of such systems, can be rationalized by means of the informations provided by CASSCF/CASSI calculations. Moreover, a rational set up of the employed model, for what concerns fine structural parameters as orientation of directly bonded water molecule, and the account of the periodic electrostatic potential inside the crystal, is able to provide results in excellent agreement with the experimental data. A reliable modelization is able to provide an higher level of results also with respect to more time consuming, and resources demanding methods, such as CASPT2. It was finally shed new light on the nature of the coordinate bond in lanthanides: a covalent interaction between the $4f$-orbitals and the ligands, beyond the purely electrostatic interaction, proved to be necessary in order to rationalize the magnetic properties.

The proof of reliability, provided with this work, suggests new development regarding the study of mononuclear complexes. Firstly, periodic optimizations at the DFT level of lanthanide containing crystals, at the same time of the bulk structure and the periodic cell, could be attempted. Once the ability to reproduce periodic bulk properties is demonstrated, study on these systems under the variation of physical parameters, such as the applications of external pressure, could be investigated. Also the prediction of different behaviours by small variations of some structural

parameters, for instance removal of solvent molecules, could be of interest in order to direct future investigations in the area. The simulation of the behaviour in aqueous solutions to rationalize paramagnetic NMR relaxation experiments is a further development of the work presented.

Reagarding heterospin systems instead, the proposed approach can be easily extended to different classes of compounds without any loss of generality. Our method allows the screeening of exchange coupling parameters of extended series of isostructural compounds, and allows to perform magneto-structural correlations in function of bonding parameters, not only in order to find general trends but also to have a comparison with the most wide-spread DFT methods. This possibility to perform preventively such analysis could orient the synthetic efforts towards the most promising ligands and ions for future applications as a storage of information or quantum computation. For instance, the employment of these systems to perform logical operation would require several interacting units with long decoherence time, able to interact between each other: hence magnetic exchange couplings in the order of fractions of wavenumber are required, and our method proved to be very sensitive also to small variations of the bonding dihedral angles, and to the consequent exchange modulations of few tenths of cm^{-1}.

Finally an optimal computational protocol, able to reproduce magnetic and structural properties of cobalt based ferrimagnetic SCMs, has been tuned in order to move towards the next step of the study: the main bottleneck towards end-user application of molecular-based magnets, i.e. the adsorption on surface. The main structural parameters has been rationalized, and a suitable protocol to obtain the exchange coupling interactions is proposed. This method is, therefore, suitable to investigate structural modifications and magnetic interactions with different types of surfaces. The research on this aspect will be extremely challenging but necessary towards the implementation of these systems in multifunctional materials and spintronic devices.

Bibliography

[1] D. Gatteschi, R. Sessoli and J. Villain, *Molecular Nanomagnets*, Oxford University Press, Oxford, 2006.

[2] R. Sessoli, D. Gatteschi, A. Caneschi and M. A. Novak, *Nature*, 1993, **365**, 141–143.

[3] B. Barbara, W. Wernsdorfer, L. C. Sampaio, J. G. Park, C. Paulsen, M. A. Novak, R. Ferré, D. Mailly, R. Sessoli, A. Caneschi, K. Hasselbach, A. Benoit and L. Thomas, *J. Magn. Magn. Mater.*, 1995, **140-144**, 1825–1828.

[4] L. Thomas, F. F. Lionti, R. Ballou, D. Gatteschi, R. Sessoli and B. Barbara, *Nature*, 1996, **383**, 145–147.

[5] D. Gatteschi and R. Sessoli, *Angew. Chemie - Int. Ed.*, 2003, **42**, 268–297.

[6] H. L. C. Feltham and S. Brooker, *Coord. Chem. Rev.*, 2014, **276**, 1–33.

[7] F. E. Kalff, M. P. Rebergen, E. Fahrenfort, J. Girovsky, R. Toskovic, J. L. Lado, J. Fernández-Rossier and A. F. Otte, *Nat. Nanotechnol.*, 2016, **18**, 1–5.

[8] M. Mannini, F. Pineider, P. Sainctavit, C. Danieli, E. Otero, C. Sciancalepore, A. M. Talarico, M.-a. Arrio, A. Cornia, D. Gatteschi and R. Sessoli, *Nat. Mater.*, 2009, **8**, 194–197.

[9] M. Mannini, F. Pineider, C. Danieli, F. Totti, L. Sorace, P. Sainctavit, M.-a. Arrio, E. Otero, L. Joly, J. C. Cezar, A. Cornia and R. Sessoli, *Nature*, 2010, **468**, 417–21.

[10] D. Aguila, L. A. Barrios, V. Velasco, O. Roubeau, A. Repolles, P. J. Alonso, J. Sese, S. J. Teat, F. Luis, G. Aromi and J. Pablo, *J. Am. Chem. Soc.*, 2014, 14215–14222.

[11] M. Shiddiq, D. Komijani, Y. Duan, A. Gaita-Ariño, E. Coronado and S. Hill, *Nature*, 2016, **531**, 348–351.

[12] M. D. Jenkins, Y. Duan, B. Diosdado, J. J. García-Ripoll, A. Gaita-Ariño, C. Giménez-Saiz, P. J. Alonso, E. Coronado and F. Luis, *Phys. Rev. B - Condens. Matter Mater. Phys.*, 2017, **95**, 1–8.

[13] M. D. Jenkins, D. Zueco, O. Roubeau, G. Aromí, J. Majer and F. Luis, *Dalt. Trans.*, 2016, **45**, 16682–16693.

[14] S. Sanvito, *Chem. Soc. Rev.*, 2011, **40**, 3336.

[15] L. Bogani and W. Wernsdorfer, *Nat. Mater.*, 2008, **7**, 179–186.

[16] R. Vincent, S. Klyatskaya, M. Ruben, W. Wernsdorfer and F. Balestro, *Nature*, 2012, **488**, 357–360.

[17] M. Urdampilleta, S. Klyatskaya, J.-P. Cleuziou, M. Ruben and W. Wernsdorfer, *Nat. Mater.*, 2011, **10**, 502–506.

[18] M. R. Pederson and S. N. Khanna, *Phys. Rev. B*, 1999, **60**, 9566–9572.

[19] E. E. Moushi, T. C. Stamatatos, W. Wernsdorfer, V. Nastopoulos, G. Christou and A. J. Tasiopoulos, *Inorg. Chem.*, 2009, **48**, 5049–5051.

[20] A. J. Tasiopoulos, A. Vinslava, W. Wernsdorfer, K. A. Abboud and G. Christou, *Angew. Chemie - Int. Ed.*, 2004, **43**, 2117–2121.

[21] A. L. Barra, D. Gatteschi and R. Sessoli, *Phys. Rev. B*, 1997, **56**, 8192–8198.

[22] F. Neese, *J. Chem. Phys.*, 2007, **127**, 164112.

[23] A. Bencini and D. Gatteschi, *EPR of Exchange Coupled Systems*, Dover Publicatons, Mineola, New York, 2012.

[24] O. Waldmann, *Inorg. Chem.*, 2007, **46**, 10035–10037.

[25] N. Ishikawa, M. Sugita, T. Ishikawa, S.-y. Koshihara and Y. Kaizu, *J. Am. Chem. Soc.*, 2003, **125**, 8694–8695.

[26] S. Cotton, *Lanthanide and Actinide Chemistry*, Wiley and Sons, Chichester, 2006.

[27] S. T. Liddle and J. van Slageren, *Chem. Soc. Rev.*, 2015, **44**, 6655–6669.

[28] L. Guokui and B. Jacquier, *Spectroscopic Properties of Rare Earths in Optical Materials*, Springer, Berlin, 2005.

[29] J. D. Rinehart and J. R. Long, *Chem. Sci.*, 2011, **2**, 2078.

[30] L. Ungur and L. F. Chibotaru, *Phys. Chem. Chem. Phys.*, 2011, **13**, 20086.

[31] N. F. Chilton, *Inorg. Chem.*, 2015, 150210090311001.

[32] Y. S. Ding, N. F. Chilton, R. E. P. Winpenny and Y. Z. Zheng, *Angew. Chemie - Int. Ed.*, 2016, **55**, 16071–16074.

[33] C. A. P. Goodwin, F. Ortu, D. Reta, N. F. Chilton and D. P. Mills, *Nat. Publ. Gr.*, 2017, **548**, 439–442.

[34] F. S. Guo, B. M. Day, Y. C. Chen, M. L. Tong, A. Mansikkamäki and R. A. Layfield, *Angew. Chemie - Int. Ed.*, 2017.

[35] D. a. Garanin and E. M. Chudnovsky, 1998, **56**, 18.

[36] W. Wernsdorfer, A. Caneschi, R. Sessoli, D. Gatteschi, A. Cornia, V. Villar and C. Paulsen, *Phys. Rev. Lett.*, 2000, **84**, 2965–2968.

[37] F. Pointillart, K. Bernot, S. Golhen, B. Le Guennic, T. Guizouarn, L. Ouahab and O. Cador, *Angew. Chem. Int. Ed. Engl.*, 2014, 1504–1507.

[38] F. S. Guo, J. L. Liu, J. D. Leng, Z. S. Meng, Z. J. Lin, M. L. Tong, S. Gao, L. Ungur and L. F. Chibotaru, *Chem. - A Eur. J.*, 2011, **17**, 2458–2466.

[39] A. Caneschi, D. Gatteschi, N. Lalioti, C. Sangregorio, R. Sessoli, G. Venturi, A. Vindigni, A. Rettori, M. G. Pini and M. A. Novak, *Angew. Chemie - Int. Ed.*, 2001, **40**, 1760–1763.

[40] M. G. F. Vaz, R. a. A. Cassaro, H. Akpinar, J. a. Schlueter, P. M. Lahti and M. a. Novak, *Chemistry*, 2014, **20**, 5460–7.

[41] F. Liu, D. S. Krylov, L. Spree, S. M. Avdoshenko, N. A. Samoylova, M. Rosenkranz, A. Kostanyan, T. Greber, A. U. B. Wolter, B. Büchner and A. A. Popov, *Nat. Commun.*, 2017, **8**, 16098.

[42] N. Ishii, Y. Okamura, S. Chiba, T. Nogami and T. Ishida, *J. Am. Chem. Soc.*, 2008, **130**, 24–25.

[43] L. Bogani, A. Vindigni, R. Sessoli and D. Gatteschi, *J. Mater. Chem.*, 2008, **18**, 4750.

[44] E. Heintze, F. El Hallak, C. Clauß, A. Rettori, M. G. Pini, F. Totti, M. Dressel and L. Bogani, *Nat. Mater.*, 2013, **12**, 202–6.

[45] K. Bernot, J. Luzon, L. Bogani, M. Etienne, C. Sangregorio, M. Shanmugam, A. Caneschi, R. Sessoli and D. Gatteschi, *J. Am. Chem. Soc.*, 2009, **131**, 5573–5579.

[46] K. S. Pedersen, L. Ungur, M. Sigrist, A. Sundt, M. Schau-Magnussen, V. Vieru, H. Mutka, S. Rols, H. Weihe, O. Waldmann, L. F. Chibotaru, J. Bendix and J. Dreiser, *Chem. Sci.*, 2014, **5**, 1650.

[47] R. Marx, F. Moro, M. Dörfel, L. Ungur, M. Waters, S. D. Jiang, M. Orlita, J. Taylor, W. Frey, L. F. Chibotaru and J. van Slageren, *Chem. Sci.*, 2014, **5**, 3287.

[48] E. Lucaccini, M. Briganti, M. Perfetti, L. Vendier, J.-P. Costes, F. Totti, R. Sessoli and L. Sorace, *Chem. - A Eur. J.*, 2016, **22**, 5552–5562.

[49] B. O. B. O. B. O. B. O. B. O. Roos and P. A. P. Å. P.-A. A. P. Å. P.-A. Malmqvist, *Phys. Chem. Chem. Phys.*, 2004, **6**, 2919–2927.

[50] P. A. Malmqvist, B. O. Roos and B. Schimmelpfennig, *Chem. Phys. Lett.*, 2002, **357**, 230–240.

[51] A. Abragam and B. Bleaney, *Electron paramagnetic Resonance of Transition Ions*, Dover Publications, Mineola, New York, 1986.

[52] H. A. Kramers, *Proceedings of Amsterdam Academy*, 1930, **33**, 959–972.

[53] M. J. Klein, *Am. J. Phys.*, 1952, **20**, 65.

[54] C. Rudowicz, *J. Phys. C Solid State Phys.*, 1985, **18**, 1415–1430.

[55] C. Rudowicz and M. Karbowiak, *Coord. Chem. Rev.*, 2015, **287**, 28–63.

[56] L. F. Chibotaru, *Advances in Chemical Physics, Vol. 153, edited by S. A. Rice and A. R. Dinner*, Wiley, New Jersey, 2013, pp. 397–519.

[57] M. Perfetti, E. Lucaccini, L. Sorace, J. P. Costes and R. Sessoli, *Inorg. Chem.*, 2015, 150310150851006.

[58] L. Sorace, C. Benelli and D. Gatteschi, *Chem. Soc. Rev.*, 2011, **40**, 3092–104.

[59] B. M. Flanagan, P. V. Bernhardt, E. R. Krausz, S. R. Lu and M. J. Riley, *Inorg. Chem.*, 2001, **40**, 5401–5407.

[60] B. M. Flanagan, P. V. Bernhardt, E. R. Krausz, S. R. Lüthi and M. J. Riley, *Inorg. Chem.*, 2002, **41**, 5024–5033.

[61] G. Cucinotta, M. Perfetti, J. Luzon, M. Etienne, P. E. Car, A. Caneschi, G. Calvez, K. Bernot and R. Sessoli, *Angew. Chemie - Int. Ed.*, 2012, **51**, 1606–1610.

[62] L. Ungur and L. F. Chibotaru, *Chem. - A Eur. J.*, 2017, **23**, 3708–3718.

[63] N. F. Chilton, D. Collison, E. J. L. McInnes, R. E. P. Winpenny and A. Soncini, *Nat. Commun.*, 2013, **4**, 2551.

[64] J. J. Baldoví, S. Cardona-Serra, J. M. Clemente-Juan, E. Coronado, A. Gaita-Ariño and A. Palii, *J. Comput. Chem.*, 2013, **34**, 1961–1967.

[65] E. Lucaccini, J. J. Baldoví, L. Chelazzi, A. L. Barra, F. Grepioni, J. P. Costes and L. Sorace, *Inorg. Chem.*, 2017, **56**, 4728–4738.

[66] R. J. Blagg, L. Ungur, F. Tuna, J. Speak, P. Comar, D. Collison, W. Wernsdorfer, E. J. McInnes, L. F. Chibotaru and R. E. Winpenny, *Nature Chem.*, 2013, **5**, 673–678.

[67] S. K. Langley, D. P. Wielechowski, V. Vieru, N. F. Chilton, B. Moubaraki, B. F. Abrahams, L. F. Chibotaru and K. S. Murray, *Angew. Chemie - Int. Ed.*, 2013, **125**, 12014–12019.

[68] S. K. Langley, D. P. Wielechowski, V. Vieru, N. F. Chilton, B. Moubaraki, L. F. Chibotaru and K. S. Murray, *Chem. Commun. (Camb).*, 2015, **51**, 2044–2047.

[69] N. F. Chilton, H. Lei, A. M. Bryan, F. Grandjean, G. J. Long and P. P. Power, *Dalt. Trans.*, 2015, **44**, 11202–11211.

[70] A. Lunghi, F. Totti, S. Sanvito and R. Sessoli, *Chem. Sci.*, 2017, **8**, 6051–6059.

[71] A. Lunghi, F. Totti, R. Sessoli and S. Sanvito, *Nat. Commun.*, 2017, **8**, 1–7.

[72] S. Cardona-Serra, A. Gaita-Ariño, M. Stamenova and S. Sanvito, *J. Phys. Chem. Lett.*, 2017, **8**, 3056–3060.

[73] C. Benelli and D. Gatteschi, *Chem. Rev.*, 2002, **102**, 2369–2387.

[74] S. Demir, I. R. Jeon, J. R. Long and T. D. Harris, *Coord. Chem. Rev.*, 2015, **289-290**, 149–176.

[75] M. Andruh, I. Ramade, E. Codjovi, O. Guillou, O. Kahn and J. C. Trombe, *J. Am. Chem. Soc*, 1993, **115**, 1822–1829.

[76] J. Paulovic, F. Cimpoesu, M. Ferbinteanu and K. Hirao, *J. Am. Chem. Soc.*, 2004, **126**, 3321–3331.

[77] G. Rajaraman, F. Totti, A. Bencini, A. Caneschi, R. Sessoli and D. Gatteschi, *Dalt. Trans.*, 2009, 3153–3161.

[78] N. Iwahara and L. F. Chibotaru, *Phys. Rev. B*, 2015, **91**, 174438.

[79] M. E. Lines, *J. Chem. Phys.*, 1971, **55**, 2977.

[80] L. F. Chibotaru, L. Ungur, C. Aronica, H. Elmoll, G. Pilet and D. Luneau, *J. Am. Chem. Soc.*, 2008, **130**, 12445–12455.

[81] D. Visinescu, A. M. Madalan, M. Andruh, C. Duhayon, J. P. Sutter, L. Ungur, W. Van Den Heuvel and L. F. Chibotaru, *Chem. - A Eur. J.*, 2009, **15**, 11808–11814.

[82] G. Novitchi, G. Pilet, L. Ungur, V. V. Moshchalkov, W. Wernsdorfer, L. F. Chibotaru, D. Luneau and A. K. Powell, *Chem. Sci.*, 2012, **3**, 1169.

[83] J. J. Le Roy, L. Ungur, I. Korobkov, L. F. Chibotaru and M. Murugesu, *J. Am. Chem. Soc.*, 2014, **136**, 8003–10.

[84] L. F. Chibotaru, L. Ungur and A. Soncini, *Angew. Chem. Int. Ed. Engl.*, 2008, **47**, 4126–4129.

[85] S. K. Langley, D. P. Wielechowski, V. Vieru, N. F. Chilton, B. Moubaraki, B. F. Abrahams, L. F. Chibotaru and K. S. Murray, *Angew. Chemie - Int. Ed.*, 2013, **52**, 12014–12019.

[86] T. Gupta, M. F. Beg and G. Rajaraman, *Inorg. Chem.*, 2016, acs.inorgchem.6b01831.

[87] V. Vieru, N. Iwahara, L. Ungur and L. F. Chibotaru, *Sci. Rep.*, 2016, **6**, 24046.

[88] A. Caneschi, D. Gatteschi and F. Totti, *Coord. Chem. Rev.*, 2015, **289-290**, 357–378.

[89] A. Lunghi and F. Totti, *J. Mater. Chem. C*, 2014, **2**, 8333–8343.

[90] S. Ninova, V. Lanzilotto, L. Malavolti, L. Rigamonti, B. Cortigiani, M. Mannini, F. Totti and R. Sessoli, *J. Mater. Chem. C*, 2014, **2**, 9599–9608.

[91] D. Golze, M. Iannuzzi, M. T. Nguyen, D. Passerone and J. Hutter, *J. Chem. Theory Comput.*, 2013, **9**, 5086–5097.

[92] A. Bencini, G. Rajaraman, F. Totti and M. Tusa, *Superlattices Microstruct.*, 2009, **46**, 4–9.

[93] M. Scarrozza, A. Vindigni, P. Barone, R. Sessoli and S. Picozzi, *Phys. Rev. B*, 2015, **91**, 144422.

[94] M. Scarrozza, P. Barone, R. Sessoli and S. Picozzi, *J. Mater. Chem. C*, 2016, **4**, 4176–4185.

[95] J. Hutter, M. Iannuzzi, F. Schiffmann and J. Vandevondele, *Wiley Interdiscip. Rev. Comput. Mol. Sci.*, 2014, **4**, 15–25.

[96] J. Luzon and R. Sessoli, *Dalt. Trans.*, 2012, **41**, 13556–13567.

[97] A. Szabo and N. Ostlund, *Modern Quantum Chemistry*, Dover Publications Inc., Mineola, New York, 1982.

[98] K. Andersson, P.-A. P.-A. Malmqvist and B. O. B. O. Roos, *J. Chem. Phys.*, 1992, **96**, 1218.

[99] Y. Guo, K. Sivalingam, E. F. Valeev and F. Neese, *J. Chem. Phys.*, 2016, **144**, year.

[100] I. B. Bersuker, *Electronic Structure and Properties Of Transition Metal Compounds*, John Wiley and Sons, New York, 1996.

[101] F. Aquilante, J. Autschbach, R. K. Carlson, L. F. Chibotaru, M. G. Delcey, L. De Vico, I. Fdez. Galván, N. Ferré, L. M. Frutos, L. Gagliardi, M. Garavelli, A. Giussani, C. E. Hoyer, G. Li Manni, H. Lischka, D. Ma, P. Å. Malmqvist, T. Müller, A. Nenov, M. Olivucci, T. B. Pedersen, D. Peng, F. Plasser, B. Pritchard, M. Reiher, I. Rivalta, I. Schapiro, J. Segarra-Martí, M. Stenrup, D. G. Truhlar, L. Ungur, A. Valentini, S. Vancoillie, V. Veryazov, V. P. Vysotskiy, O. Weingart, F. Zapata and R. Lindh, *J. Comput. Chem.*, 2016, **37**, 506–541.

[102] B. O. B. O. Roos, R. Lindh, P.-A. Malmqvist, V. Veryazov, P.-O. Widmark, A. C. Borin, B. O. Ross, R. Lindh, P.-A. Malmqvist, V. Veryazov, P.-O. Widmark, A. C. Borin, B. O. B. O. Roos, R. Lindh, P.-A. Malmqvist, V. Veryazov, P.-O. Widmark and A. C. Borin, *J. Phys. Chem. A*, 2008, **112**, 11431–11435.

[103] L. F. Chibotaru and L. Ungur, *J. Chem. Phys.*, 2012, **137**, 064112.

[104] O. Christiansen, J. Gauss and B. Schimmelpfennig, *Phys. Chem. ...*, 2000, **2**, 965–971.

[105] A. I. Liechtenstein, V. I. Anisimov and J. Zaanen, *Phys. Rev. B*, 1995, **52**, 5467–5471.

[106] L. Noodleman and J. G. Norman, *J. Phys. Chem.*, 1979, **70**, 4903.

[107] L. Noodleman, *J. Chem. Phys.*, 1981, **74**, 5737.

[108] R. G. Parr and W. Yang, *Density Functional Theory of Atoms and Molecules*, Oxford University Press, Oxford, 1994.

[109] M. Cococcioni and S. de Gironcoli, 2004, 1–16.

[110] S. L. Dudarev, S. Y. Savrasov, C. J. Humphreys and a. P. Sutton, *Phys. Rev. B*, 1998, **57**, 1505–1509.

[111] R. C. Albers, N. E. Christensen and A. Svane, *J. Phys. Condens. Matter*, 2009, **21**, 343201.

[112] S. Lutfalla, V. Shapovalov and A. T. Bell, *J. Chem. Theory Comput.*, 2011, **7**, 2218–2223.

[113] A. Jain, G. Hautier, S. P. Ong, C. J. Moore, C. C. Fischer, K. A. Persson and G. Ceder, *Phys. Rev. B - Condens. Matter Mater. Phys.*, 2011, **84**, year.

[114] H. J. Kulik, M. Cococcioni, D. A. Scherlis and N. Marzari, *Phys. Rev. Lett.*, 2006, **97**, 1–4.

[115] T. O. Wehling, A. V. Balatsky, M. I. Katsnelson, A. I. Lichtenstein and A. Rosch, *Phys. Rev. B - Condens. Matter Mater. Phys.*, 2010, **81**, 1–6.

[116] T. O. Wehling, A. I. Lichtenstein and M. I. Katsnelson, *Phys. Rev. B - Condens. Matter Mater. Phys.*, 2011, **84**, 1–7.

[117] A. Bencini and F. Totti, *J. Chem. Theory Comput.*, 2009, **5**, 144–154.

[118] A. Bencini and F. Totti, *Int. J. Quantum Chem.*, 2005, **101**, 819–825.

[119] L. Sorace and D. Gatteschi, in *Lanthanides and Actinides in Molecular Magnetism*, ed. R. Layfield and M. Murugesu, John Wiley & Sons, 2015, ch. 1.

[120] D. Aravena and E. Ruiz, *Inorg. Chem.*, 2013, **52**, 13770–13778.

[121] E. Lucaccini, L. Sorace, M. Perfetti, J.-P. Costes and R. Sessoli, *Chem. Commun.*, 2014, **50**, 1648–1651.

[122] J.-L. Liu, K. Yuan, J.-D. Leng, L. Ungur, W. Wernsdorfer, F.-S. Guo, L. F. Chibotaru and M.-L. Tong, *Inorg. Chem.*, 2012, **51**, 8538–8544.

[123] L. Tesi, E. Lucaccini, I. Cimatti, M. Perfetti, M. Mannini, A. Matteo, E. Morra, M. Chiesa, A. Caneschi, L. Sorace and R. Sessoli, *Chem. Sci.*, 2015.

[124] T. Fukuda, N. Shigeyoshi, T. Yamamura and N. Ishikawa, *Inorg. Chem.*, 2014, **53**, 9080–9086.

[125] Y. Rechkemmer, J. E. Fischer, R. Marx, M. Dörfel, P. Neugebauer, S. Horvath, M. Gysler, T. Brock-Nannestad, W. Frey, M. F. Reid, and J. van Slageren, *J. Am. Chem. Soc.*, 2015, **137**, 13114–13120.

[126] S. I. Klokishner, S. M. Ostrovsky, O. S. Reu, A. V. Palii, P. L. Tregenna-Piggott, T. Brock-Nannestad, J. Bendix and H. Mutka, *J. Phys. Chem. C*, 2009, **113**, 8573–8582.

[127] J. Long, J. Rouquette, J.-M. Thibaud, R. A. Ferreira, L. D. Carlos, B. Donnadieu, V. Vieru, L. F. Chibotaru, L. Konczewicz, J. Haines, Y. Guari and J. Larionova, *Angew. Chem. Int. Ed.*, 2015, **54**, 2236–2240.

[128] E. M. Pineda, N. F. Chilton, R. Marx, M. Dörfel, D. O. Sells, P. Neugebauer, S.-D. Jiang, D. Collison, J. van Slageren, E. J. McInnes and R. E. Winpenny, *Nature Commun.*, 2014, **5**, year.

[129] X. Yi, K. Bernot, F. Pointillart, G. Poneti, G. Calvez, C. Daiguebonne, O. Guillou and R. Sessoli, *Chem. Eur. J.*, 2012, **18**, 11379–11387.

[130] M. Llunell, D. Casanova, J. Cirera, J. Bofill, P. Alemany, S. Alvarez, M. Pinsky and D. Avnir, 2003.

[131] M. Perfetti, G. Cucinotta, M.-E. Boulon, F. El Hallak, S. Gao and R. Sessoli, *Chem. Eur. J.*, 2014, **20**, 14051–14056.

[132] L. Rigamonti, A. Cornia, A. Nava, M. Perfetti, M.-E. Boulon, A.-L. Barra, X. Zhong, K. Park and R. Sessoli, *Phys. Chem. Chem. Phys.*, 2014, **16**, 17220–17230.

[133] L. F. Chibotaru and L. Ungur, *J. Chem. Phys.*, 2012, **137**, 064112.

[134] H. B. G. Casimir and F. K. Du Pré, *Physica*, 1938, **5**, 507–511.

[135] M. Gregson, N. F. Chilton, A.-M. Ariciu, F. Tuna, I. F. Crowe, W. Lewis, A. J. Blake, D. Collison, E. J. McInnes, R. E. Winpenny and S. T. Liddle, *Chem. Sci.*, 2016, **7**, 155–165.

[136] J. M. Zadrozny, M. Atanasov, A. M. Bryan, C.-Y. Lin, B. D. Rekken, P. P. Power, F. Neese and J. R. Long, *Chem. Sci.*, 2013, **4**, 125–138.

[137] S. Demir, J. M. Zadrozny and J. R. Long, *Chem. Eur. J.*, 2014, **20**, 9524–9529.

[138] L. Ungur, M. Thewissen, J.-P. Costes, W. Wernsdorfer and L. F. Chibotaru, *Inorg. Chem.*, 2013, **52**, 6328–6337.

[139] F. Pointillart, K. Bernot, S. Golhen, B. Le Guennic, T. Guizouarn, L. Ouahab and O. Cador, *Angew. Chem.*, 2015, **127**, 1524–1527.

[140] C. Das, A. Upadhyay, S. Vaidya, S. K. Singh, G. Rajaraman and M. Shanmugam, *Chem. Commun.*, 2015, **51**, 6137–6140.

[141] Q.-W. Li, J.-L. Liu, J.-H. Jia, J.-D. Leng, W.-Q. Lin, Y.-C. Chen and M.-L. Tong, *Dalton Trans.*, 2013, **42**, 11262–11270.

[142] J. Ruiz, G. Lorusso, M. Evangelisti, E. K. Brechin, S. J. Pope and E. Colacio, *Inorg. Chem.*, 2014, **53**, 3586–3594.

[143] S. Gómez-Coca, A. Urtizberea, E. Cremades, P. J. Alonso, A. Camón, E. Ruiz and F. Luis, *Nature Commun.*, 2014, **5**, year.

[144] J. F. Desreux, *Inorg. Chem.*, 1980, **19**, 1319–1324.

[145] P. Caravan, J. J. Ellison, T. J. McMurry and R. B. Lauffer, *Chem. Rev.*, 1999, **99**, 2293–352.

[146] S. Aime, A. Barge, M. Botta, D. Parker and A. S. De Sousa, *J. Am. Chem. Soc.*, 1997, **119**, 4767–4768.

[147] O. A. Blackburn, N. F. Chilton, K. Keller, C. E. Tait, W. K. Myers, E. J. L. McInnes, A. M. Kenwright, P. D. Beer, C. R. Timmel and S. Faulkner, *Angew. Chemie - Int. Ed.*, 2015, **54**, 10783–10786.

[148] K. Kumar, C. A. Chang, L. C. Francesconi, D. D. Dischino, M. F. Malley, J. Z. Gougoutas and M. F. Tweedle, *Inorg. Chem.*, 1994, **33**, 3567–3575.

[149] K. Micskei, L. Helm, E. Brucher and A. E. Merbach, *Inorg. Chem.*, 1993, **32**, 3844–3850.

[150] T. C. Soesbe, S. J. Ratnakar, M. Milne, S. Zhang, Q. N. Do, Z. Kovacs and A. D. Sherry, *Magn. Reson. Med.*, 2014, **71**, 1179–1185.

[151] S. Viswanathan, Z. Kovacs, K. N. Green, S. J. Ratnakar and A. D. Sherry, *Chem. Rev.*, 2010, **110**, 2960–3018.

[152] B. Graham, C. T. Loh, J. D. Swarbrick, P. Ung, J. Shin, H. Yagi, X. Jia, S. Chhabra, N. Barlow, G. Pintacuda, T. Huber and G. Otting, *Bioconjug. Chem.*, 2011, **22**, 2118–2125.

[153] A. Bhaumik, C. Luchinat, G. Parigi, E. Ravera and M. Rinaldelli, *CrystEngComm*, 2013, **15**, 8639.

[154] L. Benda, J. Mares, E. Ravera, G. Parigi, C. Luchinat, M. Kaupp and J. Vaara, *Angew. Chemie - Int. Ed.*, 2016, **55**, 14713–14717.

[155] S. Dasgupta, X. Hu, P. H. J. Keizers, W. M. Liu, C. Luchinat, M. Nagulapalli, M. Overhand, G. Parigi, L. Sgheri and M. Ubbink, *J. Biomol. NMR*, 2011, **51**, 253–263.

[156] M.-E. Boulon, G. Cucinotta, J. Luzon, C. Degl'Innocenti, M. Perfetti, K. Bernot, G. Calvez, A. Caneschi and R. Sessoli, *Angew. Chem. Int. Ed. Engl.*, 2013, **52**, 350–4.

[157] P.-E. Car, M. Perfetti, M. Mannini, A. Favre, A. Caneschi and R. Sessoli, *Chem. Commun. (Camb).*, 2011, **47**, 3751–3753.

[158] D. Aravena, M. Atanasov and F. Neese, *Inorg. Chem.*, 2016, acs.inorgchem.6b00244.

[159] F. Neese, *Wiley Interdiscip. Rev. Comput. Mol. Sci.*, 2012, **2**, 73–78.

[160] P. J. Stephens, F. J. Devlin, C. F. Chabalowski and M. J. Frisch, *J. Phys. Chem.*, 1994, **98**, 11623–11627.

[161] S. Grimme, J. Antony, S. Ehrlich and H. Krieg, *J. Chem. Phys.*, 2010, **132**, 0–19.

[162] D. a. Pantazis and F. Neese, *J. Chem. Theory Comput.*, 2009, **5**, 2229–2238.

[163] P. E. Blöchl, *J. Chem. Phys.*, 1995, **103**, 7422–7428.

[164] C. Adamo and V. Barone, *J. Chem. Phys.*, 1999, **110**, 6158–6170.

[165] R. Sabatini, T. Gorni and S. De Gironcoli, *Phys. Rev. B - Condens. Matter Mater. Phys.*, 2013, **87**, 4–7.

[166] S. Goedecker, M. Teter and J. Hutter, *Phys. Rev. B*, 1996, **54**, 1703–1710.

[167] V. Veryazov, P. A. Malmqvist and B. O. Roos, *Int. J. Quantum Chem.*, 2011, **111**, 3329–3338.

[168] B. O. Roos, R. Lindh, P. k. Malmqvist, V. Veryazov and P. O. Widmark, *J. Phys. Chem. A*, 2004, **108**, 2851–2858.

[169] V. Veryazov, P.-O. Widmark and B. O. Roos, *Theor. Chem. Accounts Theory, Comput. Model. (Theoretica Chim. Acta)*, 2004, **111**, 345–351.

[170] L. Gagliardi, R. Lindh and G. Karlstrom, *J. Chem. Phys.*, 2004, **121**, 4494.

[171] M. W. Löble, J. M. Keith, A. B. Altman, S. C. E. Stieber, E. R. Batista, K. S. Boland, S. D. Conradson, D. L. Clark, J. Lezama Pacheco, S. A. Kozimor, R. L. Martin, S. G. Minasian, A. C. Olson, B. L. Scott, D. K. Shuh, T. Tyliszczak, M. P. Wilkerson and R. A. Zehnder, *J. Am. Chem. Soc.*, 2015, **137**, 2506–2523.

[172] P. Söderhjelm, J. W. Krogh, G. Karlström, U. Ryde and R. Lindh, *J. Comput. Chem.*, 2007, **28**, 1083–1090.

[173] L. Zhang, J. Jung, P. Zhang, M. Guo, L. Zhao, J. Tang and B. Le Guennic, *Chem. - A Eur. J.*, 2016, **22**, 1392–1398.

[174] S. Niu, M. L. Tan and T. Ichiye, *J. Chem. Phys.*, 2011, **134**, 1–11.

[175] L. Sorace, C. Sangregorio, A. Figuerola, C. Benelli and D. Gatteschi, *Chem. Eur. J.*, 2009, **15**, 1377–1388.

[176] J. J. Baldoví, J. M. Clemente-Juan, E. Coronado and A. Gaita-Ariño, *Inorg. Chem.*, 2014, **53**, 11323–11327.

[177] M. Perfetti, E. Lucaccini, L. Sorace, J.-P. Costes and R. Sessoli, *Inorg. Chem.*, 2015, **54**, 3090–3092.

[178] A. Bencini, A. Dei, C. Sangregorio, F. Totti and M. G. F. Vaz, *Inorg. Chem.*, 2003, **42**, 8065–71.

[179] R. Murakami, T. Nakamura and T. Ishida, *Dalt. Trans.*, 2014, **43**, 5893–5898.

[180] M. Tamura, Y. Nakazawa, D. Shiomi, K. Nozawa, Y. Hosokoshi, M. Ishikawa, M. Takahashi and M. Kinoshita, *Chem. Phys. Lett.*, 1991, **186**, 401–404.

[181] J. Laugier, P. Rey, A. Caneschi, D. Gatteschi, R. Sessoli and C. Zanchini, *J. Am. Chem. Soc.*, 1988, **110**, 2795–2799.

[182] S. G. Reis, M. Briganti, D. O. T. A. Martins, H. Akpinar, S. Calancea, G. P. Guedes, S. Soriano, M. Andruh, R. A. A. Cassaro, P. M. Lahti, F. Totti and M. G. F. Vaz, *Dalt. Trans.*, 2016, **45**, 2936–2944.

[183] J. J. Le Roy, M. Jeletic, S. I. Gorelsky, I. Korobkov, L. Ungur, L. F. Chibotaru and M. Murugesu, *J. Am. Chem. Soc.*, 2013, **135**, 3502–3510.

[184] S. Xue, L. Zhao, Y.-N. Guo, R. Deng, Y. Guo and J. Tang, *Dalton Trans.*, 2011, **40**, 8347–52.

[185] T. Liu, H. Zheng, S. Kang, Y. Shiota, S. Hayami, M. Mito, O. Sato, K. Yoshizawa, S. Kanegawa and C. Duan, *Nat. Commun.*, 2013, **4**, 2826.

[186] L. B. L. Escobar, G. P. Guedes, S. Soriano, N. L. Speziali, A. K. Jordão, A. C. Cunha, V. F. Ferreira, C. Maxim, M. A. Novak, M. Andruh and M. G. F. Vaz, *Inorg. Chem.*, 2014, **53**, 7508–7517.

[187] C. Benelli, A. Caneschi, D. Gatteschi and L. Pardi, *Inorg. Chem.*, 1992, **31**, 741–746.

[188] X.-L. Mei, R.-N. Liu, C. Wang, P.-P. Yang, L.-C. Li and D.-Z. Liao, *Dalt. Trans.*, 2012, **41**, 2904.

[189] R. T. Azuah, L. R. Kneller, Y. Qiu, P. L. W. Tregenna-Piggott, C. M. Brown, J. R. D. Copley and R. M. Dimeo, *J. Res. Natl. Inst. Stand. Technol.*, 2009, **114**, 341.

[190] E. Moreno Pineda, N. F. Chilton, R. Marx, M. Dörfel, D. O. Sells, P. Neugebauer, S.-D. Jiang, D. Collison, J. van Slageren, E. J. McInnes and R. E. Winpenny, *Nat. Commun.*, 2014, **5**, 5243.

[191] V. Vieru, T. D. Pasatoiu, L. Ungur, E. Suturina, A. M. Madalan, C. Duhayon, J.-p. Sutter, M. Andruh and L. F. Chibotaru, *Inorg. Chem.*, 2016, **55**, 12158–12171.

[192] M. G. F. Vaz, R. a. Allão, H. Akpinar, J. a. Schlueter, S. Santos, P. M. Lahti and M. a. Novak, *Inorg. Chem.*, 2012, **51**, 3138–45.

[193] P. J. Van Koningsbruggen, O. Kahn, K. Nakatani, Y. Pei, J. P. Renard, M. Drillon and P. Legoll, *Inorg. Chem.*, 1990, **29**, 3325–3331.

[194] C. Coulon, H. Miyasaka and R. Clerac, *Structure and Bonding, Vol. 122. edited by R. Winpenny*, Springer-Verlag, Berlin, 2006, pp. 163–206.

[195] S. K. Singh, K. R. Vignesh, V. Archana and G. Rajaraman, *Dalt. Trans.*, 2016, **45**, 8201–8214.

[196] X. Liu, X. Feng, Y. Zhang, X. Zhang, C. Gao, J. Liu, B. Wang, K. S. Pedersen, L. Keller, Y.-Q. Zhang, W. Shi, S. Gao, P. Cheng and J. R. Long, *ArXiv*, 2017, 1709.07697.

[197] J. VandeVondele and J. Hutter, *J. Chem. Phys.*, 2003, **118**, 4365–4369.

[198] S. Sinnecker, F. Neese, L. Noodleman and W. Lubitz, *J. Am. Chem. Soc.*, 2004, **126**, 2613–2622.

[199] H. Xiang, C. Lee, H.-J. Koo, X.-g. Gong and M.-H. Whangbo, *Dalt. Trans.*, 2012, **42**, 823–853.

[200] L. Wang, T. Maxisch and G. Ceder, *Phys. Rev. B - Condens. Matter Mater. Phys.*, 2006, **73**, 1–6.

[201] M. Bajdich, M. García-Mota, A. Vojvodic, J. K. Nørskov and A. T. Bell, *J. Am. Chem. Soc.*, 2013, **135**, 13521–13530.

[202] M. García-Mota, M. Bajdich, V. Viswanathan, A. Vojvodic, A. T. Bell and J. K. Nørskov, *J. Phys. Chem. C*, 2012, **116**, 21077–21082.

[203] R. A. A. Cassaro, S. G. Reis, T. S. Araujo, P. M. Lahti, M. A. Novak and M. G. F. Vaz, *Inorg. Chem.*, 2015, **54**, 9381–9383.

[204] L. Malavolti, V. Lanzilotto, S. Ninova, L. Poggini, I. Cimatti, B. Cortigiani, L. Margheriti, D. Chiappe, E. Otero, P. Sainctavit, F. Totti, A. Cornia, M. Mannini and R. Sessoli, *Nano Lett.*, 2015, **15**, 535–541.

[205] J. A. Burgess, L. Malavolti, V. Lanzilotto, M. Mannini, S. Yan, S. Ninova, F. Totti, S. Rolf-Pissarczyk, A. Cornia, R. Sessoli and S. Loth, *Nat. Commun.*, 2015, **6**, 8216.